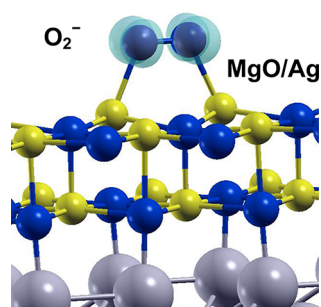


Electron Transfer at Oxide Surfaces. The MgO Paradigm: from Defects to Ultrathin Films

Gianfranco Pacchioni^{*,†} and Hajo Freund[‡]

[†]Dipartimento di Scienza dei Materiali, Università di Milano-Bicocca, Via R. Cozzi, 53–20125, Milano, Italy

[‡]Fritz-Haber-Insitut der MPG, Department of Chemical Physics, Faradayweg 4-6, 14195 Berlin, Germany



CONTENTS

1. Introduction	4035
2. Electron Transfer at MgO Surfaces: The First Observations	4037
3. Defects, Morphological Irregularities, and Electron Traps on the MgO Surface	4037
3.1. Role of Low-Coordinated Sites	4037
3.2. Optical Properties of MgO Nanocrystals	4039
3.3. Oxygen Vacancy or F Center Model	4040
3.4. From the F Center Model to F ₂ (H ⁺) Defects	4044
3.5. Electron-Rich Surfaces: New Models of Surface Traps	4044
3.6. Electron Traps at Hydroxylated MgO Surfaces	4047
3.7. Defects at the MgO Surface: Summary	4050
4. Imaging Surface Defects	4050
4.1. Atomic Force Microscopy and Scanning Tunneling Microscopy	4050
4.2. Stability and Diffusion of Oxygen Vacancies	4054
5. Not Only Point Defects: Grain Boundaries	4055
5.1. Strain and Dislocations in MgO Thin Films	4055
5.2. Electron Trapping at Grain Boundaries	4056
6. New Frontiers: Defects Engineering via Doping of Oxide Films	4058
6.1. Li-Doped MgO in Methane Coupling Reactions	4058
6.2. Transition Metal Doping of CaO Films	4058
7. MgO Ultrathin Films: Electron Transfer via Tunneling Mechanisms	4061
7.1. Cabrera–Mott Theory of Oxidation of Metals	4061
7.2. Spontaneous Charging of Adsorbates on MgO Ultrathin Films	4062
7.3. Conditions for the Occurrence of Direct Charge Transfer	4063
7.4. Work Function Changes Induced by Oxide Thin Films on Metals	4065
7.5. Structural Flexibility of Oxide Ultrathin Films	4066
8. Synopsis	4067

Author Information	4067
Corresponding Author	4067
Notes	4067
Biographies	4068
Acknowledgments	4068
References	4068

1. INTRODUCTION

Electron transfer (ET) is a fundamental process in physics, chemistry, and biology.¹ Charge transfer determines phenomena like oxidation and reduction, bond activation and bond breaking in chemical reactions, formation of radical species, and charge transport and charge trapping in nanoelectronic devices, just to mention a few examples. ET processes are the basis of technologically relevant fields such as electrochemistry, homogeneous, heterogeneous and enzymatic catalysis, photovoltaic energy production, dye-sensitized solar cells, photocatalysis, sensors, information storage, molecular electronics, etc.² ET may involve donors and acceptors at the molecular level, but often one of the components is a solid metal, a semiconductor, or an insulator. In this latter case the donor or acceptor state usually corresponds to a specific site on the surface of the material, for example, a defect, a morphological irregularity, an exposed atom, or a functional group. A well-defined orbital energy is associated to each of these sites, and the overlap and interaction with the occupied or empty states of incoming molecules, clusters of atoms, or extended systems determines the extent and the direction of charge exchange. The theoretical foundations of ET processes in condensed phases have been addressed in dedicated articles and reviews, and the reader is referred to these studies for a more thorough treatment³

There are situations where it is possible to follow the ET process in detail by looking at the fate of the transferred electron. This is when paramagnetic centers or paramagnetic species form during the ET process. In this case electron paramagnetic resonance (EPR) spectroscopy may be used to monitor the reaction. This is a powerful technique that provides direct information on the nature of the reactants and products involved in ET.⁴ It is only applicable and then very sensitive to the presence of unpaired electrons, being able to reveal 10¹² spins; this means that for a high surface area polycrystalline oxide sample of, say, 200 m²/g the lower limit of sensitivity is

Special Issue: 2013 Surface Chemistry of Oxides

Received: May 17, 2012

Published: November 1, 2012

10^7 spins/cm², i.e., about a paramagnetic center every 10^8 surface atoms. When the involved donor and acceptor species are not paramagnetic, the identification of the occurrence of an ET, and of its extent, is less straightforward and requires the study of indirect signatures and evidence like changes in the vibrational, optical, or other spectroscopic properties that provide an indication that a charge displacement has occurred. Often, an analysis of the charge transfer based on these measurements is far from being straightforward, as the contribution of the charge displacement to the specific property monitored can be difficult to disentangle from other effects. In the case of X-ray photoemission measurements, for example, the shifts of the core level binding energies are only partly determined by changes in the charge state of a given atom and often are the result of several, sometimes canceling, contributions.⁵

Oxide-based materials are frequently used when it comes to employing ET toward technically relevant applications, such as microelectronics, spintronics, corrosion protection by passive layers, heterogeneous catalysis, use of solar light for environmental and energy applications, drug delivery, etc.⁶ Oxides exhibit a great variety of electronic and crystalline structures; some are wide gap insulators, others are semiconductors. There are oxides that undergo a metal–insulator transition as a function of pressure and temperature and oxides with superconducting properties below a critical temperature. Oxides may be used as crystalline phases at different temperatures, in glassy state, in form of powder or nanocrystals, or as thin films or single crystals. The properties, and in particular the surface properties, of oxides are strongly dependent on the morphology of the sample, preparation method, surface area, presence of impurities, etc. Metal ions in oxide materials, and in particular transition metal ions, may easily change oxidation state, often resulting in nonstoichiometric and highly defective materials. For all these reasons the identification of surface sites and species directly involved in ET processes is often difficult and requires the development and use of sophisticated techniques.

A precise identification of the sites responsible for ET in solid surfaces is of key importance for the description of the process. Heterogeneous ET processes, involving a solid surface and a molecular adsorbate, are described in a similar way as for the homogeneous counterpart, i.e., the transfer of an electron from a single localized excited donor state D to a single localized acceptor state A:



In this case the electronic–nuclear coupling is strong and electron transfer is controlled by nuclear motion. The system moves on diabatic energy surfaces. Tunneling between reactant and product state occurs when both electronic levels are in resonance. The motion of the nuclei is the driving force for achieving the resonance condition, and in the classical Marcus theory⁷ the nuclear motion is expressed in terms of harmonic oscillators for the reactant and product states. The two diabatic energy surfaces for the reactant and product states are depicted in Figure 1.

The crossing point of the two parabolas is the transition state (TS). For weak electronic couplings the probability for a transition to the product state at the crossing point is small. The quantum mechanical description in the nonadiabatic limit can be done in terms of first-order perturbation theory. For a harmonic perturbation this results in Fermi's golden rule:

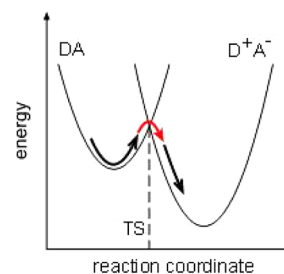


Figure 1. Diabatic energy surfaces for the reactant DA and product D^+A^- states along the reaction.

$$k_{ET} = (2\pi/h)/V_R^2FC \quad (2)$$

The rate of electron transfer k_{ET} depends on the electronic coupling matrix element V_R and the Franck–Condon-weighted density of states (FC). FC is the integrated overlap of reactant and product nuclear wave functions of equal energy. The above model holds true only for weak electronic coupling, i.e., the probability of crossing the transition state is much smaller than 1 and, thus, the frequency of the nuclear motion is much higher than the transfer rate. For strong electronic coupling, the so-called adiabatic limit, the tunneling probability is nearly 1 and the electron follows the nuclear motion along the reaction coordinate. In this case one can no longer distinguish between reactant and product state, the splitting at the transition point gets bigger, and the electronic wave function moves along the double-well potential composed of reactant and product potential.

The major difference between molecular (homogeneous) and heterogeneous ET from a molecular donor to a solid-state acceptor (or vice versa) is the number and energy of accessible acceptor (or donor) states. The single parabola of the reactant in Figure 1 couples to a whole series of product states with different ground-state energies.² Each curve represents the electron in any electronic state as well as the ionized adsorbate molecule in the pertinent vibrational state. An accurate description of the states involved and of the nature of the ET process clearly requires the full electronic characterization of the D and A species. Although for an intermolecular process this is clearly defined, when a solid surface is involved, this is no longer obvious, and the identification of the local sites taking part to the ET process becomes relevant. This requires a detailed knowledge of the surface, its morphology, and its defect density, something which is possible only with a characterization of the surface at an atomistic level.

During the last few decades the level of understanding of ET phenomena at oxide surfaces has increased enormously.^{4,8} For some simple oxides, the combined use of advanced spectroscopic and microscopic methods, often in combination with modern electronic structure theory, allowed one to reach a detailed microscopic understanding of phenomena involved in ET processes. One of the best characterized systems is MgO, a simple stoichiometric binary oxide with rock-salt structure, which exhibits well-defined surfaces and is stable under operating conditions. Despite this apparent simplicity, a lot of work spanning several decades has been necessary to unravel the atomistic details of reactivity of this material. In this review, we will consider the major steps that have led to a progressive identification of the sites involved in ET reactions on ionic oxide surfaces, MgO in particular, of their abundance, stability, and formation as a function of external conditions, of the

products and processes based on ET, etc. We will also discuss effects related to nanostructuring and nanodimensionality connected with the occurrence of ET on ultrathin oxide films grown on a metal substrate. The analysis of the successes, and of the failures, in the attempt to characterize ET at MgO surfaces can be regarded as a paradigmatic example of how the evolution of scientific knowledge sometimes follows complex and nonlinear paths. It also shows how difficult and ambitious the objective to reach control at an atomistic level on surface properties and surface reactivity is. At the same time, it provides an illustrative example of how general notions, concepts, and ideas can be derived from the study of simple systems and how they may be exploited to develop more complex and technologically more relevant materials or devices. It is the combination of this knowledge and expertise that finally allows one to design and prepare new materials and new systems based on a rational and comprehensive description of complex systems.

2. ELECTRON TRANSFER AT MgO SURFACES: THE FIRST OBSERVATIONS

One of the first detailed reports of the occurrence of an ET from an oxide surface to an adsorbed species goes back to the second half of the last century. In 1960 Kohn reported the disappearance of an EPR signal in irradiated silica by exposure to O₂ and attributed it to the interaction of electrons trapped at an oxygen vacancy in the lattice.⁹ A few years later a similar process was postulated by Nelson and Tench for an irradiated MgO surface.¹⁰

However, it was only around the mid-1960s that, thanks to the very careful work of Lunsford and Jayne,¹¹ a direct proof of the occurrence of an ET process at the MgO surface was given. In their work, Lunsford and Jayne were able to identify the formation of CO⁻, CO₂⁻, and O₂⁻ radicals by exposure of UV-irradiated MgO powders to the corresponding neutral gas-phase molecules. They reported the g-tensor of the new radical species and concluded that their spontaneous formation was due to the interaction of the gas-phase molecules with electrons trapped in paramagnetic surface defects, most likely lattice vacancies. Lunsford and Jayne demonstrated, for the first time, the possibility to closely monitor the selective activation of a molecular adsorbate by ET from a surface site to the antibonding states of the admolecule, i.e., the first step toward bond breaking and chemical reactivity.

Although EPR spectra provide a direct and useful way to detect the transfer of single electrons in chemical processes, this is not the only way to monitor electron exchange on oxide surfaces. In the late 1970s, Zecchina and Stone suggested,¹² based on reflectance IR spectra of CO molecules adsorbed on polycrystalline alkaline earth oxides, including MgO, that complex oligomers of general formula [C_nO_{n+1}]²⁻ can form even at low temperature by simple exposure of MgO to a CO atmosphere. Later it was demonstrated that the transfer of electrons from the basic sites of the oxide surface, i.e., some specific O²⁻ ions, to the empty states of the CO molecule is the initial step in a polymerization reaction.^{8g,13} ET via electron tunneling from bulk defect centers to adsorbed N₂O molecules was postulated by Aristov et al. in order to rationalize the observed high reactivity of polycrystalline MgO samples.¹⁴

Although it is obvious that in the experiments of both Lunsford–Jayne¹¹ and Zecchina–Stone¹² electrons flow from the oxide surface toward the adsorbed molecule, it is also clear that the ET process involves different sites on the oxide surfaces

and that this results in different products and reaction mechanisms. Thus, the search for the sites responsible for the specific reactivity, and the identification of the conditions favoring one ET mechanism with respect to another one, is the first step if one wants to deeply understand the nature of the ET process. To do this we have to consider in more detail the nature of donor and acceptor states on the surface of an ionic oxide. MgO is used as the example.

3. DEFECTS, MORPHOLOGICAL IRREGULARITIES, AND ELECTRON TRAPS ON THE MgO SURFACE

3.1. Role of Low-Coordinated Sites

MgO is a wide gap insulator with a band gap of about 7.8 eV,¹⁵ a value which is well-reproduced by GW quasiparticle band structure calculations.¹⁶ It is highly ionic, and the formal charge of the O and Mg ions is very close to the nominal -2/+2 value.¹⁷ The valence band is formed from O 2p orbitals slightly mixed with the Mg 3s and 3p states, while the conduction band is essentially made by Mg 3s–3p levels.¹⁸ The net charge separation between cations and anions in MgO is the consequence of the Madelung potential, which strongly contributes to a stabilization of the system. As a result, the top of the valence band formed by O 2p levels is very deep, i.e., about 9 eV below the vacuum level.¹⁹ Extracting electrons from the 2p levels of bulk, six-coordinated O²⁻ ions (O_{6C}) has, thus, a high energy cost (high ionization potential, IP). At the same time the Mg 3s–3p levels are very high in energy and rather close to the vacuum limit, which corresponds to a very small electron affinity (EA) of less than 1 eV. Stated differently, the bulk O²⁻ and Mg²⁺ ions of MgO have very little tendency to donate or, respectively, to accept electrons, thus explaining the high stability of the system. However, we note that the O²⁻ ion is unstable in the gas phase where it spontaneously dissociates into O⁻ plus one electron. Therefore, O²⁻ anion only exists in ionic crystals thanks to the stabilizing effect of the Madelung potential. This, in turn, is directly related to the value of the Madelung constant, which depends on the crystal structure and the local coordination of a given ion in the crystal. A weaker Madelung potential results in a lower stability of the Mg and O ions and in a more pronounced tendency to donate (for O²⁻) or to accept (for Mg²⁺) electrons. When one considers the most stable (001) surface of MgO there is only little change compared to the bulk. Here the ions are 5-fold-coordinated, and the reduction of the Madelung constant from the bulk value, 1.747, to that of the (001) surface, 1.681, does not change the stability of the MgO ions drastically.²⁰ The O 2p states of the surface are higher in energy than the bulk ones (in the same way, the Mg 3s–3p states are lower than in the bulk). This results in a change in the position of the top of the valence band, which, according to metastable impact electron spectroscopy (MIES) data, is at about 6.7 eV below vacuum,²¹ and in a concomitant reduction of the band gap. However, this is not sufficient to turn the (001) surface of MgO into a chemically reactive entity.

The best proof of this is that, when a defect-free MgO (001) single crystal surface is exposed to CO gas-phase molecules, no reaction, and in particular no ET, occurs. The CO molecules are very weakly bound to the cations of the surface, by about 0.14 eV on MgO(001) single crystals,²² and by about 0.11 eV on MgO nanocrystals.²³ The bonding is almost entirely due to dispersion forces²⁴ (for a thorough discussion of the interaction of CO with the MgO surface, see ref 25). The basicity of the

O²⁻ sites is so low that electrons are not transferred to the CO empty states and no bond is formed (actually, the interaction with the O anions is repulsive). This is true, also, if instead of CO one considers the more reactive CO₂ molecule. The potential energy curve for the reaction of CO₂ with the MgO(001) surface is repulsive, and indeed the formation of surface carbonates is not observed on the flat terraces.²⁶ This is completely different from what was reported by Zecchina and Stone¹² in their experiments where a high reactivity was observed by simple exposure of MgO powders to CO (for a recent review of the reactivity of MgO powders, see ref 8g).

The different behavior is now well-understood and is related to the presence of several low-coordinated (lc) ions on nanostructured oxides (Figure 2). For MgO powders, if the size

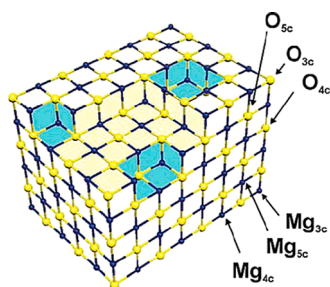
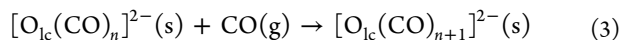


Figure 2. Schematic representation of low-coordinated sites on a MgO cubic nanocrystal. The blue area indicates the position of missing O ions (F centers).

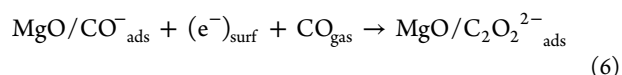
of the grains is in the nm range, there are a large number of edge, step, corner, and kink sites. O anions and Mg cations at these sites are much less stabilized than their surface or bulk counterparts (the Madelung constant is 1.591 for a four-coordinated edge site, 1.344 for a three-coordinated corner site, and can be even lower for kinks and other low-coordinated sites). The consequence is that the occupied 2p levels of O anions at these sites are destabilized and rise in energy, introducing new states in the band gap of the material. In chemical terms, these occupied states are sufficiently high in energy that the O²⁻ ion acts as Lewis base and donates electrons to the empty orbitals of incoming molecules (Lewis acids).²⁶ At the O_{lc}²⁻ sites the CO molecules interact via an acid–base mechanism to form adsorbed [O_{lc}–CO]²⁻ species, which can further react and evolve into oligomeric [C_nO_{n+1}]²⁻ chains with various structures and lengths. The ET in this case is almost barrierless and can occur even at liquid nitrogen temperature:^{8g,13,27}



In a similar way, CO₂ molecules easily interact with edge, step, or corner sites of MgO nanoparticles to form stable [O_{lc}–CO₂]²⁻ surface carbonates.^{26,28} It is interesting to note that the O_{5c}²⁻ ions at the (001) terraces of CaO exhibit a similar reactivity to that of the low-coordinated anions of MgO; in fact, stable chemisorbed species form at the terraces of CaO.²⁶ This result is consistent with the trend of surface basicity, MgO < CaO < SrO < BaO. CaO is more reactive than MgO simply because it has a larger lattice constant and, hence, a weaker Madelung potential, which destabilizes the O 2p states of the surface oxide anions. The different reactivity of MgO versus CaO surfaces has been confirmed by MIES experiments on

CO₂ adsorption on MgO²⁸ and CaO²⁹ as well as by synchrotron-based photoemission spectroscopy.³⁰

It is important to mention that, in the reactions described above, see, e.g., reaction 3, the formal oxidation state of the C atom of the CO or CO₂ molecules does not change and the process does not correspond to a redox reaction. This is completely different from what occurs when electron-rich surfaces are exposed to the same molecules as in this case a real redox chemistry occurs with formation of both diamagnetic and paramagnetic species:³¹



These processes involve a net ET from the surface but imply the presence of electrons trapped at specific defect sites. Therefore, two channels can be identified for ET reactions, one related to the presence of basic, low-coordinated sites and one (reductive ET) related to the presence of trapped electrons, as will be discussed later (see section 3.6 and Table 1).

Table 1. Summary of Most Important Surface Point Defects in MgO

defect	symbol	schematic description
low-coordinated cation	Mg ²⁺ _{nc} (n = 3, 4)	coordinatively unsaturated cation
low-coordinated anion	O ²⁻ _{nc} (n = 3, 4)	coordinatively unsaturated anion
hydroxyl group	(O _{nc} H) (n = 3, 4)	proton attached to O ²⁻
anion vacancy	F ^{m+} _{nc} (m = 0, 1, 2; n = 3, 4, 5)	missing oxygen with trapped electrons
cation vacancy	V ^{m-} _{nc} (m = 0, 1, 2; n = 3, 4, 5)	missing cation with holes at O neighbors
Mg and O divacancy	V _{MgO}	cation and anion vacancy
impurity atoms	M ^{x+} /O ^{y-} (e.g., Mg ²⁺ /X ²⁻)	substitutional cation (M) or anion (X)
oxygen radical	O ⁻ _{nc} (n = 3, 4, 5)	hole trapped at O anion
anion vacancy aggregate	M ^{m+} (m = 0, 1)	two (or more) adjacent oxygen vacancies
shallow electron traps	MgO _{nc} (e ⁻) (n = 3, 4)	trapped electrons at exposed cations
deep electron traps	MgO _{nc} (H ⁺)(e ⁻) (n = 3, 4) MgO _{nc} (M ⁺)(e ⁻) (n = 3, 4)	proton (H ⁺) and electron pair cation (Na ⁺ , etc.) and electron pair
grain boundaries	GB	interface between MgO nanocrystals

The presence of low-coordinated O²⁻ sites in fully stoichiometric samples results in a marked surface basicity and is related to a change in stability and position of the corresponding energy levels in the gap of the material, as will be discussed in section 3.2 (see also Figure 5). When going from a (001) single crystal surface, where the number of such sites is negligible, to a powder sample, where these sites represent a significant fraction of the total exposed surface, one observes a complete change of reactivity, from totally inert to highly reactive. This reactivity is the direct consequence of an ET transfer from the electron-rich O anions to acceptor molecules.

The situation is perfectly symmetric if one considers the Mg²⁺ cations. Surface Mg²⁺ ions have very small electron

affinity, i.e., they exhibit poor acidic character. However, the empty states of Mg^{2+} cations at steps, edges, corners, and kinks are lower in energy and have an enhanced acidic (acceptor) character. A clear and direct proof of this change in electronic structure is, again, related to the interaction with CO molecules. CO is only very weakly bound at five-coordinated Mg^{2+} cations, and the bonding arises mainly from dispersion forces. The C–O internal stretching frequency is weakly perturbed by the interaction with the surface, and vibrational shifts of about $+10\text{ cm}^{-1}$ are measured with respect to the free molecule.³² On MgO powders or even thin films, however, the presence of several low-coordinated cations results in stronger binding sites for CO.³³ The adsorption energy increases, as shown by temperature-programmed desorption (TPD) spectra, where the desorption temperature increases from 57 K for (001) terrace sites ($\text{Mg}_{\text{5c}}^{2+}$) to 80 and 100 K for steps and corner sites ($\text{Mg}_{\text{4c}}^{2+}$ and $\text{Mg}_{\text{3c}}^{2+}$, respectively).³⁴ At the same time, the CO stretching frequency shifts to the blue, providing a direct measure of the modified character of the adsorbate.³⁵ Notice that exactly the same results are obtained when CO is used to monitor the acid sites of MgO single crystals or powder samples. The Fourier transform infrared (FTIR) spectra of CO adsorbed on polycrystalline MgO smoke (investigated at 60 K) fully reproduce those of CO adsorbed on the (001) surface of ultrahigh vacuum (UHV) cleaved single crystals.³⁶ Although the main spectral feature at 2157 cm^{-1} is due to the $\nu(\text{CO})$ modes of $\text{Mg}_{\text{5c}}^{2+}$ –CO adducts formed on the (001) terminations of the cubic MgO smoke microcrystals, a much weaker feature at 2167 – 2164 cm^{-1} is due to $\text{Mg}_{\text{5c}}^{2+}$ –CO complexes formed at the edges of the microcrystals.²³ The vibrational shift results from the combined effect of (i) a stronger interaction of the electric field generated by the surface cation and the CO dipole moment and (ii) a more pronounced ET from the CO 5σ molecular orbital to the Mg^{2+} empty states.³⁷ Thus, the low-coordinated Mg cations are sufficiently strong acids to bind the weak CO base.

This has important consequences! One is the possibility to trap electrons forming shallow donor states on the surface of the oxide, an aspect crucially important for our understanding of the properties of grain boundaries, and oxide–oxide interfaces in polycrystalline samples. This brief discussion clearly shows that the ET properties of cation and anion sites of the MgO surface are directly related to their position and coordination on the surface. Highly coordinated ions have occupied and empty states deep and high in the gap, respectively, resulting in high stability and low ET properties. Low-coordinated ions have electronic states much closer to the frontier orbitals of the incoming molecules, resulting in strong chemical interaction and pronounced ET activity.

3.2. Optical Properties of MgO Nanocrystals

A direct measure of the combined change in position of filled and unfilled states at the MgO surface comes from optical measurements. For the whole family of alkaline earth oxides, measurements in the UV-vis region by means of diffuse reflectance spectroscopy have shown, long ago, that at least three electronic transitions are present at energies lower than that of oxygen bulk excitations. They correspond to surface states involving nonbulk sites.³⁸

To correlate the structural properties described above with optical parameters, optical absorption and luminescence measurements have been performed on MgO nanocrystals³⁹ and thin films.⁴⁰ Two absorption bands have been identified at

220–230 nm (5.4–5.6 eV) and 270 nm (4.6 eV),^{39a} with associated emission bands located around 280 nm (4.4 eV) and 380–400 nm (3.1–3.3 eV), respectively.^{39a,40} For the nanoparticles, a clear dependence of the intensity of the two bands on the average size of the crystallites has been observed (Figure 3a).

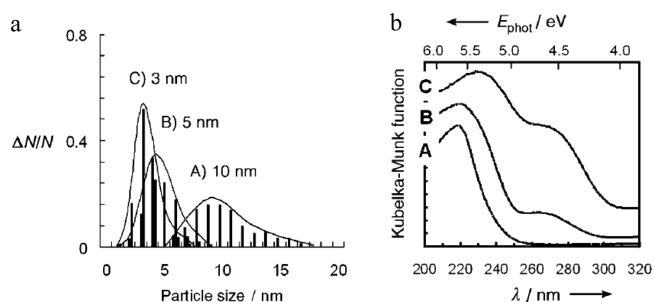


Figure 3. (a) Size distribution of MgO nanoparticles prepared by chemical vapor deposition (CVD); (b) UV diffuse reflectance spectra of samples A, B, and C.^{39a} Reproduced with permission from ref 39a. Copyright 2005 Wiley-VCH.

The origin of the bands has been assigned to absorption of four-coordinated O^{2-} anions in cube edges ($\lambda = 230\text{ nm}$) and three-coordinated O^{2-} anions in corner positions (270 nm).⁴¹ The lowest energy transitions at 4.6 eV are dominated by electron transfer from a 2p state of the O_{3c} ion to the lowest unoccupied molecular orbital (LUMO) delocalized over three neighboring Mg_{4c} ions (Figure 4). Larger cubes imply lower

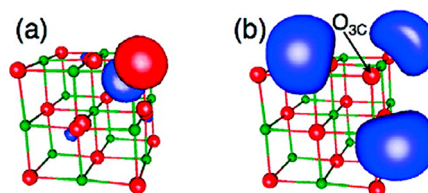


Figure 4. Molecular orbitals involved in the optical transition at 4.6 eV in MgO nanocubes: (a) O 2p HOMO; (b) linear combination of Mg 3s LUMO.^{39b} Reproduced with permission from ref 39b. Copyright 2007 American Chemical Society.

relative concentrations of corners with respect to edge anions, with a consequent change of absorption intensity (Figure 3b). It has been estimated that, for a constant quantity of 100 mg of MgO, the total number of corner anions ranges from 4×10^{16} for 10 nm cubes to 144×10^{16} for 3 nm cubes.^{39a}

The characteristic light emissions are rationalized as follows. First, surface excitons are formed by excitation of O^{2-} ions with photons or electrons. They are dominantly excited at 5-fold coordinated terrace sites (O_{5c} sites), simply because those are the most abundant sites. Excitons on the MgO surface are mobile and may diffuse away from their excitation center in a random-walk-type process.⁴¹ The diffusion stops when the electron–hole pair becomes trapped at point defect sites (e.g., cation or anion vacancies) or sites with lower local coordination, such as 4-fold coordinated edge or 3-fold coordinated corner sites. The trapping occurs because of the smaller Madelung potential at low-coordinated sites, resulting in a stabilization of the electron–hole pair. Defects and low-coordinated edge or corner sites are therefore preferential recombination centers for surface excitons and dominate the

emission characteristics of MgO. The relative importance of the two exciton-decay pathways, either via corner and edge sites or via oxygen vacancies, has been heavily debated in the literature. In photoluminescence measurements on defect-poor MgO nanocubes, two emission bands have been identified at 3.84 and 3.2 eV and assigned to a radiative recombination of excitons at 4c edge and 3c corner sites, respectively.^{39a,42} This interpretation is in accordance to previous data on MgO smokes⁴³ and theoretical calculations.⁴⁴ Slightly different results were reported by other groups, with emission bands somewhat red-shifted to 3.2 eV for the 4c and 2.7 eV for the 3c emission centers.⁴⁵ On the other hand, an emission band at 3.2 eV detected for MgO single crystals was claimed to originate from an emission mechanism involving O vacancies with a single trapped electron (F^+ centers, see below).⁴⁶

To discriminate between the two proposed mechanisms, color centers have been intentionally introduced into the surface of MgO films by exposing the film to a flux of high-energy electrons prior to spectroscopy.⁴⁰ Electron bombardment induces desorption of O atoms from the MgO surface in an Auger-like process and should thus intensify the emission channel involving O vacancies.⁴⁷ However, a decrease in emission intensity was observed for electron-bombarded films, pointing toward a minor role of O vacancies in the emission process. The two bands in the optical emission spectra are therefore interpreted as a signature of radiative exciton decays from low-coordinated MgO sites. The emission peak at 3.1 eV has been assigned to emission centers located at 3c corner sites on the MgO surface, whereas the second peak (4.4 eV) has been attributed to emission from 4c anion sites located at MgO step edges, in agreement with observations made on MgO powders.⁴³ These measurements provide a direct proof that the filled and empty states of the low-coordinated O and Mg sites on MgO surfaces are considerably shifted with respect to the corresponding levels of the 5c surface ions (Figure 5).

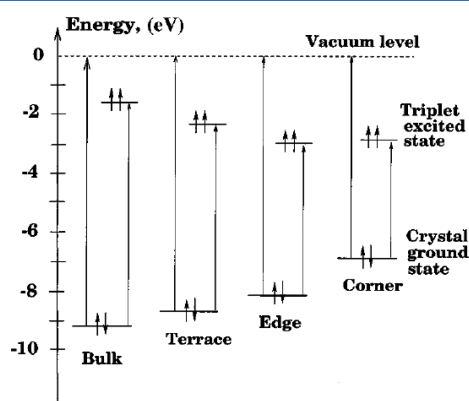


Figure 5. Relative energies of ground and excited states related to the positions of filled and empty states associated to 6c, 5c, 4c, and 3c Mg and O ions on the MgO surface.^{44b} Reproduced with permission from ref 44b. Copyright 1999 American Physical Society.

This discussion shows that MgO can give rise to completely different chemical properties depending on the morphology of the samples. Single crystals, virtually defect-free, are dominated by large (001) terraces where all the ions are five-coordinated, highly stable, with very poor acidic or basic properties (no ET). MgO powders, polycrystalline films, or low-quality epitaxial thin layers, rich in morphological defects like steps, edges, grain boundaries, etc., exhibit a completely different surface reactivity

due to the lower stability of the ions at the low-coordinated sites. This facilitates all kinds of ET phenomena. However, although the involvement of these sites explains the formation of direct bonding and activation of adsorbed species via charge delocalization, their presence cannot easily explain the formation of paramagnetic centers and radical molecules, as observed in other experiments, in particular for UV-irradiated MgO samples. The nature of these defects is more specific. The identification of those sites has required work spanning a few decades, as discussed in the next sections.

3.3. Oxygen Vacancy or F Center Model

The notion of electrons trapped at anion vacancies is well-known in ionic materials like NaCl, and the model of an electron bound to an anion vacancy in alkali halides was proposed by de Boer in 1937.⁴⁸ Because of their particular optical properties, these centers are known as color or *Farbzentren* (F centers). The observation of single electrons trapped in the lattice of bulk MgO dates back from 1957 when an EPR spectrum generated by irradiating MgO crystals was interpreted as arising from F^+ centers, anion vacancies trapping one electron.⁴⁹ Notice that in MgO, also F^0 and F^{2+} centers with two and no trapped electrons, respectively, may exist. This model was refined about 10 years later by Henderson and Wertz, who were able to measure the small isotropic hyperfine interaction, $a_{\text{iso}} = 0.4$ mT, of the unpaired electron with the ^{25}Mg ions.⁵⁰ Notice that the a_{iso} value for a free, isolated Mg^+ cation with a single electron in the 3s orbital is about 17 mT, typical for an unpaired electron in a spherical symmetric orbital. The $a_{\text{iso}}(^{25}\text{Mg}) = 0.4$ mT measured for one electron trapped at a bulk vacancy is therefore 40 times smaller than for a Mg^+ isolated ion, suggesting that only a fraction of the spin density resides on the Mg ions and that the unpaired electron is localized in the center of the vacancy.⁵¹ This picture is consistent with that provided by theory for an F^+ center where the unpaired electron is indeed localized in the anion vacancy and is only weakly interacting with the Mg ions around the vacancy. The electron (or the electrons in case of F^0 centers) is confined by the strong electrostatic potential of the ionic crystal (the Madelung potential) and de facto replaces the missing O^{2-} ion. F centers in 0, +1, or +2 charge states introduce new electronic levels in the gap of MgO (see, e.g., Figure 21) and can be detected by modern spectroscopies and microscopies, as will be discussed in section 4.1.

It is quite natural that the notion of electrons trapped at the MgO surface was originally attributed to the presence of F centers formed during the irradiation process. The extension of the notion of bulk F^+ center to the surface was made explicit by Tench who, in 1971, suggested that F^+ centers can exist also at the terraces of MgO, thus providing a possible explanation for the high reactivity of the irradiated samples.⁵² The Tench model of a surface F^+ center was followed a few years later by the first theoretical description of the electronic structure of this surface defect by Sharma and Stoneham.⁵³ Using molecular orbital Hartree–Fock calculations and a pioneering cluster model approach where a small number of ions was described in detail and the rest was represented by appropriate point charges, it was possible to compute spin-resonance parameters in reasonable agreement with experiment, thus providing support to the model of electrons trapped at anion vacancies at the surface of an ionic oxide. Thanks to these and other studies, around 1970 the notion of electrons trapped at the

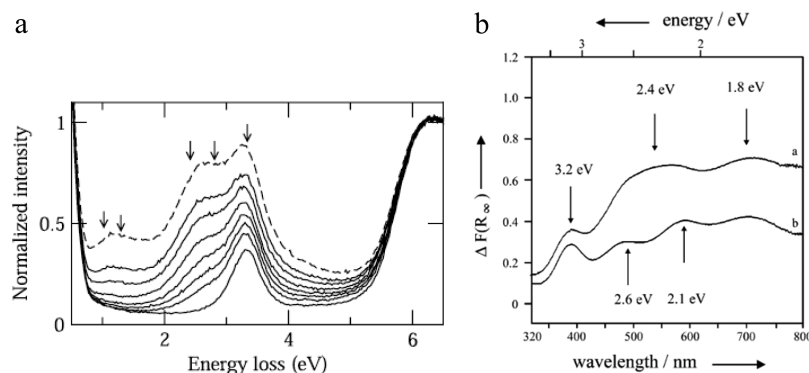


Figure 6. (a) EEL spectra of a MgO thin film after electron bombardment to create oxygen vacancies on the surface.⁴⁷ Reproduced with permission from ref 47. Copyright 2002 Elsevier. (b) Diffuse reflectance spectra of MgO powder activated with UV light under H₂ pressure: the two curves (a) and (b) have been obtained before and after 5 min of thermal treatment at 400 K under vacuum conditions, showing the thermal stability of the generated color centers.^{60a} Reproduced with permission from ref 60a. Copyright 1999 Elsevier.

MgO surface was intimately connected with that of anion vacancies or F centers.

Parallel and even prior to the application of EPR to the study of paramagnetic F centers in MgO is the study of the optical properties of these defects.⁵⁴ In fact, electrons confined in a trapping potential can give rise to specific electronic transitions and optical spectra. The first measurements of intense optical absorption bands in X-ray irradiated MgO samples go back to 1950,^{54a} although a complete assignment was obtained only about 20 years later by combining photoluminescence and EPR measurements.^{54c} Two optical absorptions at 4.96 and 5.03 eV were attributed to bulk F⁺ and F⁰ centers generated by additive coloring experiments performed by exposing a MgO single crystal to Mg vapor at high temperature and pressure.⁵⁵ More or less at the same time, the first measurements of the optical transitions of a surface F⁺ center by diffuse reflectance were reported on MgO powder samples obtained by decomposition of carbonates.⁵⁶ Despite the absence of irradiation, an intense absorption band at 2.05 eV was observed and attributed to surface F⁺ centers.⁵⁶ This assignment was later supported by electron energy loss (EEL) spectra on vacuum-cleaved MgO(001) single-crystal surfaces where a broad feature at 2.3 eV connected to surface defects was tentatively attributed to F centers.⁵⁷ The same band was observed on MgO(001) surfaces after electron bombardment, although it was tentatively assigned to Mg vacancies instead of O vacancies.⁵⁸ These, and other studies, suggested that a typical signature of the presence of trapped electrons at surface vacancies in MgO is the appearance of optical absorption bands around 2–3 eV. More recent studies on the properties of variously prepared MgO surfaces (polycrystalline or thin films) support this view. After growing epitaxial ultrathin films of MgO on Ag(001) single crystals, Pfnür and co-workers showed that two features at 2.1 and 3.3 eV are clearly associated to O deficient centers (Figure 6a).^{47,59} It is interestingly to note that very similar absorption bands have been measured after UV irradiation of MgO polycrystalline samples under hydrogen pressure (Figure 6b); in this case bands at 1.8, 2.4, and 3.2 eV were observed and assigned to electrons trapped at specific oxygen vacancies.⁶⁰ We will see below that the origin of these bands is different and is indeed related to a new class of surface electron traps (section 3.5).

The measured optical absorption bands have been supported and corroborated by advanced calculations. Using embedded cluster models and explicitly correlated wave functions, the

optical transitions associated to F centers in the bulk or on the surface of MgO have been calculated, confirming that F and F⁺ centers at low-coordinated surface sites have allowed optical transitions around 2–3 eV, i.e., well below the corresponding bulk transition.⁶¹ Thus, specific optical absorption bands are associated to well-defined surface defects present on variously prepared MgO samples, from powders to ultrathin films and even single crystals. These bands are consistent with the presence of F or F⁺ centers, a fact that, for a long time, has contributed to reinforce the idea of an ubiquitous presence of these defects on the surface of this material.

The chemical nature and the electronic structure of MgO bulk and surface F centers found a new wave of interest in the last decade of the last century. This was also thanks to the rapid development of advanced computational tools and algorithms accompanied by a spectacular increase in computing power and by the appearance of new experimental tools to characterize oxide surfaces. In the decade starting from 1990 till the past few years, several computational and experimental studies have been reported on the properties of these defect centers and of their reactivity toward atoms, molecules, and supported clusters.⁶² For instance, by using high-resolution electron energy loss (HREELS), Goodman and co-workers concluded that the activity of Li-promoted MgO catalysts is intimately connected to the presence of F centers and suggested that F centers are directly responsible for the methane-activation step.^{62a,63} A novel tool to identify the presence of oxygen-deficient centers in MgO surfaces was also proposed by Goodman and co-workers.⁶⁴ This is based on the already mentioned MIES spectroscopy, an extremely surface-sensitive, but hard to quantitatively interpret, technique, which has been successful in probing the topmost layer of insulating surfaces both with and without adsorbates by fingerprinting. In a series of studies, MIES was used for the detection of surface defects on MgO(001) thin films. A typical example of the information that can be derived from MIES is shown in Figure 7. MIES and ultraviolet photoemission (UPS) spectra were acquired on the same sample of MgO films, as-prepared and after electron bombardment. For the as-prepared films the results show the typical O 2p derived valence band structure with a gap of about 6.7 eV, free from any structure in the band gap. However, upon electron bombardment a new feature appears at about 2 eV above the top of the valence band (Figure 7). The band disappears immediately upon exposure to small amounts of oxygen, indicating that oxygen-deficient centers must be the

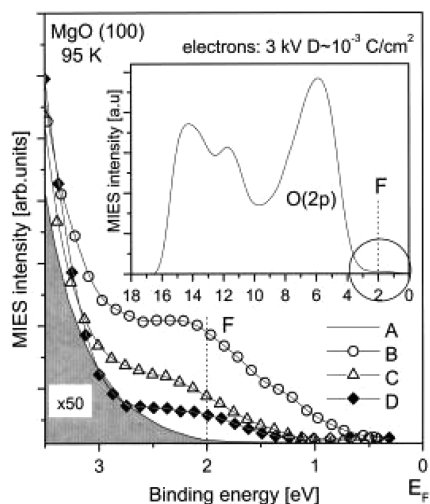


Figure 7. MIES spectra of a MgO(001) film following electron bombardment and oxygen treatment. (A) As-prepared MgO film. (B) Film in spectrum A after bombardment with 3 kV electrons. (C) UPS spectrum acquired concomitantly with spectrum B. (D) MIES spectrum of electron-treated film B exposed to oxygen. The total MIES spectrum B is shown in the inset.^{64a} Reproduced with permission from ref 64a. Copyright 2000 American Institute of Physics.

origin of the new feature. Given the extreme surface-sensitivity of both MIES and UPS spectra, these centers must be located at the surface or subsurface regions. The new bands observed in MIES were assigned to Auger de-excitation from newly created F centers or F center aggregates.^{64a}

Thanks to electronic structure theory, important results and notions were gained, such as the role of the Madelung potential in trapping one (F^+) or two (F^0) electrons in the oxygen vacancy;⁶⁵ the lower formation energy of F centers at low-coordinated sites like corners, steps, or edges, compared to the (001) terraces;⁶⁶ the tendency of F centers to migrate with relatively small barriers from terraces to step edges; etc. (see also section 4.2).⁶⁷ The nature of the trapped electrons was also described in a more rigorous way based on the electron localization function (ELF) approach, showing that MgO F centers are clear quantum subsystems, definitely characterized by a high degree of electronic localization (Figure 8).⁶⁸ Theory

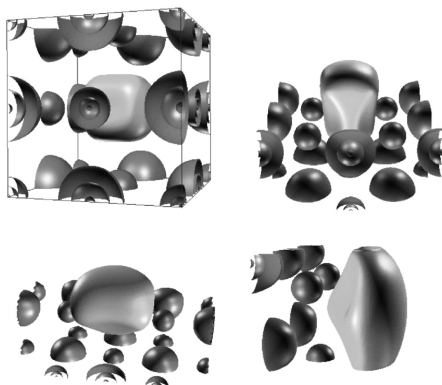


Figure 8. Electron localization function domains of the F center in the bulk (top left), bare surface (top right), step (bottom left), and corner (bottom right) in MgO.⁶⁸ Reproduced with permission from ref 68. Copyright American Physical Society 2002.

was helpful as well to assign spectroscopic features, for example, the already mentioned optical or EPR spectra, so as to identify the mechanism of ET from an F center to adsorbates such as O_2 or CO with formation of stable O_2^- or metastable CO^- radical anions.⁶⁹ Finally, theory showed that F centers may bind metal atoms and metal clusters much more strongly than regular sites of the surface, thus acting as nucleation centers for the growth of small metal particles.⁷⁰

The idea that F centers play a direct and important role in the activation of supported metal nanoparticles on oxide surfaces found strong support by UHV experiments performed by the group of Heiz and co-workers.⁷¹ Using a source of mass-selected gas-phase metal clusters, it was possible to deposit, for the first time, on a surface a well-defined ensemble of monodisperse metal nanoparticles, i.e., all particles having the same size at least before deposition. In particular, using a soft landing technique in order to avoid cluster fragmentation and surface damage, a flux of Au or Pd clusters was deposited on MgO thin films grown on a Mo(001) metal support. Small gas-phase molecules like CO or C_2H_2 were then introduced in the UHV chamber, and their reactivity was studied as a function of the cluster size and of the nature of the oxide support, “defect-free” or “defect-rich”. Two important observations emerged. Clusters of different sizes exhibit different reactivities, to the point that, while a MgO supported Au_7 cluster is inactive in CO to CO_2 oxidation, a Au_8 cluster converts CO to CO_2 efficiently at low temperature.^{71a} The second important result was that the oxide surface is not innocent and that different reactivities are detected when the clusters are deposited on defect-rich or defect-poor MgO supports.^{71a,b} In particular, although a Au_8 cluster or a Pd atom is essentially inert when deposited on a defect-free MgO support, a clear catalytic activity was observed when the same metal nanocatalysts were deposited on a highly defective MgO film.^{71a,b} To explain the observation, it was suggested that the defects responsible for the different reactivities are F centers. Specific models were constructed to calculate, based upon first principles electronic structure methods, the reactivities of the supported clusters.^{71a-c} The calculations provided evidence that if electronic charge is transferred from the defect sites to the metal nanoparticle the reactivity is enhanced and suggested that the F centers at the surface of MgO are the sites relevant to turn inactive neutral clusters in catalytic active negatively charged units. In fact, the electrons bound to F centers can be easily transferred to the deposited atoms or clusters with substantial increase of their electron density. The increased electronic charge on the metal nanocluster ($Au^{\delta-}$ or $Pd^{\delta-}$) results in easier bond activation and bond breaking, leading to the low-temperature formation of products such as CO_2 from CO and O_2 ^{71a,c} or benzene starting from acetylene (cyclotrimerization reaction $3 C_2H_2 \rightarrow C_6H_6$).^{71b} No direct evidence that F centers are involved in the process could be provided at the time of these experiments, but nevertheless the results contributed significantly to spread the idea of a dominant role of oxygen vacancies in the surface chemistry of MgO.

A few years later Yan et al.⁷² reported that Au nanoparticles grafted to the surface of MgO powders annealed to temperatures between 900 and 1300 K prior to deposition of the Au clusters exhibit rather different reactivities in CO oxidation depending on the concentration of F centers at the surface of the oxide grains. Also in this case the evidence of the presence of F centers was indirect, but the results were again pointing toward a special role of these defects in catalysis by

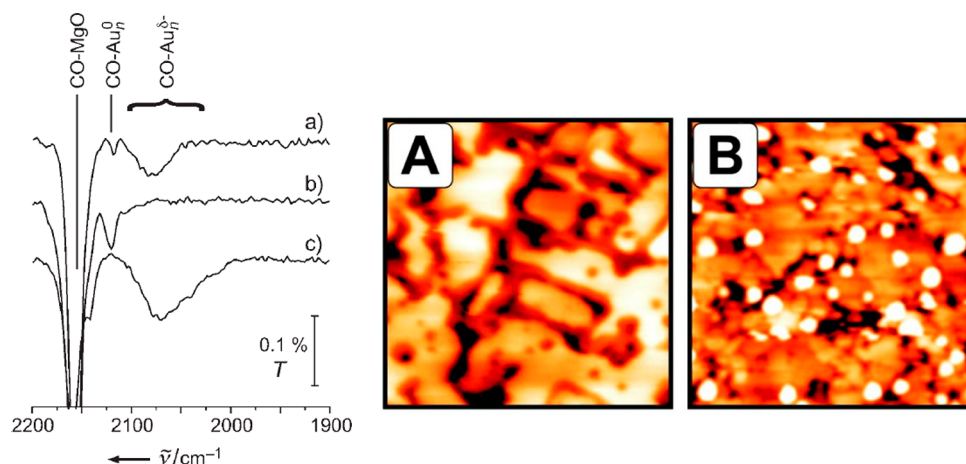


Figure 9. (Left) IR spectra of CO on Au clusters deposited on differently pretreated MgO films: (a) film after medium-dose electron bombardment and deposition of 0.05 ML Au at 30 K; (b) pristine MgO film after deposition of 0.025 ML Au at 80 K; (c) film after high-dose electron bombardment and deposition of 0.025 ML Au at 30 K.⁷⁴ Reproduced with permission from ref 74. Copyright 2006 Wiley-VCH. (Right) STM topographic images of 7 ML thick MgO films grown on Mo(001), before (A) and after (B) deposition of 0.06 ML Au ($50 \times 50 \text{ nm}^2$). The bright spots correspond to Au nanoparticles nucleated along the step edges of the MgO film.⁷⁶ Reproduced with permission from ref 76. Copyright 2007 American Chemical Society.

metals supported on MgO. Whereas the work of Heiz and co-workers^{71a,b} was referring to model systems (MgO thin films in UHV conditions), the experiments of Yan et al.⁷² were dealing with MgO powders prepared under realistic conditions, suggesting that the same type of defects, in particular the F centers, are present in the two cases.

The fact that F centers do indeed contribute to enhance the electronic charge on the supported metal nanoparticles has been predicted theoretically⁷³ and demonstrated by a series of experiments specifically designed for this purpose.⁷⁴ MgO films have been prepared, and gold nanoparticles have been deposited on them. In those experiments, the charge on the Au-nanoparticles was monitored indirectly by measuring the stretching frequency of adsorbed CO molecules (Figure 9). On a defect-free MgO surface the Au clusters are in zero oxidation state and the CO frequency is 2120 cm^{-1} , as for CO on gold single-crystal surfaces (2110 cm^{-1}).⁷⁵ When the MgO surface is damaged by electron bombardment, which results in the formation of oxygen vacancies (F centers), the frequency of CO adsorbed on the Au clusters is red-shifted to 2070 cm^{-1} ,⁷⁴ typical of CO adsorbed on negatively charged Au clusters.^{71c} The negative charge is that provided by the F centers where the clusters reside, as predicted via electronic structure calculations and shown by scanning tunneling microscope (STM) experiments.⁷⁶ In particular, electroluminescence measurements have been performed with a STM to study the growth of Au particles on thin MgO films on Mo(001). With increasing Au coverage, a rapid quenching of the characteristic, defect-related MgO emission was observed. The fast attenuation of the MgO signal with metal exposure indicates that Au nucleation preferentially takes place at the optically active centers in the MgO surface. The nucleation sites have been identified in STM measurements as F centers located along the step edges of the MgO surface (Figure 9).⁷⁶

Another strong proof that the nucleation of gold clusters occurs preferentially on F centers comes from EPR. Surface color centers on a thin, epitaxially grown MgO(001) film on Mo(001) were investigated under UHV conditions by EPR spectroscopy.⁷⁷ For the investigation of paramagnetic species on single-crystal surfaces, absolute sensitivity is of paramount

importance. EPR spectroscopy has the necessary sensitivity to detect paramagnetic species at submonolayer coverage under UHV conditions with a minimal sensitivity of 10^{12} spins. The pristine MgO films exhibit no EPR signal, and the number of singly charged color centers must thus be lower than 1×10^{12} on this surface. Paramagnetic color centers, however, have been produced by exposing the pristine film to electrons with an energy of 100 eV (Figure 10). The generation of color centers

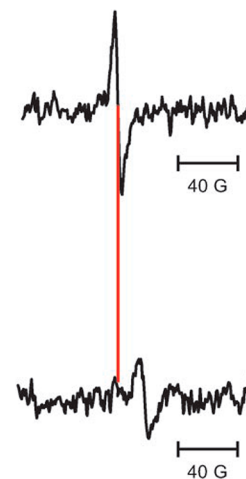


Figure 10. (Top) EPR spectra of MgO/Mo(001) film after low-dose electron bombardment; the spectrum corresponds to F^+ color centers formed at step or edges of the MgO islands. (Bottom) The same preparation after deposition of 0.015 ML Au at 30 K. The red line indicates the position of the color-center signal in both spectra.⁷⁴ Reproduced with permission from ref 74. Copyright 2006 Wiley-VCH.

in such a way was shown by specific losses observed in the EELS spectrum of MgO films grown on Ag(001).^{59b} The defect generation by electron bombardment is due to electron-stimulated desorption of oxygen atoms or ions via a multielectron Auger decay. As reported above, STM images show that the majority of the defects are located at the edges and corners of the islands rather than on the regular (001) surface,⁷⁷ consistent with the lower formation energy of O

vacancies on these sites.⁶⁶ The analysis of the principal components of the g tensor confirmed the presence of the F^+ paramagnetic centers at the low-coordinated edge or step sites of the MgO islands.^{77,78}

If nucleation of gold clusters involves F or F^+ centers, this should result in a change of the corresponding EPR signal. This is indeed what has been observed.⁷⁴ The upper trace in Figure 10 shows the EPR spectrum around the free-electron g -value of a 20 monolayer (ML) thick, single crystalline MgO/Mo(001) film after bombardment with electrons. After deposition of 0.015 ML of Au at 30 K, the EPR signal of the color center is quenched (Figure 10).⁷⁴ This is a direct consequence of the nucleation of Au at the color centers. This behavior arises from the coupling of the doublet ground states of the color center and the Au atom to a singlet ground state of the adsorption complex. The quenching of the signal is also consistent with the formation of small Au clusters at these sites, as seen by STM. Concomitant to the decrease of the color-center signal, a new EPR signal appears at higher field. This line is part of a quartet of lines with a large isotropic hyperfine-coupling constant of about 49.5 mT, which is characteristic of single Au atoms. A detailed analysis of angular dependence of the signals shows that these Au atoms are nucleated on the terraces of the MgO film, directly above the oxygen ions.⁷⁹

The relatively high number of modeling studies dedicated to this topic, associated to the experimental evidence of the role of oxygen vacancies, when present, in the activation of supported metal nanoparticles, greatly contributed to consolidate in the community the idea that F centers are present in relatively high concentrations on the surface of as-prepared MgO samples and have, therefore, a dominant role in the surface chemistry of this oxide. We have seen already that more recent results obtained in the past decade show, on the contrary, that the number of F centers on the MgO surface is very low, unless the surface is specifically treated to induce oxygen deficiency. Actually, we will show later that F centers alone cannot explain many of the observed features in MgO chemical reactivity and that new centers have to be considered to fully account for the electron transfer properties of this system.

3.4. From the F Center Model to $F_S(H^+)$ Defects

The revision of the widely accepted model of the surface F center required more than a decade and finds its roots in an experimental observation that, for the first time, indicated the need for a more refined structural model of electrons trapped at the MgO surface. In 1989, Giamello and co-workers, studying the formation of radical species by exposure of MgO powders to O_2 , found that the resulting superoxo ion, O_2^- , gives rise to a splitting in the EPR signal due to the interaction with a vicinal proton.⁸⁰ The data were clearly indicating a direct interaction of the superoxo O_2^- ion with an OH group in the immediate vicinity, an observation that was possible thanks to the improved resolution of EPR spectroscopy from the time of the early experiments of Tench⁵² and Lunsford and Jayne.¹¹ This observation, later confirmed by new and more conclusive experiments, prompted the formulation of a new model of surface F centers in MgO capable of accounting for the new data.⁸¹ By comparing the isotropic hyperfine coupling constants, a_{iso} , of the trapped electron in F^+ with both the Mg and 1H nuclei measured from EPR spectra^{11b} or computed with ab initio methods, it was proposed that a proton must be adsorbed on one of the surface oxygens adjacent to the O vacancy.⁸¹ This center was named $F_S(H^+)$, where S indicates

the location of the vacancy on the surface and (H) indicates the presence of the proton. Calculations showed that the proton polarizes the electron density toward one or two Mg ions of the vacancy, leading to an $a_{iso}(^{25}Mg)$ value of about 1.0–1.2 mT for the new $F_S(H^+)$ defect. Given a measured $a_{iso}(^{25}Mg)$ of 1.1 mT,⁸¹ it is not surprising that the agreement was considered very satisfactory and the model was considered realistic. Furthermore, also the weak but relevant hyperfine interaction with the nearby proton was reproduced quite accurately, reinforcing the $F_S(H^+)$ model. The success of this model was further consolidated by the interesting observation that electrons trapped at the surface of polycrystalline MgO, prepared following specific recipes, can be transferred to N_2 molecules with formation of a metastable N_2^- ion, a first step in the mechanism of nitrogen fixation.⁸² The observed reversible formation of N_2^- was explained with an ET occurring from $F_S(H^+)$ to adsorbed nitrogen molecules. However, we will see that the $F_S(H^+)$ center is only one step toward the real nature of trapped electrons, but not the final model yet.

The $F_S(H^+)$ model of a trapped electron was definitely an improvement with respect to the classical one but was still related to the idea that an O atom has been removed from a regular site of the surface. In this respect, it can be considered as a revision of the Tench model without replacing it entirely. However, despite a general consensus and a number of indirect pieces of evidence based on the comparison of computed and measured data,^{60a,83} some doubts about the validity of the F center model started to emerge. The first one is of purely energetic nature. The thermodynamic cost to create an O vacancy in MgO is relatively high. First principles calculations show that the removal of a neutral O atom from the (001) terraces costs between 9 and 10 eV, depending on the method used.^{44a,84} This value decreases by 2.6 eV if one considers as a reference $1/2O_2$ instead of an O atom, but still we are talking about a formation energy of nearly 7 eV. Lower formation energies have been computed for the removal of O atoms from low-coordinated edge, step, or corner sites, but the computed values are never below 4–5 eV (with respect to the formation of molecular O_2).^{66,84a} Even higher, and more difficult to evaluate, are the formation energies of F^+ and F^{2+} centers, posing, due to their positive charge, questions related to the electroneutrality of the system. Furthermore, F^+ and F^{2+} centers imply that other defects must be present to provide an electrical compensation mechanism. No evidence of the presence of such compensating defects has ever been reported, leaving the question open. Even considering entropy effects, the highly positive enthalpy contribution indicates that the number of defect centers present on the surface of the material in conditions of thermodynamic equilibrium should be too small to justify the occurrence of the observed ET processes and the formation of high concentrations of radical species.

3.5. Electron-Rich Surfaces: New Models of Surface Traps

Despite the apparent success of the F center notion to explain processes and ET phenomena on MgO surfaces, some specific details of accurate measurements were not easy to reconcile with the classical Tench model⁵² or its more recent variants.⁸¹ In particular, referring to paramagnetic centers, some EPR properties were not entirely consistent with the F center model. For instance, ab initio calculations gave for the classical F_S^+ surface center an $a_{iso}(^{25}Mg)$ value of about 0.5 mT, only slightly larger than that measured in the bulk, 0.4 mT. However, this hyperfine coupling constant is about one-half of that measured

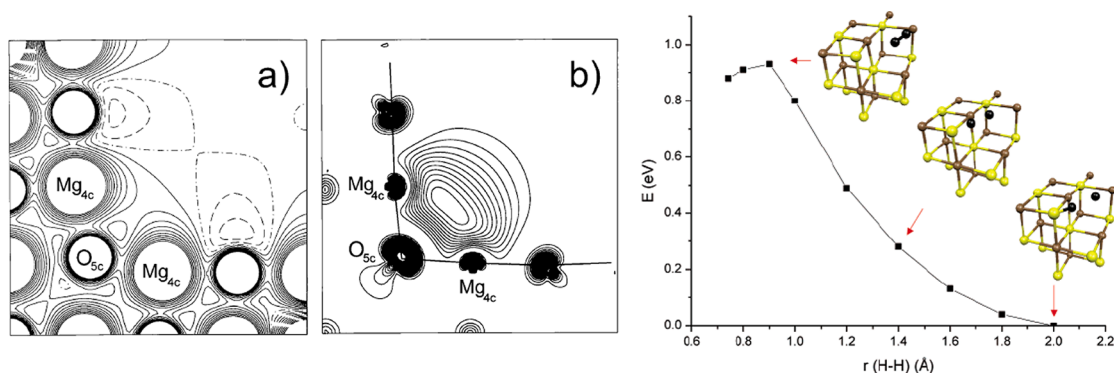


Figure 11. (Left) (a) Electrostatic potential of a reverse corner on the MgO surface plotted in the top layer; solid, dashed, and solid–dashed curves refer to positive, negative, and zero potential, respectively; (b) spin density map of an electron trapped at the reverse corner site. (Right) Section of the potential energy surface for the interaction of H_2 with a $\text{Mg}_{10}\text{O}_{10}$ cluster model of a reverse corner site, MgO_{RC} . For each fixed H–H distance, the rest of the geometrical parameters have been reoptimized. The position of the H atoms (black spheres) for three structures is shown.^{87a} Reproduced with permission from ref 87a. Copyright 2003 American Chemical Society.

in the dominant EPR signal of MgO powder samples (1.1 mT).⁸¹ A 0.5 mT value for the hyperfine interaction with Mg has never been observed in experiments. Given the relatively small value of the hyperfine interaction, this discrepancy was attributed to the approximations inherent to the ab initio calculations. To rationalize the observed $a_{\text{iso}}(^{25}\text{Mg}) = 1.1$ mT, the new model of a $\text{F}_s(\text{H})^+$ defect had to be proposed, where a proton is adsorbed in the vicinity of the trapped electron.⁸¹ This led to the conclusion that trapped electrons exist *only* in combination with OH groups, and that if classical F^+ centers with no protons in the vicinity exist, their number must be below the detection limit of a very sensitive technique like EPR.

The absence of a direct proof of the existence of “classical” F^+ centers in MgO polycrystalline samples together with their high formation energies and charge neutralization problems, prompted the search of other possible electron trapping sites at the MgO surface. One potential candidate considered is the divacancy, a defect consisting of a missing pair of adjacent Mg and O ions.^{62h,85} If created at the MgO terraces or steps, this results in a cavity whose electrostatic potential is able to trap one electron with a binding energy of 0.6 (terrace) or 1.1 eV (step), according to theoretical calculations.⁸⁶ The model of a divacancy is conceptually very different from that of a classical O vacancy. First of all, formally the removal of a pair of Mg and O atoms does not alter the stoichiometry of the sample but only results in new low-coordinated sites. This means that no extra electrons are associated to this center. Second, from an energy point of view, removing a neutral MgO unit has a lower cost than removing an O atom; furthermore, if one assumes that the two removed Mg and O atoms are simply displaced to some other region of the surface, one is dealing with a morphological defect with a low formation energy, which could result in large numbers of these defects. The capability of divacancies to trap electrons is directly connected to the presence of low-coordinated Mg ions, which, as we discussed in section 3.1, have low-energy 3s–3p acceptor levels that can thus act as Lewis acid sites.⁴¹ These observations pointed the attention to the role of low-coordinated sites, and in particular low-coordinated Mg cations, as potential sites where electrons can be trapped. However, the idea that divacancies at terraces or steps of the MgO surface can be the real sites where excess electrons are stabilized was not supported by a comparison of the measured and computed hyperfine constants: some

discrepancies remained, thus discarding this site as a good model to replace the F center model.⁸⁶

The search for a more realistic model of electron traps led also to reconsideration, in some detail, of how excess electrons are generated at the surface of MgO and what are the intermediate steps involved. A classical procedure to generate electron-rich MgO surfaces is of a physical type and consists of the irradiation of the material with high-energy photons (X-ray or UV). Electrons are excited from bound O 2p states in the bulk or on the surface into new accepting levels, creating electron–hole pairs. The electron, trapped at some specific sites, can give rise to the typical change in color of the sample due to the creation of color centers. However, the same result can be obtained using chemical methods in milder conditions. One approach is the addition of electron donor species to the MgO powder samples. By evaporating small amounts of Na on the surface of polycrystalline MgO, one observes in EPR spectra the formation of new paramagnetic centers consisting of a single electron bound to some specific site.⁸⁷ The same result can be obtained by exposing MgO powders to a plasma of H atoms.^{87b,88} Clearly, the Na or H atoms bind to the surface in the form of Na^+ or H^+ ions and release the valence electron, which populates a pre-existing trapping site. The same material can be prepared by using molecular H_2 , instead of atomic H, and irradiating the sample with UV light. In this case the formation of the paramagnetic color centers occurs in two steps: (i) the H_2 molecule interacts with the MgO surface and splits heterolytically into a proton, H^+ , bound to an O^{2-} site, and an hydride ion, H^- , bound to a Mg^{2+} site;⁸⁹ and (ii) an UV-photon excites the adsorbed hydride ion with desorption of a neutral H atom, leaving behind a trapped electron on a surface site:^{87,90}



The released H atom (reaction 8) can further react to produce another proton and an excess electron. Notice that all these processes are very fast and involve surface sites. This is demonstrated by the fact that the sample changes color (from white to pale blue) after exposure to alkali metals or hydrogen; however, if the sample is exposed to molecular oxygen, there is an instantaneous decoloration due to the ET of the trapped

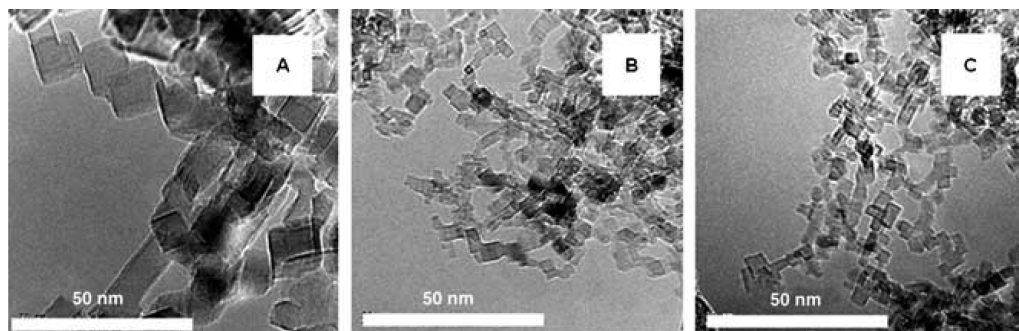
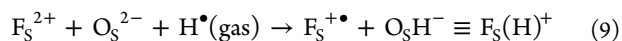


Figure 12. TEM images of MgO nanocubes of various average sizes prepared from CVD.^{39a} Reproduced with permission from ref 39a. Copyright 2005 Wiley-VCH.

electrons from the MgO surface to the O₂ molecules, with formation of adsorbed superoxo ions, O₂⁻.⁸⁷

For a long time it has been assumed that F centers are the natural candidates for the occurrence of the process. However, EPR spectra clearly indicate that the surface contains no trapped electrons *before* the exposure to hydrogen, whereas the typical signal of an electron interacting with both Mg and H ions is detected *after* contact of the MgO surface with hydrogen. If the generated centers would be paramagnetic F_S⁺ surface defects, this would imply that diamagnetic precursors, the empty F_S²⁺ vacancy sites, must exist on the surface:



In reaction 9 a neutral H atom from the gas phase splits into a proton, H⁺, which binds to a surface oxygen, O_S²⁻, to form a hydroxyl group, O_SH⁻, while the electron is donated to the strong accepting F_S²⁺ site, which transforms into a paramagnetic F_S^{+\bullet} defect center. If this latter defect is near the hydroxyl group, one is left with the F_S(H)⁺ center described above. In other words, the formation of such a paramagnetic center by interaction with hydrogen implies the existence of F_S²⁺ diamagnetic precursors. This poses some questions related (i) to the high formation energy of the F_S²⁺ precursor sites and (ii) to the large charge imbalance that would be associated to a significant number of F_S²⁺ centers. Clearly, the observed phenomena are difficult to be fully accounted for by the classical model of a surface O vacancy.

The solution of the problem lies in the analysis of the sites, which are capable to split the H₂ molecule heterolytically. Possible candidates (although not the only ones) are the four-coordinated Mg and O ions along the step or edge sites of MgO. Even better is the defect formed at the intersection of two MgO steps oriented perpendicular to each other. This has been named reverse corner, and it is the site that has been considered, initially, as a potential candidate to replace the F center model.⁸⁷ In a reverse corner (Figure 11), there are three Mg²⁺ cations, two Mg_{4c} and one Mg_{5c}, that generate a particularly strong electrostatic potential. This is sufficient to dissociate molecular hydrogen within a weakly activated exothermic process (the reaction occurs already at very low temperature, 77 K, and the energy gain, according to ab initio calculations, is about 0.5 eV, as confirmed by accurate calorimetric data on MgO powders).⁸⁷

This leads to the formation of two kinds of adsorbed H atoms, a proton, H⁺, bound to an O²⁻ ion, and an hydride ion, H⁻, bound to three Mg²⁺ cations (Figure 11). The formation of the two types of hydrogen ions is clearly shown by the appearance of the typical OH bands at 3500–3700 cm⁻¹ and

MgH bands at 1200–1300 cm⁻¹, respectively, in IR spectra.^{89a,91} What is formed on the surface are thus MgO_{RC}(H⁺)(H⁻) diamagnetic sites, where RC indicates the reverse corner site where the process has occurred and (H⁺) and (H⁻) are the species resulting from the heterolytic dissociation of H₂. The proton is bound to an O_{4c} ion along the step, while the hydride ion interacts with two Mg_{4c} and one Mg_{5c} ions that provide a strongly stabilizing environment for the negatively charged hydrogen. The next step consists of removing the H atom from the MgO_{RC}(H⁺)(H⁻) center, reaction 8. This costs about 3.5 eV, thus explaining the need for UV light for the stimulated H desorption. This process leaves on the surface a center where the place of the hydride ion is taken by a “free” electron, which, due to the strong electrostatic potential, does not recombine with the proton and remains trapped at the surface. The resulting MgO_{RC}(H⁺)(e⁻) center is neutral, is thermally stable, and has a high IP: the cost to remove the trapped electron is, in fact, 4.8 eV.^{87a} The reverse process, i.e., the attachment of an electron to the diamagnetic precursor site (the vertical EA of the MgO_{RC}(H⁺) center) is associated with an energy gain of 3.1 eV, showing that these are strong trapping sites. The MgO_{RC}(H⁺)(e⁻) center is thus a paramagnetic color center, with electronic transitions in the visible, stable at room temperature and above, which consists of a “free” electron near an OH group. These are all the typical features of the so-called F_S(H⁺) centers, with the important difference that the precursor is a rather abundant morphological defect on the MgO surface, not the unlikely F²⁺ center. The precursor site of the new MgO_{RC}(H⁺)(e⁻) color center, the reverse corner MgO_{RC}, is neutral, does not require the presence of compensating charges, and does not alter the stoichiometry of the sample, at variance with the O vacancy model.

Of course, the surface of an ionic oxide with cubic rock-salt structure like MgO does not only exhibit reverse corners as morphological defects. Transmission electron microscopy (TEM) images clearly show that MgO powders consist of condensed nanocrystals in the form of small cubes (Figure 12).^{39a} These have step, edge, corner, and kink sites characterized by the presence of low-coordinated ions. Thus, several extended and point defects exist on the surface of the material, with the characteristics potentially required for the generation of the MgO(H⁺)(e⁻) centers. If the mechanism described previously for the generation of the trapped electrons works for reverse corners, there is no reason to believe that it is restricted to these special sites. Indeed, theoretical calculations have shown that the process of dissociating H₂ molecules followed by UV irradiation results in the formation of MgO(H⁺)(e⁻) centers also at sites like edges and corners,

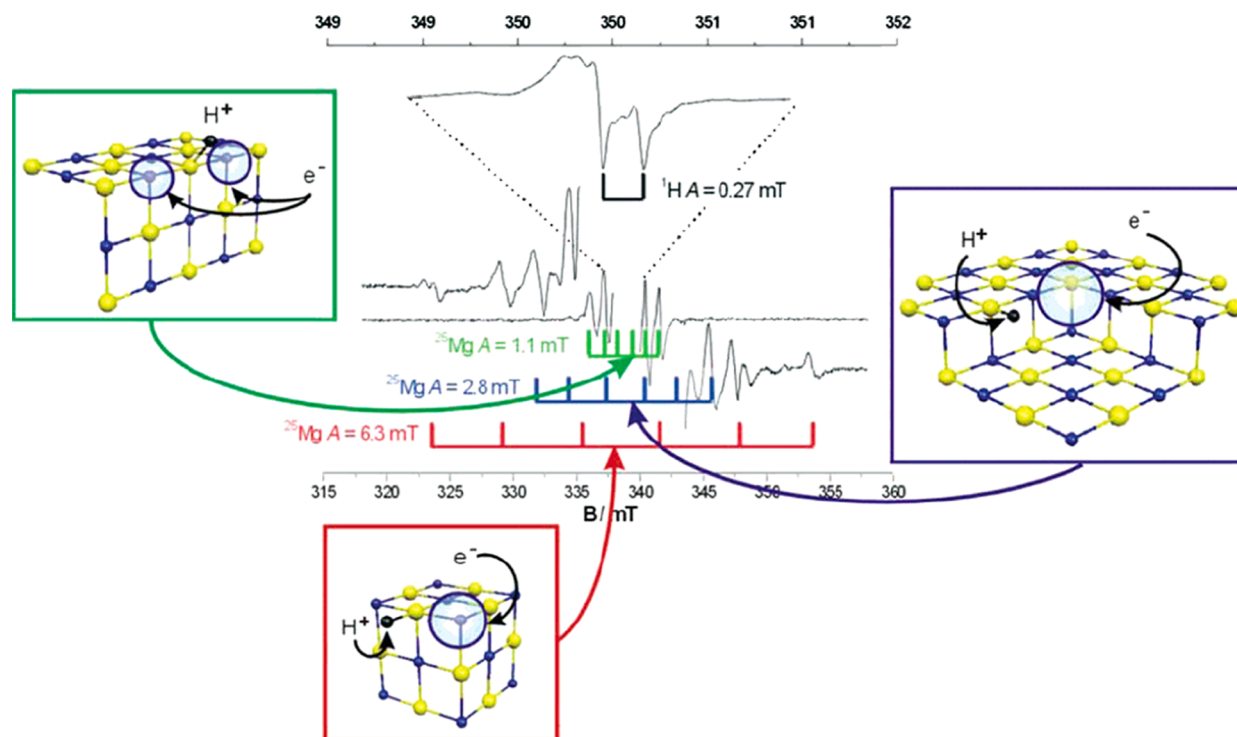


Figure 13. EPR spectra and atomistic models of $(\text{H}^+)(\text{e}^-)$ centers on MgO. The various lines in the EPR spectrum are assigned to $(\text{H}^+)(\text{e}^-)$ centers formed at steps (green), reverse corners (blue), and corners (red) sites.^{87b} Reproduced with permission from ref 87b. Copyright 2006 American Chemical Society.

and that in principle a whole family of electrons trapped near adsorbed protons should exist.^{87b,90a}

The direct, and final, proof of the existence of a variety of trapping sites where $(\text{H}^+)(\text{e}^-)$ centers can be formed came once more from EPR. In particular, an important observation was made by looking at the ^{25}Mg hyperfine coupling constants in high-resolution EPR spectra of MgO powders exposed to H_2 under UV irradiation. Three distinct ^{25}Mg hyperfine patterns could be observed, with couplings of 1.1, 3.0, and 6.0 mT (see colored stick diagram in Figure 13). The 1.1 mT signal is the one already observed in several previous spectra and tentatively assigned to the $\text{F}_s^+(\text{H}^+)$ center discussed above.⁸¹ Particularly surprising was the finding of the large hyperfine sextets (3.0 and 6.0 mT),^{87a,92} which are clearly hard to reconcile with the classical de Boer model of an electron trapped in an O vacancy of bulk MgO. In particular, the largest value of 6.0 mT indicates the interaction of the trapped electron with at most one Mg cation; also the hyperfine splitting of 3.0 mT was unprecedented, clearly indicating the need of a new model of electron traps. The only reasonable explanation for the 6.0 mT coupling was that the unpaired electron spin density is localized on a single $^{25}\text{Mg}^{2+}$ cation at an exposed site.⁹² Cluster model density functional theory (DFT) calculations confirmed this hypothesis and revealed that excess electrons were indeed stabilized by the large electrostatic potential provided by a corner or kink Mg_{3c}^{2+} ion and a nearby proton, predicting for this site a ^{25}Mg hyperfine coupling constant of 6.1 mT, in quantitative agreement with the experiment.⁹² The origin of the 3.0 mT signal was easily found in the reverse corner model described above, which results in a single trapped electron interacting with two Mg_{4c} cations, giving rise to a computed hyperfine constant of 3.0 mT, again in excellent agreement with the observed value.^{87a}

Far more problematic was the assignment of the 1.1 mT ^{25}Mg hyperfine pattern, which is also the most intense signal. The magnitude of this coupling could be equally reproduced, by ab initio calculations, using two drastically different models, the $\text{F}_s^+(\text{H}^+)$ center discussed above⁸¹ and the $(\text{H}^+)(\text{e}^-)$ pairs model localized at surface edges and steps, $\text{MgO}_{\text{edge}}(\text{H}^+)(\text{e}^-)$.^{87a} Although the energetic and electrostatic considerations clearly favor the second model, the final definitive assignment was only achieved by performing a number of experiments using a MgO surface enriched with ^{17}O ($I = 5/2$).⁹³ Enrichment was achieved by repeated hydration/dehydration cycles of high surface area MgO using H_2^{17}O . In this way the unpaired electron spin density distribution could be monitored over the constituent O^{2-} ions of the surface electron trap. The EPR spectrum of ^{17}O -enriched MgO is dominated by two ^{17}O hyperfine sextets arising from the interaction of the unpaired electron with two, magnetically nonequivalent, ^{17}O nuclei assigned to an OH^- group, with the larger ^{17}O hyperfine coupling, and to a surface O^{2-} lattice anion. This result demonstrated unambiguously that only the $(\text{H}^+)(\text{e}^-)$ pairs model, based at surface steps or edges, is consistent with the experimental data, because the ^{17}O hyperfine couplings for the $\text{F}_s^+(\text{H}^+)$ model were far too small.⁹³

3.6. Electron Traps at Hydroxylated MgO Surfaces

The $(\text{H}^+)(\text{e}^-)$ centers described above consist of a “free” electron confined by the electrostatic potential provided by one or more exposed Mg^{2+} cations and by the proton of a hydroxyl group, OH. This raises an important question about the role of hydroxyl groups on oxide surfaces as potential sites where electrons can be bound. Hydroxyl groups are always present on oxide surfaces as the result of the spontaneous dissociation of water at reactive sites of the surface. Even in UHV conditions, traces of water are present that are sufficient to decorate, by

some OH groups, the oxide step edges. The role of OH groups in oxides chemistry cannot be underestimated. A considerable body of literature shows that the reactivity of “clean”, OH-free, and hydroxylated surfaces can be drastically different.⁹⁴ For instance, OH groups are important to stabilize⁹⁵ or to induce oxidation of supported metal clusters,⁹⁶ or may give rise to reverse hydrogen spillover phenomena with hydrogen transfer from an OH unit to the supported cluster.⁹⁷ In principle, OH groups therefore represent ideal precursor sites for the generation of trapped electrons at the surface of ionic oxides. This process has been demonstrated in an elegant experiment.⁹⁸

Fully dehydrated high-surface area MgO, CaO, and SrO samples have been prepared by decomposition of the corresponding hydroxides or carbonates followed by thermal activation at 1173 K. This produces virtually OH-free samples, which have been exposed to low amounts of Na vapors. The result is a change in color of the sample, which turns pale blue, and the appearance of a typical EPR spectrum (Figure 14a),

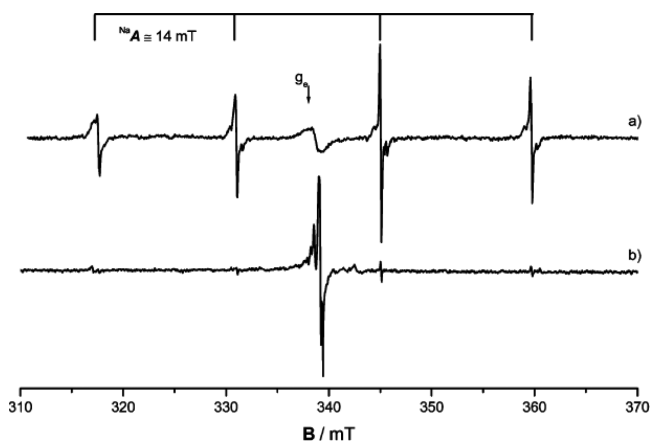


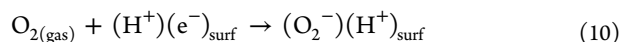
Figure 14. EPR spectra of Na atoms adsorbed on (a) fully dehydrated and (b) partially hydroxylated MgO. Both spectra were recorded at 77 K.⁹⁸ Reproduced with permission from ref 98. Copyright 2007 American Chemical Society.

which consists of a quartet of lines separated by about 14 mT. This is the signature of the interaction of an unpaired electron wave function with a Na nucleus. The same experiment has been repeated with MgO, CaO, or SrO samples dehydrated at 1073 K, a temperature that preserves a few OH groups on the surface, as demonstrated by the typical signal in IR spectra. The EPR spectrum of partially dehydrated MgO exposed to Na vapors is shown in Figure 14b and is completely different from that of the fully dehydroxylated sample (Figure 14a). The hyperfine quartet of lines due to adsorbed Na atoms is almost absent while the intensity of a feature with $g \approx 2$ clearly dominates the spectrum. This feature is present also in the spectrum of the dehydrated sample (Figure 14a), where it is very weak and superposed with other features, probably due to the formation of tiny amounts of Na clusters. The analysis of the central line in the spectrum of Figure 14b allows one to identify a 1:1 correspondence with the spectrum of the $(\text{H}^+)(\text{e}^-)$ centers obtained by exposing the MgO powders to H_2 under UV irradiation.^{87a} From the intensity of the signal a concentration of about 7×10^{11} spins/cm² is estimated. The origin of the two different features has been explained with the help of quantum chemical models. On the fully dehydrated samples, low amounts of Na are deposited in the form of free

atoms. These are stabilized as neutral entities on various sites of the surface. As demonstrated also for Li and K atoms, the valence electron is polarized by the interaction with the surface, but no ionization of the alkali atom occurs.⁹⁹ A tiny amount of alkali atoms is ionized by specific defects (oxygen vacancies?), but the concentration of these centers is orders of magnitude smaller than that of the Na adatoms. The quartet of lines observed is typical of a polarized adsorbed Na atom. The situation is completely different when OH groups are present on the surface. Here a spontaneous ionization of the Na atom with formation of a Na^+ cation and an extra electron occurs. The reaction is exothermic if the excess electron is stabilized near a hydroxyl group, forming a $(\text{H}^+)(\text{e}^-)$ center. This shows that the hydroxyl groups at the surface of ionic oxides, such as MgO, CaO, or SrO, are potential trapping sites for electrons generated by adding metal atoms with low ionization potential, or by generating electron–hole pairs by irradiation with UV light.

These results lead to a very important conclusion: there is no need to invoke the presence of anion vacancies to explain the large amount of trapped electrons observed in experiments. It is sufficient that on the surface traces of OH groups are present to create the conditions for binding electrons. These may be provided by highly reducing chemical species, such as hydrogen or alkali atoms, or simply by generation of electron–hole pairs under irradiation. *What has been a strong belief for several decades, the idea that electrons trapped at the surface of ionic oxides must be intimately connected to the presence of anion vacancies, is no longer valid, as more natural and abundant candidates exist to explain the same phenomenon.* This does not exclude the presence of low amounts of F centers, but these form only under special conditions, like a severe damage of the oxide surface by electron bombardment, the exposure to high-energy photons, or a drastic dehydroxylation at high temperature. On the contrary, $(\text{H}^+)(\text{e}^-)$ centers are not exotic sites that need to be created by sophisticated experiments. Their amount can be rather high and may lead to situations where electrons are “solvated” in a way that is reminiscent of solvated electrons in liquid ammonia.¹⁰⁰

Not surprisingly, the surface of MgO decorated by electron–proton pairs is an extremely reactive system. Molecules exposed to the electron-rich surface are easily reduced to the corresponding radical anion, via electron transfer. There are several examples for this reactivity; for instance, CO_2 interacts with electron-rich MgO surfaces to form carboxylate radical anions, and ¹⁰¹ SO_2 molecules adsorbed on electron-enriched surfaces of MgO and CaO show the formation of two paramagnetic products identified via EPR as SO_2^- and S_2O^- radicals whose abundance depends on the surface oxide properties (in particular, higher basicity and higher number of defects in the case of CaO lead to a higher amount of these two radical species).¹⁰² However, two cases are particularly relevant for the present discussion and well-represent the kind of ET reactivity that can be expected on these surfaces. The first case is that of molecular oxygen, which readily reacts with surface excess electron centers to form the superoxide O_2^- radical ion.^{89b,103} O_2^- is stabilized on the surface in proximity to the adsorbed proton (hydroxyl group) of the trapped electron center, according to the following reaction:



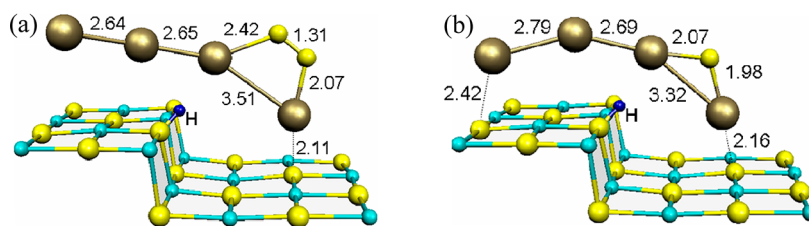
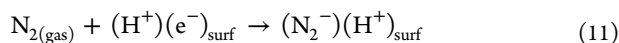


Figure 15. Structure of (a) $\text{MgO}(\text{H}^+)(\text{Au}_4/\text{O}_2^-)$ surface complex and (b) $\text{MgO}(\text{H}^+)(\text{Au}_4/\text{O}^-)$ complex; see reaction 13. The gold anion formed at $(\text{H}^+)(\text{e}^-)$ defect sites on the MgO surface is predicted to be catalytically active in CO to CO_2 activation. Selected distances are given in Å.¹⁰⁶ Reproduced with permission from ref 106. Copyright 2008 American Chemical Society.

The majority of the surface O_2^- species are adsorbed on Mg_{4c}^{2+} sites, interacting with the proton of a nearby OH^- group.¹⁰³ This explains the original observation reported in 1989 of the existence of an hyperfine interaction of the superoxo ion with a vicinal proton⁸⁰ (see section 3.4). The structural equivalence and uniform spin densities on the two oxygen atoms at this adsorption site have been confirmed using $^{17}\text{O}_2$.¹⁰³ In the second example, molecular nitrogen interacts with $(\text{H}^+)(\text{e}^-)$ centers when physisorbed at temperatures lower than 100 K. In this case reversible formation of an N_2^- surface radical occurs following a net ET from the surface to the π^* orbitals of the adsorbed molecule:¹⁰⁴

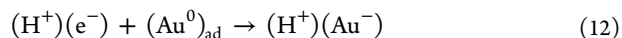


Magnetic and structural equivalence of the two nitrogen atoms was confirmed by EPR, based on analyses of the $^{15}\text{N}_2^-$ and $^{14}\text{N}_2^-$ spectra. The process is completely reversible as at low pressures or higher temperature N_2 is desorbed and the electron is released back to the original surface site. A very small energy barrier separates the bound state (transferred electron) from the physisorbed state (neutral units).^{103a}

At first sight the reactions involving O_2 and N_2 , leading to radical anion formation, are surprising, considering the low or even negative EA of the two molecules, +0.44 eV for O_2 and -2.0 eV for N_2 (calculated). If the driving forces for these reactions were exclusively based on the interplay between ionization energy of the surface center and molecular electron affinity, no ET reaction would occur. However, when electrostatic contributions due to the ionic surface are taken into account, favorable reaction conditions are realized. Once again, only specific sites of the cubic nanocrystals are capable of providing sufficiently strong stabilization energies. This fact exemplifies and highlights once more the importance of low-coordinated surface sites in the chemistry of the MgO surface, and in general of ionic oxides.

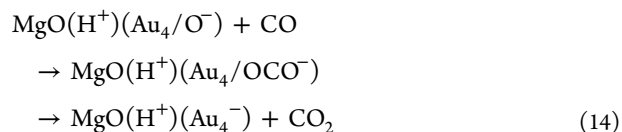
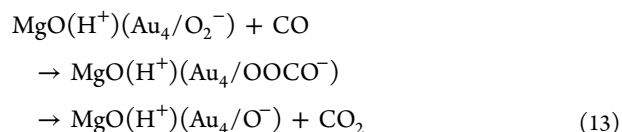
There is another reason why $(\text{H}^+)(\text{e}^-)$ centers substantially modify the reactivity of oxide surfaces. In the past decade evidence has been reported that negatively charged gold clusters supported on an oxide surface may be chemically more active than their neutral counterparts.^{71c,73a,c,74,105} The presence of a negative charge on a small supported Au cluster results in an easier breaking of bonds of adsorbed molecules, O_2 in particular, and in an enhanced catalytic activity. Charging is supposed to occur through the interaction with specific sites of the MgO surface, and oxygen vacancies have been considered for a long time the ideal candidates.^{70b,c,71a,c,73b} As we mentioned previously, Au clusters deposited on oxygen-deficient MgO surfaces are indeed negatively charged.⁷⁴ However, $(\text{H}^+)(\text{e}^-)$ centers can play this role as well.¹⁰⁶ The interaction of an Au atom ($5d^{10}6s^1$ valence configuration) with

a $(\text{H}^+)(\text{e}^-)$ center leads to a spin coupling and a diamagnetic $(\text{H}^+)(\text{Au}^-)$ complex:



The high electron affinity of gold, 2.3 eV, favors the formation of an adsorbed Au^- anion near the surface OH group with a highly exothermic process. Au atoms can thermally diffuse on the surface (the barrier for diffusion of Au on MgO terraces is about 0.2–0.3 eV)^{70e} and become stabilized at $(\text{H}^+)(\text{e}^-)$ defect sites. The ET process is favorable also with gold nanoclusters. Take, for instance, an Au_4 unit. Theoretical calculations have shown that on the $\text{MgO}(001)$ surface this cluster assumes a slightly distorted rhombic structure¹⁰⁷ whereas on a $(\text{H}^+)(\text{e}^-)$ center the Au_4 cluster is nearly linear (Figure 15), as expected for a negatively charged gold cluster (in this model the gold chain bends to adapt to the step morphology; Figure 15).

There is ample evidence that gold cluster anions are active species in promoting CO oxidation to CO_2 ^{105,108} or hydrogen peroxide formation from H_2 and O_2 .¹⁰⁹ Both theoretical and experimental studies on gas-phase or oxide-supported gold cluster anions show that a key step in the reaction is the formation of a superoxo species, O_2^- .¹¹⁰ This is followed by the insertion of the CO molecule with formation of an OOCO intermediate,¹¹¹ separated by a small barrier from the final state consisting in the formation of CO_2 , which desorbs from the cluster. The rupture of the O–O bond and simultaneous formation of the O–CO bond is the rate-determining step, and the formation of O_2^- is a necessary prerequisite. This is the mechanism postulated for low-temperature CO oxidation at gold cluster anions formed at $(\text{H}^+)(\text{e}^-)$ centers.¹⁰⁶ The following reactions occur according to an Eley–Rideal mechanism on supported Au_4^- with low barriers:



With respect to the model of gold clusters activated on F centers, the $\text{MgO}(\text{H}^+)(\text{Au}_n^-)$ model has two important advantages: First, on $(\text{H}^+)(\text{e}^-)$ centers the process is catalytic as it implies the regeneration of the original supported cluster anion at the end of the cycle; see reactions 13 and 14. This is different from gold clusters supported on F centers because the atomic oxygen formed in the course of the reaction most likely

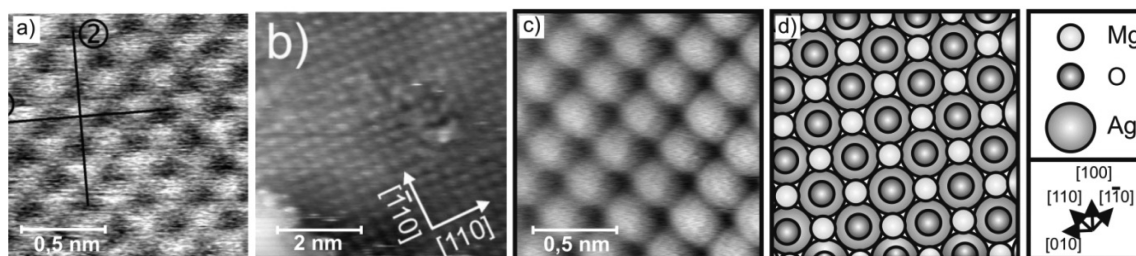


Figure 16. NC-AFM atomically resolved images of MgO(001) surface as reported by Barth and Henry¹¹⁵ for a bulk crystal (a) and by Heyde and co-workers^{119a} for a thin MgO film on Ag(001) (c). The first atomically resolved STM image of a 1 monolayer MgO(001) film on Ag(001) reported by Schintke, Schneider, and co-workers¹¹⁸ is shown in (b) for comparison with a schematic of the MgO(001) surface oriented on a Ag(001) single-crystal surface (d).^{119c} Reproduced with permission from ref 119c. Copyright 2006 American Institute of Physics.

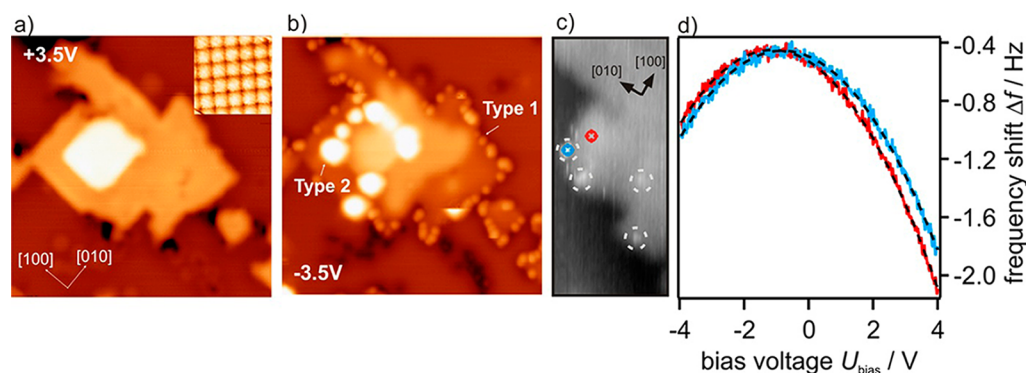


Figure 17. Images and spectra of color centers in a MgO(100) film on Ag(001): (a) topographic image of a set of facets at +3.5 V (inset, atomic resolution)¹²⁰ and (b) color centers located at the step edges of the film imaged at -3.5 V after inducing defects by a high positive voltage sweep before scanning the image; (c) NC-AFM image of a similar surface after the same procedure; (d) frequency shift as a function of bias voltage for a MgO terrace site (red) and after inducing color centers (blue), directly above the defect (blue).^{119a} The difference in maxima represents the change in contact potential.¹²¹ Reproduced with permission from ref 121. Copyright 2009 American Chemical Society.

migrates to the Au/MgO interface and fills the vacancy with elimination of the surface defect.¹¹² When this occurs, the catalytic cycle is broken and the supported cluster is no longer activated. The second advantage is that the $(\text{H}^+)(\text{e}^-)$ defect centers can be easily produced by chemical methods, at variance with F centers that must be specifically generated under more severe conditions.

3.7. Defects at the MgO Surface: Summary

What has been discussed so far are examples of physical and chemical properties and reactivity of simple oxides like MgO accumulated in about 50 years of work. For this purpose, high surface area polycrystalline materials have been synthesized via chemical methods, and their surface properties have been investigated with integrated physical chemistry techniques like optical and vibrational spectroscopies, electron paramagnetic resonance, transmission electron microscopy, etc., often interfaced and complemented by advanced theoretical studies. Some of the phenomena observed, related to ET, have been interpreted as due to surface defects (e.g., the famous F centers), but it is only recently that it has been possible to show that other kinds of electron-rich centers may be involved as well. A deeper understanding calls for surface science approaches and new spectroscopies and microscopies that can provide an atomistic view of the surface composition, the nature of the defects, and their stability and abundance. This is the subject of the following sections.

4. IMAGING SURFACE DEFECTS

4.1. Atomic Force Microscopy and Scanning Tunneling Microscopy

As we have seen in the previous sections, the properties of MgO surfaces are very much determined by the presence of defects. Although ensemble-averaging experiments may allow one to assign the presence of a distribution of species, only local probes will provide access to a characterization and imaging of specific defects or adsorption sites. A prerequisite for the identification of defects is atomic resolution in the scanning probe experiment. On bulk MgO samples, the only available surface-sensitive technique is atomic force microscopy (AFM)¹¹³ in addition to aberration-corrected transmission electron microscopy (TEM),¹¹⁴ whereby the latter is not truly surface-sensitive. The first image with atomic resolution was recorded with an AFM by Barth and Henry¹¹⁵ as shown in Figure 16a. Shluger and collaborators have developed a code to simulate AFM¹¹⁶ images mainly on the basis of AFM images taken on $\text{CaF}_2(111)$ surfaces. In a series of studies they also provided a quantitative modeling of scanning force microscopy on insulating substrates.¹¹⁷

Although those measurements indicated that it is possible to accumulate such data in principle, a breakthrough only came when thin films were studied. Schintke, Schneider, and co-workers¹¹⁸ published the first set of truly atomically resolved scanning tunneling microscopy (STM) images of a MgO(001) film that was only one layer thick (Figure 16b). Atomic resolution for thicker films occurred to be impossible. Later measurements, however, provided indications that it is possible

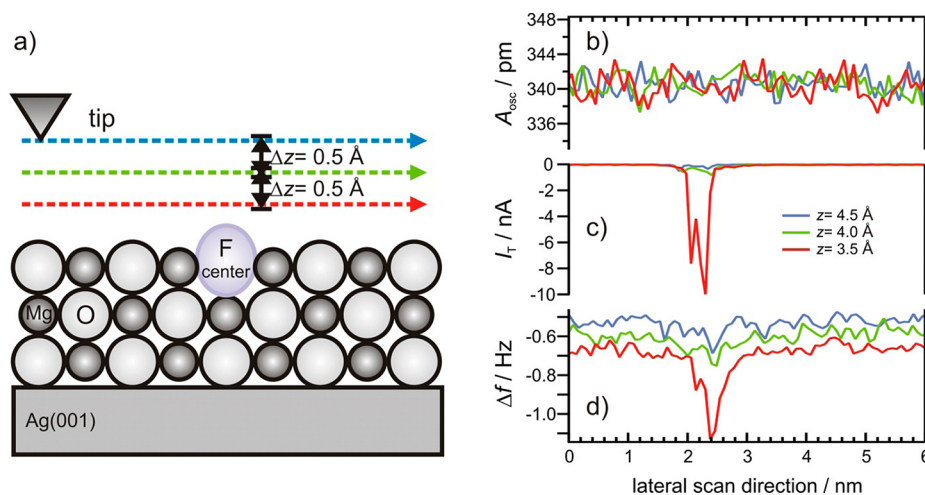


Figure 18. Dependence of experimentally measured quantities on tip–sample distance, in an NC-AFM experiment. Constant-height line-scans across an F^0 defect situated at a step edge. The scan direction is along the step edge. The presented three channels have been measured simultaneously. The colors indicate different tip–sample distances. Note that the displacement of 4.5 Å has been chosen arbitrarily, because absolute values are generally unknown in scanning probe microscopy. (b) The oscillation amplitude is constant during the scan process. This excludes artifacts in frequency shift. (c) The tunneling current and (d) the frequency shift. Data were obtained at a bias voltage of $U_{\text{bias}} = -50$ mV.^{119a} Reproduced with permission from ref 119a. Copyright 2011 Beilstein Institute.

to image even considerably thicker films.¹¹⁹ A noncontact atomic force microscopy (NC-AFM) image of a perfect MgO surface of a MgO film on Ag(001) is shown in Figure 16c. The film is 2 atomic layers thick; however, films with a thickness of 2–8 layers give very similar images. One type of ion is shown as a protrusion whereas the other type of ion is depicted as a depression. This is a typical finding for ionic surfaces imaged by NC-AFM and also predicted by several authors.^{115,116} Because the density of electrons on the MgO surface is the highest above the oxygen atoms,^{44a} the maxima in the NC-AFM image are thought to correspond to the positions of the oxygen atoms. Furthermore, electron paramagnetic resonance (EPR) spectra have shown that the preferred adsorption sites for Au atoms are on top of the oxygen ions on the terrace of the MgO surface.⁷⁴ Assuming that the forces acting on such metal adatoms are comparable to those on the tip apex, one may conclude that a more attractive interaction occurs between the oxygen sites and the tip.

Because the intrinsic defect density of the film is very small, color centers, such as F^0 , F^+ , and F^{2+} , have been generated by operating the scanning probe microscope in the STM (a specialty of the microscope used in Fritz Haber Institute) mode at high currents $I_t = 6$ nA and high voltages $U_{\text{bias}} = 7$ V or higher, thus inducing oxygen vacancy formation. Clean and well-grown MgO areas have been selected to ensure well-defined conditions. The defects are preferentially located at kinks, corners, and steps. This means defect sites with a lower coordination number are preferred, as discussed above. An NC-AFM image of a MgO step edge with point defects is shown in Figure 17c. In the same figure (Figure 17a and b), STM images are shown before and after scanning the surface with higher positive voltages to desorb oxygen to form color centers.¹²⁰ The dependence of the frequency on the bias voltage exhibits a parabolic behavior, and the difference in the parabolas maxima corresponds to relative changes in contact potential (Figure 17d).¹²¹

The high local resolution of the NC-AFM image shown in Figure 17 serves as the starting point for adsorbate–defect interaction studies. The tip, representing the adsorbate, scans

laterally across the defect positions at constant height along the step direction. The simultaneously measured frequency shift Δf and tunneling current I_t provide insight into the local surface potential as well as into the local electronic structure. The corresponding results of such experiments are shown in Figure 18, where the tip was scanned across an F^0 defect. The three stacked graphs show the simultaneously recorded oscillation amplitude Δ_{OSC} , the frequency shift Δf , and the tunneling current I_t . The colored traces in Figure 18b–d indicate constant-height scans at different tip–sample separations as indicated in Figure 18a. At all tip–sample distances, the oscillation amplitude can be considered as constant, which is a prerequisite because the frequency shift scales with the amplitude.¹²²

Because of the exponential dependence of the tunneling current on the tip–sample distance, I_t vanishes at the largest separation and the shift of the resonance frequency is a consequence of the long-range force background arising from electrostatic and van der Waals forces. By decreasing the tip–sample distance by 0.5 Å, the absolute value of the tunneling current and the frequency shift increase at the position of the defect. Despite the decrease of 1.0 Å in tip–sample distance, the average tunneling current on the regular MgO terrace remains below $I_t = -0.05$ nA. This experiment demonstrates the highly attractive interaction of the tip (or adsorbate) with an F^0 center.

It has been debated in literature how color centers are imaged by NC-AFM^{115,123} because a color center represents a geometric hole in the MgO lattice.¹²⁴ The observed attraction of F^0 centers originates from the charge density of the two trapped electrons, which are located in the center of the defect site. Because of Coulomb repulsion, the trapped electrons repel each other and a charge density spills out of the defect site into vacuum (see the discussion above).¹²⁵ This charge density is supposed to interact with the tip, resulting in a strong attraction, as presented in Figure 18. Because the doubly occupied F^0 state is close to the Fermi level of the MgO/Ag(001) system,¹²⁰ the charge density is also responsible for the strong peak in the tunneling current signal. Further insights

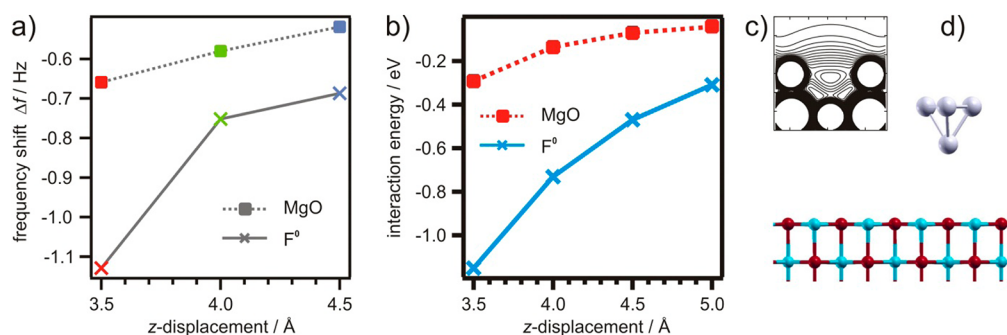


Figure 19. Dependence of frequency shift and interaction energy, respectively, on tip–sample distance. (a) Shift of the resonance frequency of a $\text{Pt}_{0.9}\text{Ir}_{0.1}$ tip on a regular MgO surface (squares) and above an F^0 defect site (crosses). Experimental data are derived from the constant-height measurements shown in Figure 18. The frequency shift is a direct consequence resulting from potential gradients between tip and sample. The integration of the frequency shift is related to the potential energy. (b) Interaction energy of a Pt_4 cluster above the O site of an MgO surface (rectangles) and above an F^0 defect center (crosses) calculated by DFT. (c) The spillover of the electron charge density of an F^0 center calculated by DFT. (d) The Pt_4 cluster above the MgO surface.^{119b,121} Reproduced with permission from ref 119b. Copyright 2010 American Chemical Society.

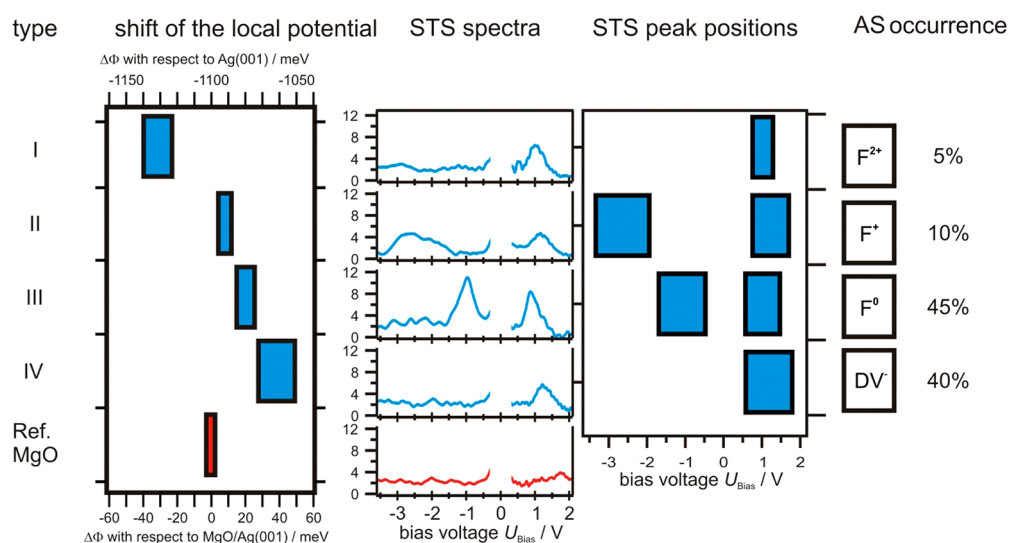


Figure 20. Color centers on MgO. The left labeling assigns numbers to the defect types. The left graph shows the relative shift of the local (effective) contact potential with respect to the MgO surface (bottom abscissa) and with respect to the Ag(001) level (top abscissa). The covered range in the shifts results from measurements with different local resolutions due to different tip structures. The energy level scheme presents the different energy levels of the defect types and their local contact potential shifts. The central graph shows STS spectra of the respective defects. The right graph presents the maxima of the STS data. The covered abscissa range accounts for the statistics of the peak positions. The assignment (AS) of defect types to color centers and negatively charged divacancies (DV^-) according to theory as well as their relative occurrence are given on the right-hand side.¹²¹ Reproduced with permission from ref 121. Copyright 2009 American Chemical Society.

into the interaction of tip and color center are obtained by periodic supercell DFT calculations.^{119b,121,126} The tip–surface interaction energy has been computed as a function of tip–sample distance of the apical Pt_4 cluster (which has been used to model the Pt–Ir tip) with respect to the top layer of the MgO slab (see Figure 19d).

The results of the experimental distance-dependent measurements and the corresponding theoretical results are presented in Figure 19. At the defect site, the tip–sample interaction increases significantly with decreasing distance. For the NC-AFM measurements it is unknown which type of color center, F^0 , F^+ , or F^{2+} , is imaged on the MgO surface. However, Sterrer et al.¹²⁰ measured scanning tunneling spectra (STS) of F^0 and F^+ defects (similar to the ones shown in Figure 20 and discussed later), which were identified through a comparison with theoretical calculations on the energy position of the defect states in the MgO band gap (see also below). To gain further insight into the nature of the color centers, Heyde and

co-workers^{121,124b} performed high-resolution Kelvin probe force microscopy measurements with single-point defect resolution. It has been found that the MgO thin film shifts the Ag(001) work function and thus the contact potential by about 1.1 eV. This MgO level is set as the reference level, and relative shifts are related to it. From measurements of numerous defects, four different types were distinguished by their contact potential, which corresponds to the maximum position of the frequency shift versus bias voltage parabola. The results are shown in Figure 20. On the left-hand side of Figure 20, four types of defects are indicated by numbers, and the MgO reference level is given (red bar). The graph on the left-hand side represents the measured contact potential with respect to the reference MgO level (bottom abscissa) and with respect to the Ag(001) level (top abscissa).

For type I defects, shifts of -50 to -25 meV below the MgO level were observed. These significant shifts can be explained by the presence of positively charged defects with respect to the

surrounding area resulting in a decrease of the local contact potential. The charge density distribution is significantly reduced at the positions of the defects compared with the surrounding MgO lattice. The presence of charges localized at defect sites induces a contact potential shift of the MgO/Ag(001) in analogy to the Helmholtz equation $\Delta\Phi = 4\pi\epsilon\mu\sigma$,¹²⁷ where μ is the dipole moment induced by the localized charge at the site of the defect and the screening charge in the Ag(001) substrate and σ is the surface concentration. However, the full complexity is not covered by the Helmholtz equation, and detailed calculations including the influence of the tip environment are necessary. Defect type II shows a contact potential shift of $\sim+9$ meV. This shift can be assigned to an F^+ . For an F^+ the overall charge is positive, but on a very local scale the single electron has a probability above the surface as derived by DFT calculations.¹²⁵ The charge density spills out of the defect's site and has therefore a probability above the surface. The spill out of the negative charge changes the local dipole moment such that the local contact potential increases compared with the MgO/Ag(001) reference level. The electron charge is symmetrically distributed along the surface normal with its charge maximum located in the center of the defect. Defect type III results in a shift of about +15 to +20 meV above the MgO level. The shift results from two charges present in a defect site and is thus attributed to an F^0 color center. An F^0 is neutral compared to the surrounding MgO lattice, but the two electrons have a large probability density above the surface due to Coulomb repulsion. The charges are as for type II symmetrically distributed and located in the center of the defect; see Figure 19c. Therefore, the charge does not belong to any Mg^{2+} site surrounding the defect. Thus, the oxidation state of the surrounding lattice is not affected by the trapped charges. The spillover of the charges results in a stronger dipole moment compared to defect type II, and the measured shift is about twice as large as that for defect type II.

The strongest positive shift on the relative scale is that of type IV. The strong shift indicates that negative charges are involved. Therefore, this shift might result from divacancies (DVs) or OH groups trapped at low coordinated Mg^{2+} sites. It has been discussed above that OH groups can trap electrons.⁹⁸ However, OH groups and other adsorbates can be excluded because all defects occur only after high voltage and high current scanning and are not present on regular terraces and steps. With the above-mentioned scan parameters, adsorbates would be removed from the scan area. Furthermore, the defects occur only within the high current scan frame and not outside. Favored candidates are, therefore, divacancies formed at step and corner sites because the formation energy at these sites is the lowest. The stability of divacancies and their electron affinities have been confirmed by DFT calculations.⁸⁶ A divacancy is neutral compared with the surrounding MgO, because a complete Mg–O unit is missing. Because of the electron affinity of 0.6–1 eV, electrons can be trapped by the DV from the tunneling junction and the DV becomes negatively charged. The trapped electron of the DV^- is strongly localized at the Mg^{2+} site due to the attractive Coulomb interaction. Because the DV^- is negatively charged with respect to the surrounding MgO area, the additional dipole moment will increase the work function resulting in the largest positive shift on the relative scale. The measured shifts cover a range of values due to different tip structures; however, the reproducibility of two subsequent measurements with the same microscopic tip is within ± 2 meV.

The measurements based on NC-AFM are supported by complementary STS taken simultaneously with the NC-AFM, as well as by the earlier independent STS measurements. For all defects the local density of states (LDOS) has been detected. The tunneling spectra measurements have been performed directly after the local contact potential measurements without moving the tip laterally, i.e., STS and Kelvin probe force microscopy (KPFM) have been performed with the same microscopic tip configuration. The tunneling spectra measured on the defects are compared with MgO spectra on the terrace next to the defect. The MgO reference spectra show no peaks within the voltage regime due to the band gap (compare red lines in Figure 20). The spectra taken on the F^{2+} only show peaks in the unoccupied regime at voltages of $\sim+1$ V above the Fermi level (see Figure 20). The F^+ centers have both occupied and unoccupied electronic states within the band gap. The electronic states are located within the band gap of MgO. The occupied states are quite broadly distributed from -3.5 to -2.0 V below the Fermi level, depending on the defect location on the film.¹²⁰ The empty states are at $\sim+1$ V above the Fermi level. Considering the F^0 color center, the doubly occupied state is higher in energy, approximately -1 V below the Fermi level, whereas the position of the unoccupied state is similar to F^+ centers.

The negatively charged divacancies only show a clear feature in the empty states at about +1 V. The corresponding occupied shallow state is expected to be very close to the Fermi level, i.e., in a region where the experiment cannot clearly detect states. However, F^0 and DV^- are equally frequent and represent $\sim 85\%$ of the total defects. F^+ color centers are much less frequent and represent $\sim 10\%$, and F^{2+} centers represent about 5%. These findings are in good agreement with the high formation energies of F^{2+} centers. By comparing the STS peak positions in Figure 20, it becomes obvious that F^{2+} and DV^- defects are hardly distinguishable by their scanning tunneling spectra but show a significant difference in the local contact potential due to the effect of a locally trapped charge on the surface dipole. This demonstrates the great benefit of NC-AFM and KPFM in combination with STM and STS. All defect types analyzed show a characteristic fingerprint due to different charge states. A comment on theoretical calculations of the energy positions of the levels induced in the band gap is in order. There have been calculations by a number of groups.^{41,51,61a,87a} The results based on density of states calculations are in fair agreement with experiment given the deficiencies of DFT for calculating band gaps.

In Figure 21 we compare the experimental results with calculated ground-state energy levels of F^0 and F^+ centers located at terraces and monatomic steps. Neutral F centers (F^0 , Figure 21c) present a doubly occupied state 3.4 eV (terrace) and 2.8 eV (step) above the top of the O 2p valence band. Above this state, there is a group of three empty close-lying electronic states. They are observed at 1.9–2.0 and 2.0–2.4 eV above the doubly occupied state on the terrace and step, respectively. F^+ centers (Figure 21a) present a singly occupied state 3.0 eV (terrace) and 2.3 eV (step) above the top of the valence band. For the terrace, a set of three empty states due to the charged vacancy is found at 2.6–2.7 eV above the filled level. On the step, the first empty level is at 2.3 eV above the singly occupied state. Two other levels are found at higher energies, 3.1 and 3.2 eV, respectively.

For comparison, the energy levels of type 1 and type 2 defects obtained from the tunneling spectra in this study are

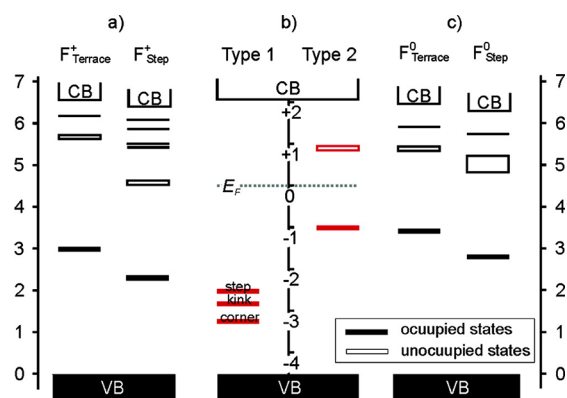


Figure 21. (a) Calculated energy levels of F^+ centers on terrace and step sites. (b) Summary of energy levels of type 1 and type 2 defects from STM experiments. (c) Calculated energy levels of F^0 centers on terrace and step sites.¹²⁰ Reproduced with permission from ref 120. Copyright 2006 American Chemical Society.

plotted in Figure 21b. We find good qualitative agreement between the calculated energy levels of occupied states for singly charged (F^+) and neutral (F^0) color centers and type 1 and type 2 defects, respectively. Unoccupied states are not observed for type 1 defects because of the location of the respective state for step F^+ centers close to the Fermi level of the $MgO(001)/Ag(001)$ system, which prevents the experimental observation of this state. The dependence of the defect state location in the band gap on the coordination number found for F^+ centers (Figure 21a)⁴¹ is also reproduced for type 1 defects, where the occupied state of the corner defect is located closer to the valence band than that of the step site. It should be noted here that the comparison of calculated and experimental data shown in Figure 21 has to remain qualitative, because the presence of the image charge in the $Ag(001)$ substrate, as well as band-bending effects due to the electric field between the scanning tunneling microscope tip and the sample, which is not taken into account in the calculations, might, to some extent, influence the position of the defect states.

4.2. Stability and Diffusion of Oxygen Vacancies

There have been predictions or suggestions that color centers may not be stable in thin films,^{41,125} because they may be discharged into the metallic substrate. It turns out that this is not the case as long as one stays at low temperatures because the migration of color centers is kinetically hindered. However, if temperature is increased, color centers start to migrate, preferentially from the terrace sites to the steps because step color centers are stable. If the number of next layers down will not exceed a certain number (1–2 layers), the color center will discharge. Electron spin resonance (ESR) experiments at increasing temperature have revealed indications¹²⁸ in this direction for the case of F^+ centers. For all other defects there is no experimental evidence available at present. Carrasco et al.⁶⁷ have performed detailed calculations on the energetics and barriers in the migration of neutral oxygen vacancies on $MgO(001)$. Figure 22 summarizes the results.

For a MgO single crystal, diffusion through terrace sites costs 2.69 eV (see also ref 129), whereas diffusion from the surface to the subsequent layers in the film involves larger energy barriers of 3.42, 3.93, and 4.13 eV converging to 4.21 eV for bulk diffusion. Experimentally, a broad range of oxygen vacancy bulk diffusion barrier estimates exists, essentially due to the difficulty

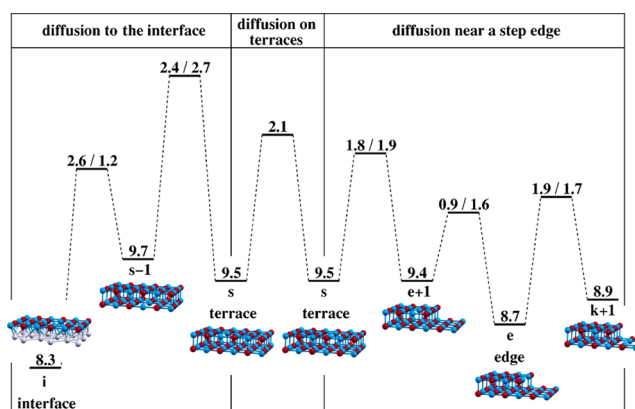


Figure 22. Energy profile (in eV) for the diffusion of oxygen vacancies of MgO (three atomic layers) thin films supported on $Ag(001)$; both formation energy, E^f , and diffusion barriers, E_a , for oxygen vacancies are given. The central panel corresponds to diffusion between surface terrace sites, the left panel shows the profile for diffusion from terrace sites to the inner layers and to the interface, and the right panel stands for the diffusion from terrace sites to the step edge and underlying terrace sites. Structural models representative of the various vacancy configurations considered are given in the insets.⁶⁷ Reproduced with permission from ref 67. Copyright 2006 American Institute of Physics.

to accurately measure this magnitude arising from the fact that, under experimental conditions, F center diffusion competes with other processes, such as interaction with residual gases and the like, also taking place upon sample annealing.¹³⁰ Indeed, experimental values for energy barriers smaller than 3.4 eV have been argued to be related to these competing processes.^{130a} Notice that the predicted surface to subsurface energy barrier for MgO is 3.4 eV, similar to the experimental estimate obtained from the decay of the optical fingerprint corresponding to the surface oxygen vacancy center.^{62i,130a} The difference between the energy barriers described above is large enough to conclude that, whenever oxygen vacancies exist at the surface, transport within the surface will occur at lower temperatures and will always prevail while oxygen vacancies in deeper layers on the material will tend to be more static. The theoretical results indicate that barriers for diffusion from the surface to subsurface layer in the single crystal and on a thin film of three layers differ by less than 0.3 eV, indicating a very fast convergence of this property with the film thickness. Therefore, one can conclude that oxygen vacancy diffusion in a single crystal may be described by calculations on unsupported thin films and will be very similar with noticeable differences for the extreme case of two atomic layer slabs only.

For the metal-supported ultrathin films, the situation is very similar except for the case containing just two atomic layers, which represents a limiting case. In fact, for this extremely thin slab, diffusion to the interface is favored with respect to diffusion through the surface. For the oxygen vacancies at edges, it is interesting to point out that the most favorable process involves diffusion from the terrace to the edge with an energy barrier of 0.87 eV, which is much smaller than the barriers for diffusion either through the terrace or through the bulk. Once the oxygen vacancies reach an edge site they are trapped, because the inverse process implies an energy barrier of 1.57 eV. The rest of the possible competing diffusion processes all have larger energy barriers; the lowest one involves diffusion from the edge to a site of the underlying terrace, but the corresponding energy barrier is 1.88 eV. To

conclude, oxygen vacancy diffusion from the surface to the bulk is a highly unlikely process, but diffusion through the surface terraces is less energetically costly and diffusion to step edge sites involves even smaller energy barriers. Consequently, once the oxygen vacancies reach the step edge sites, they are trapped because further diffusion is hindered by much larger energy barriers. Given the various barriers, in case the temperature is large enough to permit the diffusion through surface sites, the trapping at step edge sites will have a dynamic character in the sense that interdiffusion between step sites is possible. This general picture is fully corroborated by STM and AFM images, where almost exclusively oxygen vacancies are found at the step edges (see Figure 17).

5. NOT ONLY POINT DEFECTS: GRAIN BOUNDARIES

5.1. Strain and Dislocations in MgO Thin Films

The electronic, optical, and chemical properties of wide-gap oxide materials are governed by defects in their crystal structure, e.g., point defects, and step edges, as discussed in the previous sections.¹³¹ Those point defects perturb the local oxide stoichiometry, as individual ions or ion pairs, and give rise to structural relaxations of the surrounding lattice. They also induce discrete electronic states in the band gap that can be filled with electrons. Those extra charges are held in place by the attractive potential produced by the adjacent ions.^{21,41} If those individual species increase their dimensionality, they cluster into larger aggregates. Such situations are often encountered at dislocations. The trapping capacity of those defects depends on their position in the crystal as well as on the modalities of their formation.¹³² The presence of trapped electrons strongly affects the chemical properties of oxide surfaces, which we have briefly addressed and will come back to. The role of extended electron traps in the chemistry of oxide surfaces is not well-studied, and any interrelation between defect density and reactivity proposed in the literature^{71c} was not based on a large base of dependable experimental data, although line defects and grain boundaries are the dominant trapping centers in real oxide supports used in catalysis. The large potential of extended defects to trap electrons has been demonstrated in recent theoretical work by Shluger and co-workers.¹³² Atom-resolved images of ordered defect superstructures with significant electron trapping potential have been reported based on a combined use of advanced electron microscopy, spectroscopy, and first-principles calculations.¹³³ Line defects are also abundant in thin oxide films. In such systems, dense dislocation networks develop spontaneously in order to compensate the lattice mismatch with the substrate.^{40,134} Recently, an STM and EPR study has demonstrated the trapping ability of misfit dislocations formed in MgO/Mo(001) thin films.¹³⁵ Even well-prepared oxide films are able to capture high numbers of electrons, underlining the general importance of this defect type.

Low-energy electron diffraction (LEED) investigations indicate epitaxial growth of the MgO oxide on Mo(001). The MgO(001) plane is parallel to Mo(001), whereas the MgO direction aligns with the Mo[110] direction, as expected from the 5% lattice mismatch between the primitive cells of body-centered cubic (bcc) Mo (3.15 Å) and rock-salt MgO (2.98 Å). A superstructure appears in the low-coverage regime and is attributed to the formation of a Mg–Mo–O interface layer. With increasing thickness, a Moiré structure comprising tilted MgO facets, in agreement with the STM results discussed

below, appears. For a nominal thickness between 5 and 12 ML, similarly also reported for MgO/Ag(001)¹³⁶ and MgO/Fe(001),¹³⁷ the formation of mosaics spanned between a dislocation network that relaxes the strain in the oxide layer is observed.

The evolution of the MgO morphology with increasing film thickness has been analyzed by STM as summarized in Figure 23. After deposition of approximately one layer, the film still

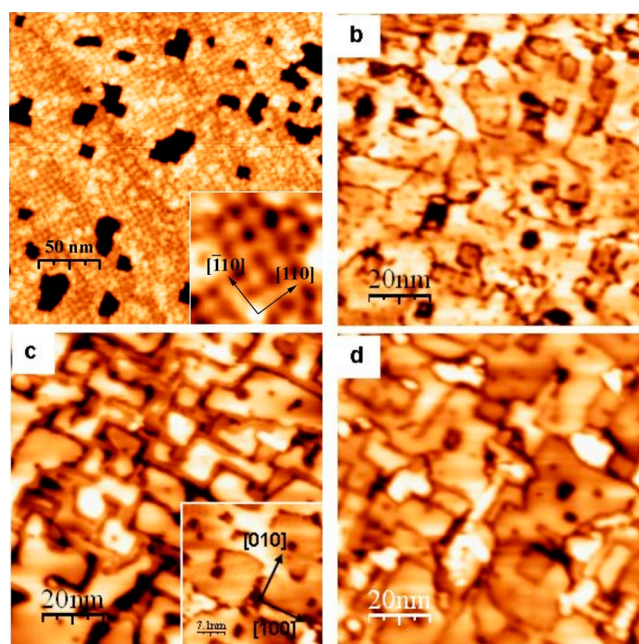


Figure 23. STM images of MgO thin films on Mo(001): (a) $150 \times 150 \text{ nm}^2$ of 0.85 ML MgO ($I = 0.23 \text{ nA}$, $U_{\text{sample}} = +3.4 \text{ V}$). The inset shows a $25 \times 25 \text{ nm}^2$ region of the same sample. (b) 1.75 ML MgO ($I = 0.05 \text{ nA}$, $U_{\text{sample}} = +3 \text{ V}$); (c) 7 ML MgO ($I = 0.14 \text{ nA}$, $U_{\text{sample}} = +3.7 \text{ V}$); (d) 18 ML ($I = 0.15 \text{ nA}$, $U_{\text{sample}} = +12.5 \text{ V}$). Images (b–d) are $100 \times 100 \text{ nm}^2$ in size. The inset in image c shows a screw dislocation, which is frequently observed in 5–10 ML thick MgO films.⁴⁰ Reproduced with permission from ref 40. Copyright 2006 Elsevier.

exhibits large holes, confined by nonpolar [100] and polar [110] oriented edges (Figure 23a). The presence of a significant fraction of polar borders has already been observed for thin MgO films on Ag(001) and ascribed to a stabilization effect of the metal support.¹³⁸ On the oxide surface, a regular square pattern with a mean size of 55 Å becomes visible, which is aligned with the MgO[110] direction. The pattern persists until 5 ML nominal film thickness. The square structure is interpreted as coincidence lattice resulting from the 5% lattice mismatch between MgO and Mo and would be compatible with 18 MgO unit cells overlaying 17 substrate cells along the MgO[110] direction. The calculated size of such Moiré structure amounts to 53.5 Å, in good correspondence to the periodicity of the measured square pattern. The visibility of the Moiré structure is apparently enhanced by an electronic effect, as large topographic contrast is only obtained for sample voltages above 3.5 V.¹³⁹

The surface Moiré pattern fades away for a nominal MgO thickness of 3–5 ML. The dominant structural elements on the surface are now step edges, dislocation lines, and small rectangular holes of 20–50 Å diameter (Figure 23b). Whereas for thinner films, dislocation lines have no preferential

orientation, they begin to align with the MgO[100] direction for thicker ones. In particular cases, the presence of screw dislocations can be recognized, as shown in the inset of Figure 23c. The formation of a dislocation network is a well-known mechanism to reduce stress and strain in thin epitaxial films caused by a lattice mismatch with the support.¹⁴⁰ Above 7 ML film thickness, the oxide gradually flattens and the global roughness decreases, indicating good layer-by-layer growth. For a nominal thickness exceeding 15 ML, STM experiments become increasingly difficult due to the vanishing conductivity of the film and only step edges remain visible at the surface (Figure 23d).

5.2. Electron Trapping at Grain Boundaries

A first indication comes from a deviating electronic structure of the dislocation lines, as deduced from STM images taken in the field-emission regime (Figure 24).¹⁴¹ At high sample bias, the

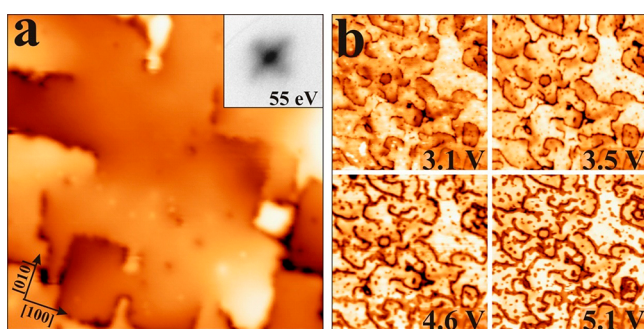


Figure 24. (a) STM image of 12 ML MgO on Mo(001) (3.4 V, 0.05 nA, and $35 \times 35 \text{ nm}^2$). A corresponding LEED pattern is depicted in the inset. (b) High-bias series showing the line defects as deep grooves in the oxide surface 0.05 nA and $100 \times 100 \text{ nm}^2$.¹⁴¹ Reproduced with permission from ref 141. Copyright 2010 American Physical Society.

line defects are imaged with negative apparent height of up to -7 \AA compared to the regular film, although the geometric corrugation deduced from low-bias images is below 2.5 \AA .

The negative contrast indicates a low electron transmissibility of the line defects, forcing the tip to approach the surface in order to maintain a constant current. Electron transport at elevated bias is governed by field emission resonances (FER), which can be considered as vacuum states that develop in the classical part of a tip-sample junction (Figure 25b).¹⁴² Their energy is defined by the condition that multiples of half the free-electron wavelength fit into the triangular region confined by the tunnel barrier and the sample surface. Quantum mechanically, FER are eigenstates E_n in a triangular potential, the bottom and slope of which are given by the sample work function and the tip-electric field F , respectively.¹⁴³

$$E_n = \Phi + ((3\pi\hbar e \cdot F)/2\sqrt{2m})^{2/3} n^{2/3} \quad (15)$$

As field emission resonances carry most of the electron current at high bias, their availability above the MgO surface determines the image contrast in the STM.¹⁴⁴ Apparently, the defect lines offer no or fewer FER than the regular oxide patches and consequently appear dark (see Figure 24b).

According to eq 15, the energy position of the FER is primarily fixed by Φ because the tip-electric field is roughly constant in the feedback-controlled imaging mode employed here. The negative contrast, therefore, suggests a work-function increase around the dislocation lines that moves the FER to higher energies. This assumption is confirmed by dz/dV

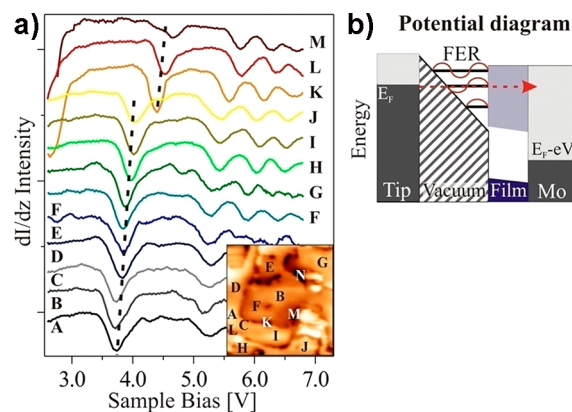


Figure 25. (a) Series of dI/dz spectra measured with enabled feedback loop on terrace (A–J) and defect sites (K–M) of a 12 ML MgO/Mo film. The positions are marked in the inset (0.05 nA and $50 \times 50 \text{ nm}^2$). (b) Visualization of the electron transport through an STM junction in the field emission regime.¹⁴¹ Reproduced with permission from ref 141. Copyright 2010 American Physical Society.

spectroscopy, where the FER show up as minima due to the sudden tip retraction when the next transport channel becomes accessible (see Figure 25a). On defect-free oxide patches (positions A–J), the first and second FER are reached around 3.7 and 5.4 V, respectively, with the exact value depending on the terrace size. Above the line defects, the first and second resonances are systematically upshifted to 4.4 and 6.0 V (positions K–M), corroborating the local increase in the work function.

Complementary information is obtained from STM light emission spectra taken on the MgO/Mo films (see Figure 26a). It is known that¹⁴⁵ the optical response is governed by radiative electron transitions from higher to lower FER states.

The dominant peak at 1.75 eV (700 nm) corresponds to a decay from the second to the first FER state while a weak shoulder at 2.5 eV (500 nm) involves the third and first FER states. The high cross section of the emission is owed to the long residence time of electrons in the FER being caused by the penetration barrier imposed on the system by the oxide film. Similar to the resonance states, the photon response is sensitive to the oxide work function. On regular MgO terraces, the emission becomes detectable between 4.8 and 5.5 V excitation bias, which covers the energy window of the second FER in this region (see Figure 26a). In contrast, no emission is observed below 5.8 V for the line defects, in agreement with an upshift of the FER. The energy of the emission peak remains constant in both cases, reflecting the rigid shift of the FER with Φ . Whereas on regular patches the intensity maximum is reached below 5.5 V (positions A–E), it shifts above 5.5 V on the line defects (positions F and G). This bias difference can be exploited to display the work-function distribution in the MgO film by mapping the integral photon yield as a function of sample bias (see Figure 26c). In photon maps taken at 5.1 V, only the flat MgO terraces with low Φ emit light and the defects remain dark. The contrast reverses at 6.0 V, as the optical channel opens in the defect regions. Both electronic and optical spectroscopy conclusively reveal a work-function increase of 0.7 eV along MgO/Mo line defects with respect to the regular film.

To explain this observation, one needs to consider that oxide films in general modify the work function of a metal support. According to DFT calculations and Kelvin probe studies, the MgO film reduces Φ by $\sim 1.5 \text{ eV}$.^{124b,146} The effect is caused by

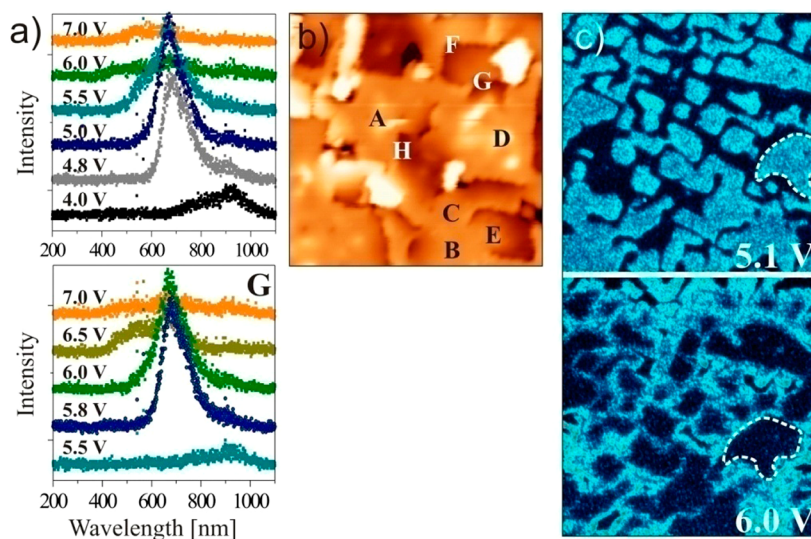


Figure 26. (a) Light-emission spectra taken as a function of excitation bias on a regular terrace site (B) and a line defect (G) (current = 1 nA). The spectral positions are shown in the STM image in (b) ($50 \times 50 \text{ nm}^2$). (c) Photon maps (1 nA and $75 \times 75 \text{ nm}^2$) taken at the bias position of the second FER on MgO terraces (top) and defect lines (bottom). The contrast reversal between both images reflects work-function modulations in the film.¹⁴¹ Reproduced with permission from ref 141. Copyright 2010 American Physical Society.

an electron transfer out of the film that creates a positive interface dipole and the suppressed electron spillover at the metal surface. Surface defects may alter this trend due to their influence on the local charge distribution. While electron-poor defects, such as F^{2+} centers or cationic edge and corner sites, produce positive surface dipoles that lower Φ , electron-rich defects increase the charge density at the surface and hence the work function. The higher value measured along MgO line defects is therefore compatible with a charge accumulation and indicates electron trapping in the dislocation lines. This conclusion is in agreement with DFT calculations that identified electrostatic pockets in the Madelung potential along an MgO grain boundary that can be filled with electrons.^{132,147} The associated gap states are localized close to the conduction-band onset. Because of the high energy of the electrostatic traps, electron trapping will be restricted to oxide films that are sufficiently thick to inhibit electron tunneling into the metal support. Alternatively, a “chemical trapping” of electrons is conceivable. In this case, the excess electrons are captured in the form of reduced Mg^0/Mg^+ species or extra O^{2-} ions and come along with a nonstoichiometric oxide composition along the line defect. As chemical traps are often filled via electron transfer from the metal support, they become active primarily in thin films.

The observed work function increase along the MgO line defects is partly attributed to chemically trapped electrons.¹⁴⁸ As the expected deviation from the ideal MgO composition lies only in the percent range, it could not be detected with conventional X-ray photoelectron spectroscopy.^{40,134d} In thick MgO films, on the other hand, also the electrostatic traps can be filled, as demonstrated by EPR measurements. After saturating the surface with atomic hydrogen produced by cracking 30 L H_2 on a hot filament, a strong bulklike EPR line develops at $g = 2.003$ (see Figure 27a). Its position near the free-electron g value and the lack of the hyperfine signature of hydrogen indicates that the electrons are abstracted from the H atoms as they enter the line defects. The electrons remain, however, close to the protons, as the EPR line narrows in a characteristic manner upon exchanging H_2 with D_2 . The EPR

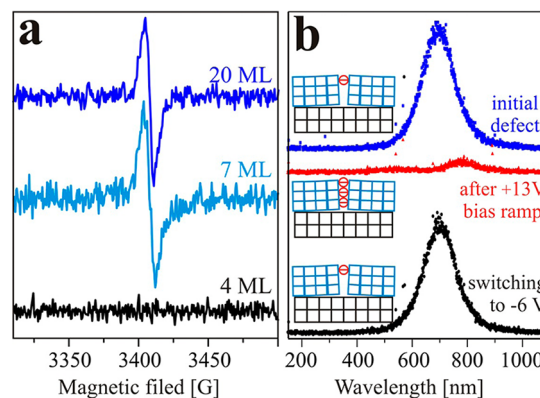


Figure 27. (a) EPR spectra of differently thick MgO/Mo(001) films after exposure to a saturation coverage of H atoms. The bulk signal at $g = 2.003$ indicates electron trapping in the line defects of thicker films. (b) Light-emission spectra taken on a pristine line defect top after a bias ramp to +13 V center and after reversing the polarity bottom. All spectra are acquired at +6 V sample bias and 1 nA current. The suppressed emission after the ramp is ascribed to electron trapping in the line defect, being reversed at negative bias (see insets).¹⁴¹ Reproduced with permission from ref 141. Copyright 2010 American Physical Society.

signal is not observed in films below 7 ML thickness, most likely because the electrons are drained to Mo support.

It also vanishes when annealing a thick film to 500 K, which indicates thermal activation of the trapped electrons into the MgO conduction band (desorption of H_2 would be an additional explanation for the quenching of the EPR signal at 500 K). From this temperature threshold, the energy gap between the trap states and the band onset is estimated to be around 1.0 eV when assuming an attempt frequency of $1 \times 10^{13} \text{ s}^{-1}$ for the Arrhenius-type behavior. Such activation energy is in line with the DFT results obtained for MgO grain boundaries.¹³² The intensity of the EPR line is compatible with 5×10^{13} unpaired electrons, which provides only a lower bound for the total number of trapped charges. However, already this value is a factor of 10 larger than the highest

number of electrons that can be stored in paramagnetic point defects.^{77,149} Distributing the trapped charges along the circumference of all dislocation lines, as estimated from the STM images, yields a density of 3–5 electrons per nm line defect. It should be noted that at such high carrier densities electron–electron interactions start to affect the EPR spectra, giving rise to a broadening of the resonance.

Filling of the electrostatic traps in thicker films was also achieved locally with the STM. For this purpose, voltage ramps with enabled feedback loops were applied to the STM junction. The effect of electron trapping was then monitored by reversible changes in the optical response. As discussed above, a pristine defect emits photons at 6.0 V excitation bias. After ramping the bias to +13 V and returning to the initial situation, the photon signal vanishes (see Figure 27b). It recovers only after a quick reversal of the bias polarity. Apparently, electrons from the MgO valence band are excited into the shallow trap states at high bias, although those states are not directly accessible for tunneling due to their negligible overlap with the Mo wave functions. The trapped charges trigger a work-function increase that renders the second FER unavailable for optical transitions at 6.0 V excitation bias. The electrons are only stabilized at positive bias but leave the trap states at negative polarity most likely via tunneling to the tip. The subsequent discharging of the gap states restores the initial photon signal. A comparable hysteresis in the optical response is not observed on the oxide terraces, reflecting the crucial role of the line defects in the trapping phenomenon.

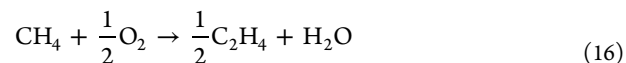
With those investigations it is obvious that defects of higher dimensionality than point defects are very efficient electron traps. Those trapped electrons may be transferred from the interface into the trap and vice versa, as seen above. Voltage pulses from a tunneling tip may be used to do so. In this sense, the trapped electrons are a consequence of the existence of the oxide metal interface and are not expected to be present in an insulating oxide powder. By evaporating a metal onto oxide films exhibiting those properties, one expects that metals such as Au, characterized by high electronegativity, may nucleate on those electrons containing grain boundaries. This has, indeed, been observed,¹³⁵ and exposure of those charged Au clusters to carbon monoxide leads to FTIR spectra, briefly addressed in earlier parts of this review (see Figure 9), fully consistent in frequency shift and signal intensity with expectations from other studies. Therefore, not the few point defects existing on the oxide surface but rather the grain boundaries, artificially filled with electrons, from the oxide metal interface represent the nucleation sites for metals. If one wants to study the influence of the point defects relevant for heterogeneous catalysis, one has to resort to systems and preparation conditions that avoid formation of those extended defects.

6. NEW FRONTIERS: DEFECTS ENGINEERING VIA DOPING OF OXIDE FILMS

6.1. Li-Doped MgO in Methane Coupling Reactions

We had seen in earlier sections of this review that charge transfer to and from point defects as well as defects of higher dimensionality, such as grain boundaries within pure MgO, may have pronounced influence on the properties of the material itself and in particular on material interacting with MgO. Another way of modifying the properties of an oxide, including MgO, that has been used early on in catalysis has been to dope the material with different metal ions. Probably the best known

case, which has already been mentioned in the Introduction to this review, is the use of Li-doped MgO as a catalyst for oxidative methane coupling to ethene. The transformation of abundant stable hydrocarbons into useful chemicals is a major task of today's basic research in catalysis.¹⁵⁰ In particular, methane activation has recently received considerable attention.¹⁵¹ Oxidative coupling of methane (OCM) according to



with $\Delta_r H = 139 \text{ kJ mol}^{-1}$ at 800 °C has been a central focus of research. However, the underlying reaction mechanism is still not understood. For the reference catalyst, lithium-doped magnesium oxide, there is a heavily debated proposal for a mechanism that was put forward by Jack Lunsford several years ago.¹⁵² The key step is hydrogen abstraction by O^- species, being created by Li doping and subsequent formation of Li^+O^- ion pairs. Lunsford and co-workers provided circumstantial evidence from a number of loosely connected experiments for a correlation between Li incorporation and the chemical activity of the doped oxide.¹⁵³ CH_3' radicals were collected behind the Li/MgO catalyst bed and identified by ESR spectroscopy. In separate experiments, the Li/MgO material was annealed to 700 °C in air or pure O_2 instead of the OCM gas mixture and quenched afterward at 77 K. After this treatment, the material showed an ESR signal at $g = 2.054$, assigned to Li^+O^- centers, although no evidence for the spatial proximity of the paramagnetic defect and the Li^+ ion could be provided. From these experiments, it was concluded that CH_4 molecules dissociate homolytically on the Li^+O^- centers into Li^+OH^- and CH_3' radicals. The latter would desorb into the gas phase, where they would couple in a stoichiometric reaction, giving C_2H_6 as the primary C_2 product ($\text{CH}_3' + \text{CH}_3' \rightarrow \text{C}_2\text{H}_6$).

Given the lack of direct interconnection between the various pieces of evidence, a research effort has been set up in Berlin through collaboration between theory and experiment to study the surface properties of Li-doped MgO, in order to revisit the proposed reaction mechanism.¹⁵⁴ For this purpose, STM and TEM microscopies in combination with optical and EPR spectroscopies were used to study two model systems for Li-doped MgO. The first was a MgO thin film grown on Mo(001) with Li being incorporated during film preparation. The second was a Li/MgO powder catalyst that was fabricated by gel-combustion synthesis from $\text{Mg}(\text{NO}_3)_2/\text{LiNO}_3$ /glycerol gels. In both cases, the Li has left the sample at reaction temperatures, but it has induced a considerable roughening of the MgO surface at elevated temperatures due to segregation of dopants to the sample surface and defect formation.¹⁵⁵ The thermodynamics of the underlying processes was revealed from ab initio calculations performed in addition. The surface modification of Li-doped MgO, with respect to the bare oxide, is considered an essential, yet disregarded, precondition for the catalytic activity of the Li/MgO system instead of the Li^+O^- ion pair formation. It seems that the nature of the long-discussed Li-doped MgO materials for methane activation needs further experimental and theoretical investigation to clarify the role of Li–O pairs and the proposed mechanisms involved.

6.2. Transition Metal Doping of CaO Films

Although the case of the Li/MgO system has taken a different route, doping is a versatile, yet little examined, approach to tailor the physical and chemical properties of oxide thin films. By means of STM, it has been demonstrated how tiny amounts

of Mo embedded in a CaO matrix change the growth behavior of deposited gold. Whereas 3D deposits are formed on the pristine oxide surface, strictly 2D growth prevails on the doped material. The crossover in particle shape from 3D to 2D behavior is driven by a charge-transfer process from the Mo dopants into the Au islands, as elucidated with DFT calculations. Optimizing the structural and electronic properties of supported metal catalysts to augment their conversion and selectivity is a goal of catalysis research. Special emphasis was placed on controlling the properties of the metal centers on the catalyst surface, that is, their size, shape, crystallinity, and charge state. In gold catalysis, for example, small raftlike deposits with amorphous structure and nonzero charge state were found to be more active than their bulklike and neutral counterparts.¹⁵⁶ There are different approaches to manipulate the properties of metal deposits. Whereas their size and density can be tuned by introducing anchoring sites into the oxide surface, for example, defects^{156c} or hydroxyl groups,^{96a} their charge state is controlled by adjusting the metal–support interactions.¹⁵⁷ Oxygen vacancies or structural electron traps, for example, were found to initiate a charge transfer into the admetal (see previous sections). On ultrathin oxide films, even spontaneous charging takes place as electrons tunnel from the substrate into the metal deposits (see also section 7).¹⁵⁸ Oxide doping opens new, versatile routes to tune particle–support interactions.^{84c,159} Whereas “overvalent” dopants produce excess electrons in the host oxide that can be transferred into suitable adsorbates, “undervalent” impurities promote the formation of holes in the oxide electronic structure that might be filled with electrons from the metal deposits. Such a charge transfer has direct consequences on the equilibrium shape of the adparticles, as it enhances the metal oxide adhesion as well as the Coulomb forces within the confined metallic systems.^{158b,160} The presence of dopants also alters the formation energy of oxide defects that may act as nucleation centers and hence stabilize the dispersion of the active species.¹⁶¹

To study dopant effects, a few prerequisites have to be fulfilled. The substrate should grow in high-quality films, as grain boundaries may represent trapping centers for dopants, prohibiting a uniform distribution within the oxide. It turns out that MgO is not so well-suited as CaO as a model system to study the effects systematically. The oxide is isostructural to MgO and has comparable properties as far as the melting temperature, the size of the band gap, or the associated optical properties are concerned.¹⁶² In contrast, both oxides largely differ in their chemical behavior, as CaO is more basic than MgO.¹⁶³ This difference can be traced back to the increased lattice parameter, and hence the lower Madelung potential of CaO, which leads to an upshift of the valence band with respect to the vacuum energy and renders the oxide a good electron donor.^{17,26} CaO is also characterized by a higher state density at the surface that originates from the larger spatial expansion of the Ca 4s with respect to the Mg 3s orbital. The more delocalized electronic structure makes it easier for adsorbates to interact with the surface, which further promotes the chemical reactivity of CaO. Such differences in the chemical behavior, despite a comparable lattice structure, render a detailed comparison of CaO and MgO interesting from a fundamental but also an applied point of view.

Whereas a tremendous amount of work, both experimental and theoretical, has been devoted to MgO,²⁵ the number of CaO studies is surprisingly small. One reason is related to the difficulty to prepare high-quality CaO samples, such as single

crystals, powders, and thin films.^{162a,b,163} STM, LEED, and Auger measurements revealed a complex growth behavior of CaO on a Mo(001) support, being triggered by the relatively large lattice mismatch between both systems. Some results are summarized in Figure 28.¹⁶⁴ In the limit of ultrathin films,

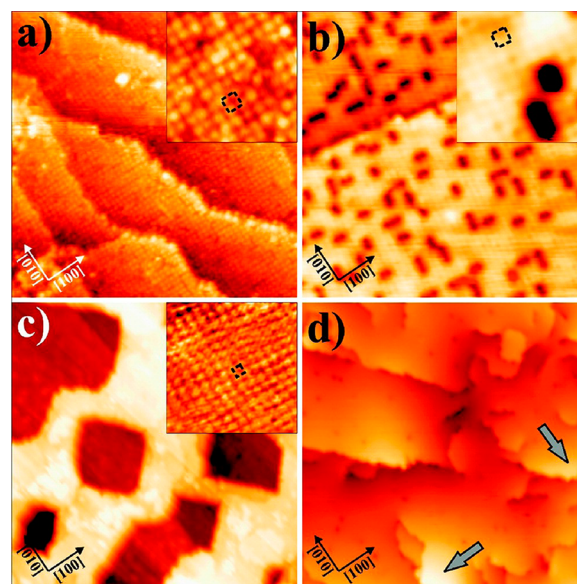


Figure 28. STM topographic images of CaO films as a function of thickness: (a) 3 ML (−1.2 V, $25 \times 25 \text{ nm}^2$), (b) 5 ML (2.2 V, $30 \times 30 \text{ nm}^2$), (c) 10 ML (4.5 V, $100 \times 100 \text{ nm}^2$), and (d) 16 ML (4.5 V, $100 \times 100 \text{ nm}^2$). The insets show atomically resolved data of selected surface regions ($5 \times 5 \text{ nm}^2$) with the (2×2) and (1×1) unit cells being marked with dashed squares in (a, b) and (c), respectively. The arrows in (d) denote the direction of surface tilt on the faceted CaO films.^{164a} Reproduced with permission from ref 164a. Copyright 2011 American Chemical Society.

mixed-oxide layers develop upon thermal treatment, whereby Mo from the substrate diffuses into the CaO rock-salt structure. Because of a reduction of the Mo–O versus Ca–O bond length, the mixed oxide has a smaller lattice parameter and grows in (2×2) registry with the Mo support. The formation of a mixed oxide stops at a critical thickness of 4–5 ML, as the Mo diffusion into the film breaks down. The reappearing lattice mismatch drives the CaO into a three-dimensional growth regime that is compatible with the Stranski–Krastanov mode. At even higher exposure, the 3D oxide islands merge into a flat and defect-poor film, characterized by structural and electronic parameters that are similar to the ones of bulk CaO.

The CaO/Mo(001) films display several fascinating properties in the various growth stages. At low thickness, the Mo impurities inside the CaO matrix give rise to a number of unusual electronic, optical, and magnetic properties that are intrinsically connected to the Mo d levels located in the oxide band gap.¹⁶⁵ The Mo dopants will also alter the adsorption and hence the chemical characteristic of ultrathin oxide films. By comparing the CaO and MgO systems, new insight into the relationship between lattice parameter, electronic properties, and chemical reactivity of isostructural oxide materials may be achieved. One important question to be answered when dealing with doped materials is the one about the lattice position of the dopant. This may be often difficult to know but may be investigated to a certain extent either by high-resolution TEM or optical spectroscopy. Local optical spectroscopy via cathode

luminescence¹⁶⁶ with the STM turns out to be helpful. Cr as well as Mo dopants in MgO and CaO have been studied. The impurities induce a number of narrow emission peaks between 1.7 and 1.8 eV. The STM allows for detecting those dipole forbidden, and hence weak, optical transitions with high spatial resolution, even on a thin oxide film. This allows one to conclude that, in the case of Cr/MgO, the Cr ions substitute for the Mg ions. Similar conclusions may be drawn for Mo/CaO.

The influence of Mo dopants on the growth of Au particles on CaO(001) films has been investigated by STM and DFT.¹⁶⁷ The doping is realized by adding 2 at % of Mo to the Ca/O vapor that is used for growing oxide films of 60 ML thickness.^{164a,167} The topmost layers are always prepared without dopants to suppress Mo segregation to the surface. STM images of molybdenum-doped CaO films (CaO_{Mo}) display atomically flat and defect-poor surfaces, covered with oxide terraces of 20 nm diameter, independent of the doping level (Figure 29). The predominant defects are dislocation lines

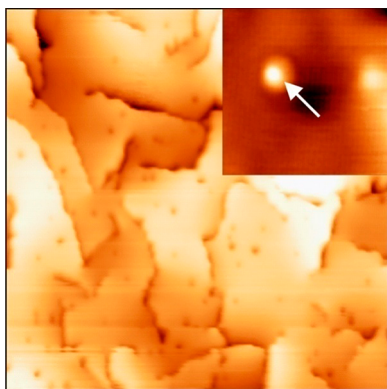


Figure 29. STM image of a doped CaO film (100 × 100 nm²). Inset: single Mo impurity, as observed in a film without capping layer (5 × 5 nm²).¹⁶⁷ Reproduced with permission from ref 167. Copyright 2011 Wiley-VCH.

that originate from the coalescence of neighboring oxide islands and are involved in compensating the substrate-induced lattice strain.^{164a} For doped films with more than 10 capping layers, no additional defects are revealed on the surface. Apparently, the caps are sufficiently thick to inhibit Mo segregation even during high-temperature treatment (up to 1000 K). When using thinner caps, atom-sized protrusions can be detected in the STM, which are assigned to individual Mo species (Figure 29, inset).

Deposition of 0.7 ML Au at 300 K leads to the formation of metal particles. On pristine films, the deposits preferentially nucleate along the CaO dislocation lines and adopt pronounced 3D shapes (Figure 30 a) with a height-to-diameter ratio of 0.35 ± 0.10 (Figure 30c and d). The observed Volmer–Weber growth is characteristic for metals on wide-band gap materials and reflects the small adhesion between adlayer and inert oxide support.¹⁶⁸ In contrast, on the doped films, randomly distributed Au islands of monolayer height and aspect ratios of 0.07 ± 0.02 develop (Figure 30b–d). These islands have hexagonal shapes, indicating growth along Au[111], and display a characteristic stripe pattern on their surface that is assigned to a Moiré structure formed between the square CaO and the hexagonal Au(111) lattice. The patterns occur with different orientations, indicating a rather loose Au–CaO interfacial registry. However, the mere appearance of monolayer islands

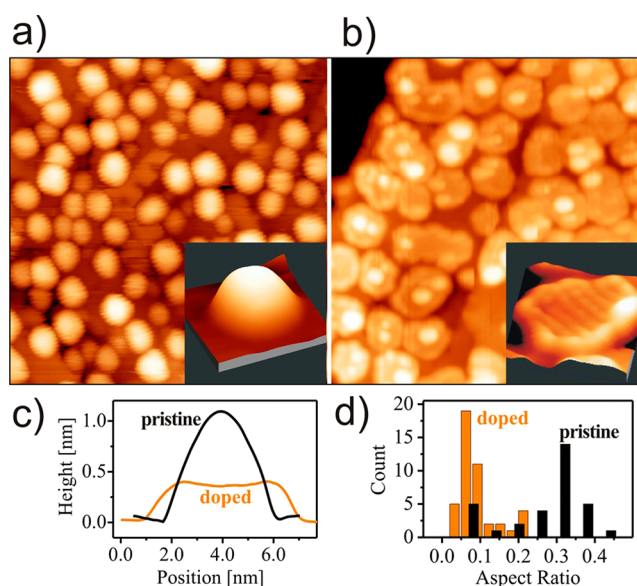


Figure 30. STM images of 0.7 ML Au on (a) pristine and (b) doped CaO films (50 × 50 nm²). The insets display close-ups of two characteristic particles (10 × 10 nm²) with the corresponding height profiles plotted in (c). (d) Histogram of particle aspect ratios on doped and pristine films.¹⁶⁷ Reproduced with permission from ref 167. Copyright 2011 Wiley-VCH.

suggests that the Mo impurities have a considerable impact on the Au–CaO adhesion. DFT calculations on a five-layer CaO(001) slab with one Mo atom substituting one Ca²⁺ ion (2% Mo content) reveal that the binding strength nearly triples in the presence of a Mo species, even if the dopant is located well below the surface. (Without dopants, the Au adsorbs with 1.35 eV on top of a surface oxygen ion.) Clearly, the Au–Mo interaction is preserved over large distances and independent of direct orbital overlap.

Furthermore, the preference for binding to a surface oxygen atom is lost and cationic, anionic, and hollow sites become equally preferred sites for Au adsorption on the doped CaO films. For charge-neutrality reasons, the substituting Mo should adopt the 2+ charge state of a cation in a rock-salt structure, which implies the Mo center must donate its 5s electrons to the neighboring ions, but retains the four electrons in the Mo 4d shell. This scenario is confirmed with calculations for a single Mo in a bulk CaO environment, which finds the low-spin ($t_{2g})^4(e_g)^0$ configuration as ground state and the high-spin ($t_{2g})^3(e_g)^1$ state at 0.5 eV higher energy.¹⁶⁷ STM conductance spectra taken on 8 ML thick doped films confirm the existence of localized states in the gap region. Their assignment to specific Mo 4d levels is hampered by the proximity of the metal substrate that is neglected in the calculations.

The calculations suggest that the Mo²⁺ charge state is unstable against electron transfer, either into CaO defect states (e.g., Ca vacancies)^{132,141} or into adspecies with acceptor character. A charge transfer into the Au deposits is fully compatible with both the theoretical and experimental results. On pristine CaO, the Au atoms are neutral, as deduced from their half-filled 6s level, and bind to the surface mainly through O 2p–Au 5d hybridization. Upon doping, the Au 6s orbital shifts below the Fermi level and becomes doubly occupied, through a charge transfer from the Mo 4d state, leading to an increased Bader charge and a vanishing magnetization of the bound gold atoms. Concomitantly, the oxidation of the Mo

dopant is detected, the occupancy of the Mo 4d levels changes to $(t_{2g})^3(e_g)^0$, and the Mo charge state rises to 3+. The electron transfer enables strong electrostatic interactions between the Au and the CaO surface, boosted by a polaronic lattice distortion.^{158a,169} Even if the Mo dopant is in the 3+ oxidation state, charge transfer to adsorbed gold is still possible via formation of Mo^{4+} .¹⁷⁰ Thanks to this charge-mediated bond reinforcement triggered by the Mo, the gold tends to maximize its contact area with the CaO and forms 2D islands.

As stated previously, whereas “overvalent” dopants produce excess electrons in the host oxide that may be transferred to Au particles, “undervalent” impurities should promote the formation of holes in the oxide electronic structure that might be filled with electrons from the overvalent dopant, thus attenuating or suppressing the ability of electron transfer to adsorbates. This is, indeed, observed as shown in Figure 31a–

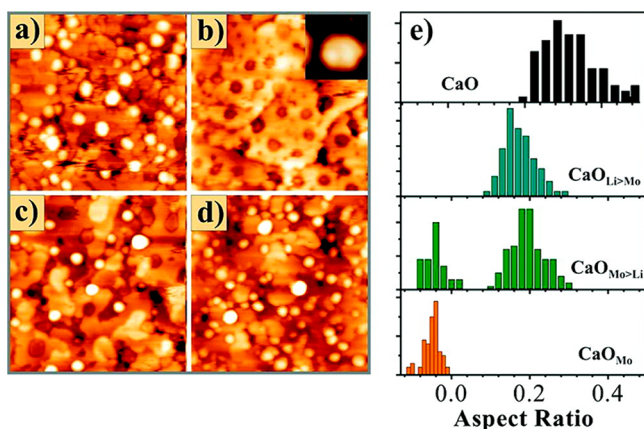


Figure 31. STM images of 0.5 ML Au deposited onto (a) pristine CaO, (b) doped with 4% Mo, (c) doped with 4% Mo + 2% Li, and (d) doped with 4% Mo + 8% Li (6.0 V , $50 \times 50\text{ nm}^2$). Note that monolayer Au islands in (b) and (c) appear as depressions at high sample bias. The typical contrast is only revealed in low-bias images (3.0 V , see inset of b), which are however difficult to obtain on the insulating oxide film. (e) Histogram of aspect ratios for Au particles grown on the differently doped CaO films.¹⁷¹ Reproduced with permission from ref 171. Copyright 2012 American Chemical Society.

d.¹⁷¹ Adding small amounts of Li to the Mo-doped CaO reinstalls the initial 3D growth regime of CaO-supported Au particles. We assign this morphology crossover to charge transfer processes between the dopants and the admetal. Whereas Mo acts as electron donor and provides excess charges to be transferred into the gold, Li creates electron traps in the oxide lattice that interrupt the charge flow toward the metal. The different Au charge states in the presence of the dopants

are derived from different growth morphologies (Figure 31c), with anionic gold favoring a 2D mode due to an enhanced interface adhesion.

7. MgO ULTRATHIN FILMS: ELECTRON TRANSFER VIA TUNNELING MECHANISMS

7.1. Cabrera–Mott Theory of Oxidation of Metals

So far we have seen that charge transfer at oxide surfaces takes place when specific electronic states are available on the adsorbate and/or on some special sites like point defects, morphological irregularities, low-coordinated atoms, trapped electrons, and other impurities present on the oxide surface. In this respect, mastering and engineering charge transfer processes at oxide surfaces requires a control down to the atomic scale of the individual donor or acceptor centers.

In this section we describe another phenomenon, which may occur spontaneously when molecules, clusters, or metal nanoparticles are deposited on the surface of an ultrathin film even in the absence of defects. This is the direct electron transfer from the metal support to the adsorbate (or vice versa) by electron tunneling through the thin oxide dielectric layer. This notion is not new as it has been proposed a long time ago to rationalize the early stages of oxidation of metals via formation of a thin oxide layer. In 1949 Cabrera and Mott¹⁷² suggested that the oxidation process starts by adsorption of oxygen molecules on top of the metal surface, followed by formation of atomic oxygen species. The subsequent steps involve therefore adsorption and activation of molecular oxygen on the surface of the oxide ultrathin film grown on the metal. This can occur via electron tunneling from the metal through the oxide layer to the adsorbed O_2 molecules, which transform into superoxo O_2^- ions: the empty states of O_2 fall below the Fermi level of the metal, generating a potential difference that induces the electron tunneling (Figure 32). The superoxo ions then split to form oxide anions that either diffuse toward the metal through the growing oxide or force metal ions to migrate through the oxide to the oxide–oxygen interface, and continue the oxidation of the metal until the film is too thick to allow electron tunneling. At this point oxygen activation is no longer possible, and the oxidation process stops. Native oxide passive layers of 1–5 nm thickness grown on a metal surface can provide indeed an efficient barrier toward corrosion.¹⁷³ This picture well-illustrates the possibility to exploit ultrathin oxide films to induce charging of adsorbed species. In fact, recent results show that the very same process can occur for any kind of insulating layer on a metal or semiconductor substrate, provided that the film thickness is below some characteristic length scale of the material, as the mean-free path of electrons.^{144,156e,174}

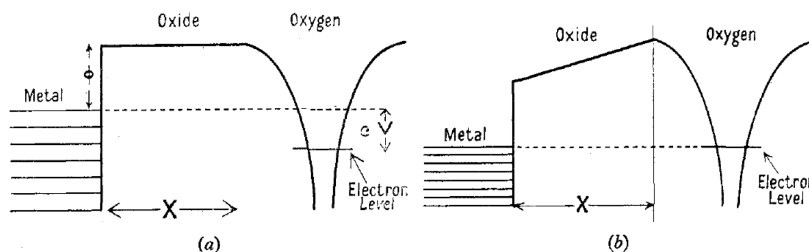


Figure 32. Schematic diagram in the original paper by Cabrera and Mott on the theory of oxidation of metals showing the electronic levels in the metal, oxide, and adsorbed oxygen molecule before electrons have passed through the oxide (left) and when equilibrium is set up (right).¹⁷² Reproduced with permission from ref 172. Copyright 1948 Institute of Physics.

7.2. Spontaneous Charging of Adsorbates on MgO Ultrathin Films

DFT studies have shown that Pd and Au atoms adsorbed on the MgO(001) surface or on MgO/Mo(001) ultrathin films exhibit a completely different behavior.^{158a} Although the properties of adsorbed Pd atoms (binding energy, adsorption site, atomic charge, etc.) are practically the same on bulk MgO or on a 2 ML MgO/Mo(001) film, a completely different bonding mode occurs for Au atoms interacting with the two supports: whereas on the bare MgO(001) surface Au clearly prefers to adsorb on top of the oxide anions, on MgO/Mo(001) Au prefers to bind to Mg cations or in the 4-fold hollow sites.^{158a,175} The change in adsorption site is related to a large change in bond strength and, most important, in a completely different chemical nature of the adsorbate. Accurate EPR experiments in UHV⁷⁹ as well as DFT calculations^{70e} have shown unambiguously that Au atoms deposited on the (001) terraces of MgO are essentially “neutral” and keep their atomic character. In fact, the 6s valence orbital of the Au atom is singly occupied, as in gas phase, resulting in a typical EPR signal.⁷⁹ The adsorption on O sites of the MgO surface is clearly proven by the superhyperfine interaction of the electron spin with the ¹⁷O nucleus.⁷⁹ In short, Au adsorbed on bulk MgO is atomic-like and its bonding does not imply a net charge transfer. Things are completely different when a Au atom is adsorbed on a MgO ultrathin film. DFT calculations indicated the formation of a negatively charged Au⁻ species, as shown by the double occupancy of the 6s level, by the value of the atomic charge close to -1, and by the occurrence of a strong polaronic distortion of the oxide substrate, typical of charge traps in insulators.^{158a,176} In the absence of defects or grain boundaries (the computed films were ideal and defect-free), it was suggested that charging occurs via electron tunneling.

The occurrence of the charge transfer has been demonstrated experimentally by depositing low amounts of Au atoms on 3 ML MgO/Ag(001) films at very low temperature (4 K). Low-temperature STM was used to analyze the resulting samples and showed the formation of a special ordering of the deposited Au atoms.¹⁷⁷ This ordering, which is absent when Pd atoms are deposited in the same conditions, can be explained with the repulsive interactions between charged Au adatoms. While this indicates the occurrence of a charge transfer, it does not provide any information on its direction as the ordering could be due to a positive as well as to a negative adsorbate. Again, STM provided convincing evidence for the negative charging (Figure 33). The STM image of the adsorbed Au adatoms on MgO/Ag(001) films has a particular shape very similar to that observed by Repp et al.¹⁷⁸ in an experiment where Au anions

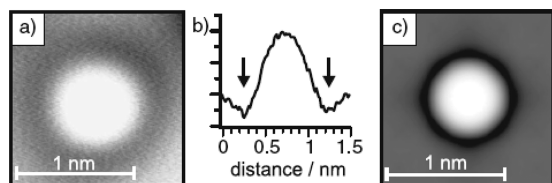


Figure 33. Experimental STM image (a) and height profiles (b) and corresponding simulated STM image (c) of a single Au atom on the surface of 3 ML thin MgO/Ag(001) films. The depression in the height profile results in a bright image surrounded by a dark ring typical of negatively charged Au. Reproduced with permission from ref 177. Copyright 2007 American Physical Society.

were prepared on NaCl/Cu(111) ultrathin films by injection of a single electron by the STM tip into the Au 6s level. The possibility to inject selectively the extra charge on some Au atoms and not on others lead to the presence on the same support of both Au⁰ and Au⁻ species, which appear very different in STM, allowing their distinction.¹⁷⁸ In particular, whereas neutral Au appears as a big bright spot, charged gold has a different profile with a bright central region surrounded by a dark ring (depression) (Figure 33). The profile of the image of Au atoms on MgO/Ag(001) exhibits a “sombbrero” effect typical of negatively charged atoms on conducting substrates, proving the fact that a charge transfer has occurred. Simulated STM images obtained from DFT calculations using the Tersoff–Hamann approach also show that the sombrero shape appears only for Au⁻ and not for Au⁰ (Figure 33).

Recently, another unambiguous proof of the occurrence of a charge transfer through the thin MgO films has been reported. This is closely related to the original Cabrera and Mott model of oxidation of metals.¹⁷² According to DFT calculations, not only Au atoms but also O₂ molecules adsorbed on the surface of MgO/Ag(001) films should induce an electron transfer from the substrate with formation of a superoxide radical anion, O₂⁻.¹⁷⁹ No such effect exists on bare MgO, where O₂ interacts weakly and forms O₂⁻ species only in the presence of strong electron donors (e.g., alkali adatoms or electrons trapped at the surface).¹⁸⁰ Low-temperature EPR experiments on O₂ molecules adsorbed on 4 ML MgO/Mo(001) films have shown the typical EPR signature of a superoxide anion (Figure 34).¹⁸¹ The

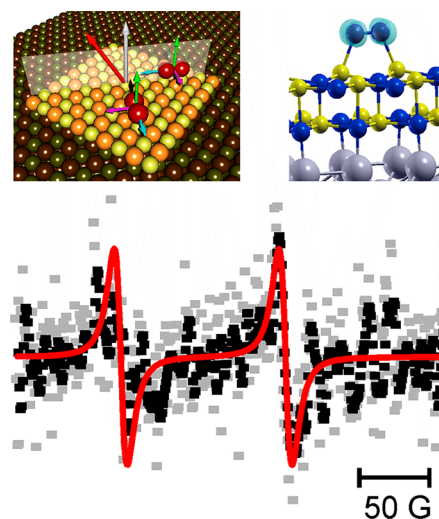


Figure 34. Top left shows a sketch of oxygen molecules adsorbed on 2 ML MgO/Mo(001) films as predicted by theory together with the orientation of the magnetic field as used in the experiment; (Top right) result of a DFT calculation of O₂⁻ on a 2 ML thin MgO(001) film on Mo(001) showing the polaronic distortion of the MgO lattice; (Bottom) EPR spectrum of 20 L O₂ adsorbed at 40 K on a 4 ML thick MgO(001) film on Mo(001) with the magnetic field oriented in the surface plane.¹⁸¹ Reproduced with permission from ref 181. Copyright 2011 Wiley-VCH.

intensity of the feature decreases with the number of layers and disappears for a 15 ML MgO film. Thus, the spontaneous charge transfer is possible only for films of 1–2 nm thickness and is not present for thicker films as expected for a model of electron tunneling. The analysis of the g-tensor has also shown in a quite convincing way that the MgO film undergoes a

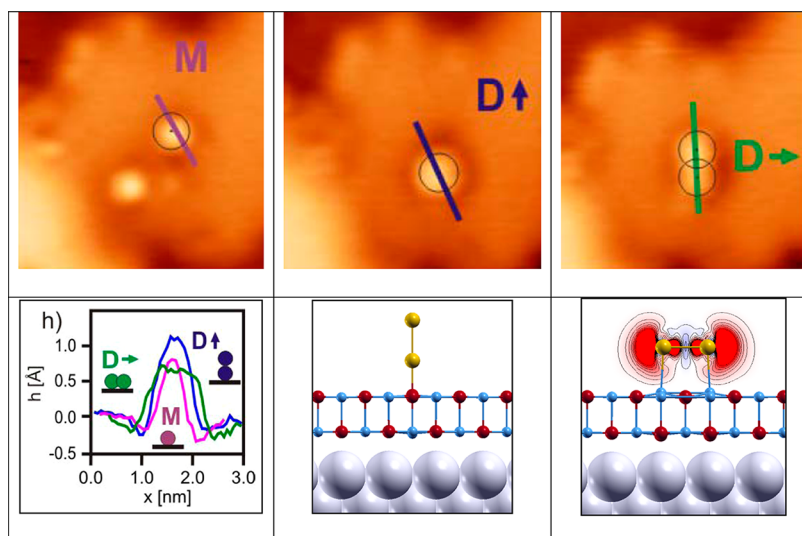


Figure 35. (Top) STM images of Au monomers (M), upright Au₂ dimers (D↑), and flat-lying Au₂ dimers (D→) on 3 ML MgO/Ag(001). (Bottom) Corresponding line profiles and structures of upright Au₂ of flat Au₂⁻ on 2 ML MgO/Ag(001). Notice the displacement of Mg (blue) and O (red) ions (polaronic distortion) and the spin density distribution of paramagnetic Au₂⁻.¹⁸⁴ Reproduced with permission from ref 184. Copyright 2008 American Chemical Society.

substantial polaronic distortion in correspondence of the formation of the O₂⁻ species, an effect that is absent on bare MgO (Figure 34).¹⁸¹ Notice that the role of the polaronic distortion is essential for the occurrence of the charge transfer, as will be discussed later. In fact, if in a computational experiment one freezes the coordinates of the MgO ultrathin films, thus avoiding the polaronic distortion, no charge transfer occurs and the adsorbate remains neutral.

Another example of an adsorbate that can induce electron transfer and formation of anionic species is that of a NO₂ molecule with strong electron-acceptor character that forms NO₂⁻ anions when adsorbed on MgO ultrathin films.¹⁸² The phenomenon is therefore quite general and represents an initial step toward activation and dissociation of admolecules. The reactivity of these species can be particularly high, and indeed it has been suggested theoretically that the coadsorption of CO and O₂ on the surface of MgO/Ag(001) films can result in the easy formation of CO₂, a reaction that does not occur on the regular MgO surface.^{179,183} This effect can be of tremendous importance for catalysis.

7.3. Conditions for the Occurrence of Direct Charge Transfer

The occurrence of a charge transfer through a thin dielectric film on a metal opens some interesting possibilities in terms of tuning the adsorbate properties. For instance, it has been shown that the occurrence of the charge transfer can depend on the orientation of the adsorbed molecule.¹⁸⁴ Au has been deposited at 4 K on MgO/Ag(001) thin films, and STM images show that the majority of the adsorbed species (90%) are indeed Au atoms with a small fraction of dimers formed upon deposition and diffusion on the oxide surface. The analysis of the STM images for the dimers shows that they can exist in two geometries, with the molecular axis normal or parallel to the surface. According to DFT calculations, upright dimers are neutral and sit preferentially on O sites whereas the flat-lying dimers populate a manifold of different azimuthal orientations and are negatively charged, which results in a longer Au–Au distance (Figure 35).

It is possible to prepare supported metal particles with different charge states and even different structures simply by changing the thickness of the oxide film. In fact, the extent of tunneling is related to the thickness of the insulating layer: beyond a given thickness the behavior of a bulk oxide surface is fully recovered. This aspect has been investigated in detail both theoretically and experimentally. Au clusters assume completely different structures when deposited on very thin (2–3 layers) or thick films.^{156e,160,185} Small clusters up to Au₇ form planar structures on the MgO(001) bare surface with the cluster plane perpendicular to the oxide surface¹⁸⁵ whereas on MgO ultrathin films the clusters adopt a linear structure (Figure 35).¹⁸⁵ The effect is even more dramatic for Au₂₀ and larger particles. From a thermodynamic point of view Au tends to form three-dimensional (3D) particles on oxide surfaces owing to the lower surface energies of oxides compared with metals. Indeed, on MgO(001) Au₂₀ keeps the tetrahedral 3D shape it has in the gas phase. However, on a 2 ML MgO/Mo(001) film Au₂₀ prefers to assume a flat, two-dimensional (2D) shape.^{160a} The effect has been proven experimentally by depositing Au atoms at low temperature on 2–3 ML or on 8 ML MgO films on Ag(001) and inducing aggregation and cluster growth by annealing the system up to room temperature. The STM images (Figure 36),^{160b} clearly show that on the 2–3 ML film for high Au coverage extended 2D gold islands are observed, whereas only 3D Au particles appear on the thicker 8 ML films.^{160b} Thus, by using MgO films of different thicknesses, completely different growth modes of gold clusters can be induced.

The origin of the change in shape of the Au clusters on thick and ultrathin MgO films is again the occurrence of a charge transfer from the metal substrate. The charge localizes at the Au–MgO interface and strongly reinforces the Au–MgO interaction, thus favoring the change in structure. Using a low-temperature STM and analyzing the images obtained on a Au₁₈ 2D cluster and in particular the nodal structure of the wave function, it has been possible to determine the exact number of electrons that are transferred to the supported particle.¹⁸⁶ In the case of Au₁₈, four extra electrons are accumulated at the

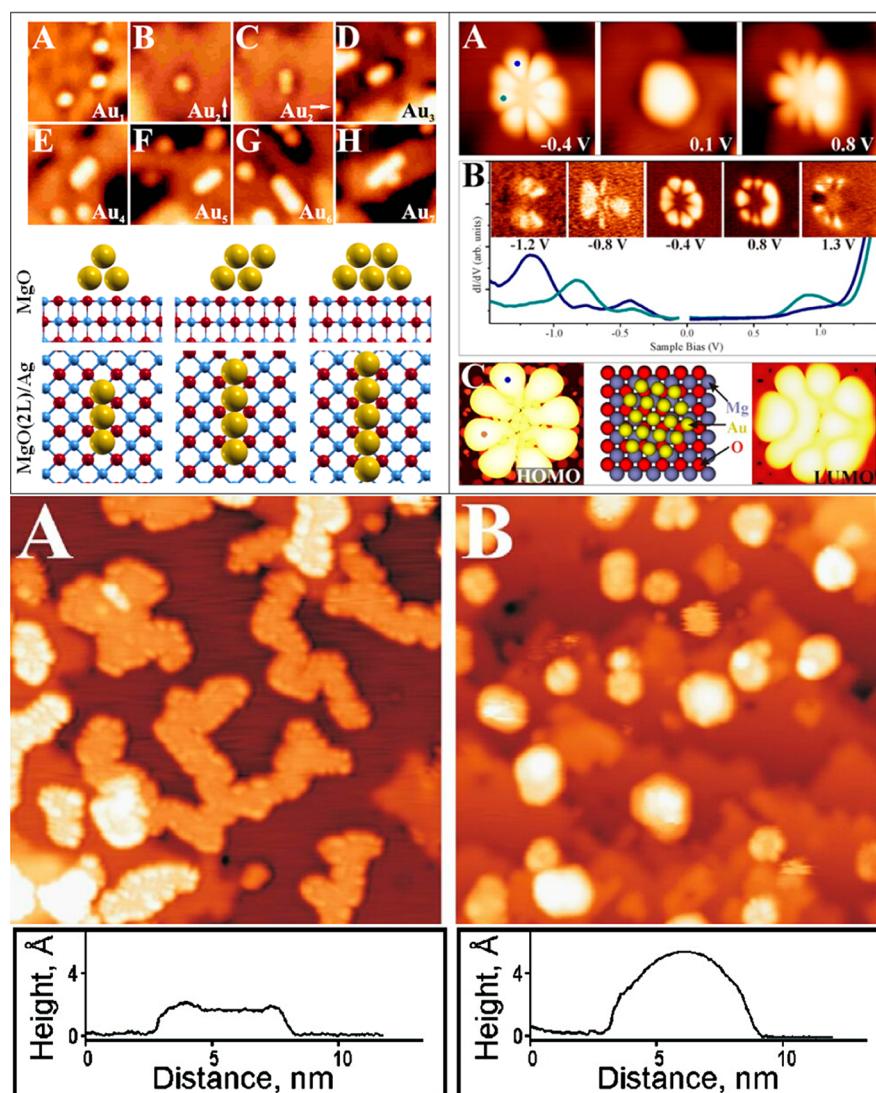


Figure 36. (Top left, upper panel) STM topographic images of (A) Au monomers, (B, C) upright and flat Au dimers, and (D–H) Au₃–Au₇ chains on MgO/Ag(001); (Top left, lower panel) DFT calculated Au clusters for bulk MgO(001) or MgO(2L)/Ag(001) films. Adapted with permission from ref 185. Copyright 2008 American Physical Society. (Top right) (A) Topographic and (B) dI/dV images of Au₁₈ on MgO/Ag(001). The corresponding dI/dV spectra are shown. (C) Calculated HOMO and LUMO shape. Reproduced with permission from ref 186. Copyright 2009 American Physical Society. (Bottom) STM images of Au deposits on (A) 3 ML and (B) 8 ML MgO/Ag(001) and corresponding height profiles. Reproduced with permission from ref 160b. Copyright 2007 American Physical Society.

interface between the flat gold cluster and the MgO film. This has direct consequences on the reactivity of the system. For instance, it has been suggested based on DFT calculations that several O₂ molecules can bind at the periphery of the gold nanoislands and capture negative charge with formation of superoxide O₂⁻ ions.¹⁸⁷ These gold islands are also expected to be highly reactive in low-temperature CO oxidation.^{183,188} The consequence of these results for catalysis and in general for cluster properties is apparent.

In principle, the charge transfer can be stimulated in cases where the oxide film is too thick by applying an external electric field. DFT calculations suggested that by applying an electric field of 1 V/nm it is possible to stabilize two-dimensional Au₂₀ even on a 8 ML MgO/Ag(001) film, whereas under field-free conditions the preferred structure of the adsorbed Au₂₀ is a 3D tetrahedron.¹⁸⁹

In the examples discussed so far, the electron transfer occurs from the oxide thin film to the adsorbate and refers specifically

to MgO. The question is if the effect is restricted to MgO or if it can occur also with other insulating oxides and if it can occur also in the opposite direction, from the adsorbate to the supporting film. The answer to the first question is that indeed electron transfer to adsorbed gold has been reported also on other thin oxide films like, for instance, alumina on NiAl.^{144,158b,190} On the other side, electron flow from an adsorbate to the metal has been demonstrated for a different oxide/metal interface, FeO/Pt(111). The FeO film consists of one atomic layer of Fe atoms at direct contact with the Pt(111) surface, as well as an external layer of O atoms. DFT calculations and scanning tunneling spectra (STS) show that Au atoms deposited at 5 K on the FeO/Pt(111) film adsorb on top of O and that the Au 6s level is empty, above the Fermi level (E_F).¹⁹¹ This means that Au⁺ has formed and a charge transfer from the adsorbate to the substrate has occurred, opposite to the Au/MgO/Ag(001) case.

So, the same atom, Au, can behave completely differently when deposited on MgO or FeO films. The reason is that the occurrence and direction of the charge transfer depend on the position of the highest occupied molecular orbital (HOMO) (or LUMO) levels of the adsorbed species with respect to the metal Fermi level, E_F . In particular, if the adsorbate HOMO is above E_F , the resulting potential difference drives a spontaneous electron tunneling through the thin dielectric barrier and electrons can be transferred to the metal/oxide interface. This is the case of K atoms on MgO/Ag(001).¹⁹² Alkali atoms have low ionization potentials (typically 4 eV), which are further reduced to 2–3 eV by the interaction with an oxide support.^{99a} Because E_F of most metals is between 4 and 5 eV below the vacuum level, alkali metals are easily ionized on ultrathin oxide films. This is also the case mentioned above of Au atoms deposited on FeO/Pt(111) films.¹⁹¹

On the contrary, if the LUMO of the adsorbate falls below E_F , a condition verified for species with high electron affinity like O₂, NO₂, or Au, electrons can flow from the metal support toward the adsorbate (Figure 37). Once the electron is

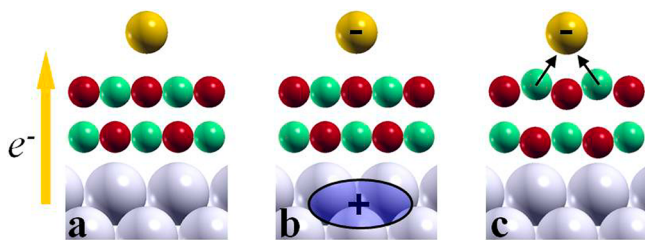


Figure 37. Electron transfer phenomena through an oxide thin film: (a) electron tunneling, (b) polarization of the metal substrate (image charge), and (c) polaronic-like distortion of the oxide. Electron tunneling in the opposite direction also can occur. Reproduced with permission from ref 174b. Copyright 2011 American Chemical Society.

transferred, there are two additional effects that contribute to stabilize the charge species: (i) an induced image charge forms in the metal substrate and provides an electrostatic attractive term and (ii) a polaronic-like distortion of the ionic lattice screens the charged species (Figure 37).

Of course, there is also the possibility that the HOMO or LUMO levels of the adsorbed species are near E_F so that the potential energy difference may be too small to induce a spontaneous tunneling. In this case no charge transfer occurs, and the adsorbate remains neutral, as for Pd atoms deposited on MgO 2–3 layer films.¹⁷⁷

Of course, point defects created at the surface or in the interior of an oxide film (in particular O vacancies) can act in the same way as adsorbed atoms, molecules, or clusters, as they also introduce filled and empty states in the band gap (Figure 21). Results of DFT calculations on F centers created on MgO thin films suggest that in some conditions the F⁰ center is metastable or unstable and may transform into the paramagnetic F⁺ center.¹²⁵ This may occur when the defect state induced by the F⁰ center in the band gap is very close to the metal Fermi level, a condition that is fulfilled for MgO films on Ag(100). The phenomenon is enhanced when the vacancy is closer to the interface. The effect may change with increasing film thickness and converge to the typical stability of F⁰ compared to F⁺ on the surface of MgO(100). The observed stability of F⁺ centers is enhanced by the strong lattice

distortion, which always accompanies the formation of charged vacancies. On MgO/Mo(100) films, where the Fermi level is at higher energies, F⁰ centers are stable and do not show a tendency to transform into F⁺. On the contrary, F⁺ centers can transform spontaneously into neutral F⁰ centers by capturing an electron from the Mo substrate. Of course, DFT calculations do not address the important question of a lifetime of some particular charge state of a defect. This lifetime would depend on the defect position with respect to metal, i.e., film thickness.

7.4. Work Function Changes Induced by Oxide Thin Films on Metals

Thus, charge transfer on ultrathin insulating films is governed on one side by the position of the frontier orbitals of the adsorbate (HOMO or LUMO) and on the other side by the metal Fermi level. This latter depends on the nature of the metal/oxide interface, and it provides an important conceptual way to tune and modify in a desired manner the properties of the support. The direct measure of E_F in a metal is the work function Φ_m , the energy needed to move one electron from E_F into the vacuum. Therefore, Φ_m becomes a central quantity as it determines the direction of the electron flow on oxide thin films.

The growth of an oxide layer on a metal or semiconductor surface may result in substantial changes of the metal work function.^{146b} In particular, this can lead to an increase of the work function, thus favoring charge transfer from the adsorbate to the support, or, less frequently, to a decrease of the work function, thus making possible a charge transfer in the opposite direction. This is the case of MgO films and, more in general, of films of ionic materials interacting mostly by electrostatic forces with the supporting metal. König et al.^{124b} measured the work-function shift of Ag(001) induced by the deposition of 1, 3, and 8 monolayers of MgO based on three independent scanning probe techniques using a dynamic force microscope and scanning tunneling microscope in ultrahigh vacuum at low temperature (5 K). The methods used are based on (i) Kelvin probe force microscopy measuring the contact potential difference, (ii) $I(z)$ curves, and (iii) field-emission resonances. It turns out that the three approaches give very similar values and in particular a $\Delta\Phi$ of 1.1–1.4 eV, which is in excellent agreement with the theoretical prediction of $\Delta\Phi = 1.3$ eV computed for ideal MgO/Ag(001) thin films.^{146b} Similar results have been obtained for MgO/Mo(001) films by Vaida et al. using femtosecond laser photoemission.¹⁹³

A reduction of the work function is not the usual result when an oxide is grown on a metal. In fact, the presence of O atoms at the interface generally causes a charge displacement from the metal to the oxide film with creation of an interface dipole, μ , which shifts the position of the metal Fermi energy. In particular, a dipole that corresponds to negative charge above the metal results in a work-function increase, $\Delta\Phi > 0$. This is the classical picture proposed by Kingdom and Langmuir (1923)¹⁹⁴ and by Gurney (1935),¹⁹⁵ for adsorbed species on metal surfaces: Φ increases (decreases) for negative (positive) adsorbates on a metal because an image charge forms into the metal, giving rise to a dipole layer that the emitted electron must pass through.

There are systems, however, where the work-function change is substantial despite the fact that the charge transfer at the interface is small or negligible. This is the case of films of ionic materials like MgO or NaCl, as discussed above, which induce a substantial reduction of the work function of 1 eV and

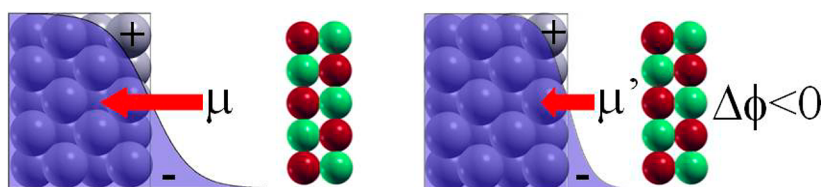


Figure 38. Schematic representation of the compressive electrostatic contribution to the reduction in work function Φ , induced by an ultrathin dielectric layer on a metal. Reproduced with permission from ref 174b. Copyright 2011 American Chemical Society.

more.^{124b,196} In highly ionic materials the anions are already fully reduced and cannot take extra charge, so that a charge flow can occur only in direction of the metal, but this is much too small to justify a work-function change of more than 1 eV. The change in work function is large because of a mechanism of electrostatic nature, also called “compression” effect (Figure 38).^{146,197} The effect has been attributed to the polarization of the metal electrons induced by the oxide film, a mechanism that has been proposed also for adsorbates on metal surfaces.¹⁹⁸ In particular, a recent work has emphasized the role of the exchange (or Pauli) repulsion in determining work-function changes induced by rare gases on metals.¹⁹⁹ The “rigid wall” represented by the dielectric layer pushes the electronic charge that spills over from the metal surface back into the metal, thus changing the surface dipole even in the absence of charge displacement between the metal and the insulating film (Figure 38). Although the charge transfer mechanism dominates the value of the work function for films with strong chemical interaction with the metal, the electrostatic or “compression” effect is important for films of highly ionic materials where the adhesion is more of electrostatic nature, like MgO.

7.5. Structural Flexibility of Oxide Ultrathin Films

The last point that we want to discuss is the role of surface relaxation and polaronic distortion in stabilizing charged species on ultrathin films. We already mentioned previously that EPR experiments on the formation of O_2^- on MgO/Mo(001) films prove the occurrence of a substantial surface relaxation (in particular the Mg^{2+} cations move outward to reduce their distance from the O_2^- molecule, resulting in modified g-tensor values).¹⁸¹ This geometrical flexibility is a specific property of ultrathin films that is not observed on a bulk surface: O_2^- adsorption on the terrace sites of MgO nanocrystals does not result in any appreciable surface relaxation.¹⁸⁰

Structural modifications of thin films may be due to charged adsorbed species or to charge transfers at the metal/oxide interface. Oxide monolayers, which are flat when unsupported, have a nonvanishing rumpling when supported on a metal surface. This relaxation can be seen as a response to the charge transfer at the interface: the dipole moment associated to the rumpling of the ionic crystal opposes that resulting from interface charge transfer, so that the two partially compensate each other.²⁰⁰ Theory shows that for MgO monolayers adsorbed on simple metals (Al and Mg) small amounts of charge are transferred from the metal to the oxide, inducing a negative rumpling (oxygen closer to the metal surface). On the contrary, for MgO on transition metals (Ag, Mo, and Pt) small amounts of electronic charge are transferred from the oxide to the substrate and the rumpling is positive (oxygen relaxes outward, Figure 39a and b). This effect is specific of oxide monolayers and does not depend on the crystallographic orientation, as it has been shown for MgO monolayers in the nonpolar (001) and polar (111) orientations.²⁰⁰

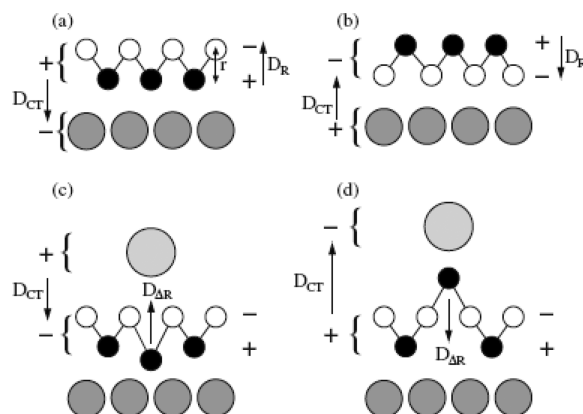


Figure 39. (a and b) Schematic representation of the coupling between dipole moments due to the interface charge transfer (D_{CT}) and oxide film rumpling (D_R) in bare oxide monolayer films (black circles = cations, white circles = anions) deposited on a metal substrate (large gray circles); (c and d) schematic representation of positive (c) and negative (d) adsorption modes of an adatom (large circle) on a supported oxide film. In positive adsorption, the polaronic-like distortion induced by the adatom locally increases the rumpling (distance between planes of anions and cations); in negative adsorption mode, the distortion locally reduces or inverts the rumpling. Dipole moments due to charging of the adatom (D_{CT}) and to the adsorption-induced structural distortion (D_R) are plotted schematically with arrows in the two cases. Reproduced with permission from ref 201. Copyright 2009 American Physical Society.

A similar electrostatic coupling also exists when atoms, molecules, or clusters are adsorbed on the oxide film (polaronic distortion). When a spontaneous charge transfer takes place, the local relaxation induces a dipole moment (due to the rumpling of the ionic layer), which partially counterbalances the dipole moment due to the charge transfer. On a very flexible oxide monolayer, the same adsorbate can be stabilized in two opposite charge states (Figure 39c and d).²⁰¹ For this reason, the adsorption on 2 ML MgO/Ag(001) of Au and K atoms (which become negatively and positively charged, respectively) induces structural relaxation in the opposite direction such as to create a dipole moment, which partially screens that due to the charged adspecies (Figure 39).

The structural flexibility is intimately connected to the phonon structure of materials. A way of investigating vibrational properties of solids is to look at the broadening in photoelectron spectra.²⁰² This broadening is natural and easy to observe in X-ray photoelectron spectra, which are routinely measured for oxide films on metal supports. By comparing experiments on MgO thin films with *ab initio* calculations, it has been shown that the changes in bond lengths between the initial ground state and the core-hole ionized states are directly related to the extent of the vibrational broadening. It is reasonable to expect that changes in the initial-state polaronic distortion will significantly affect the final-state changes in bond

length. Changes in the Franck–Condon broadenings in Mg 2p XPS spectra for a MgO monolayer on Ag(001) from their bulk values (Figure 40) arise because of several differences between

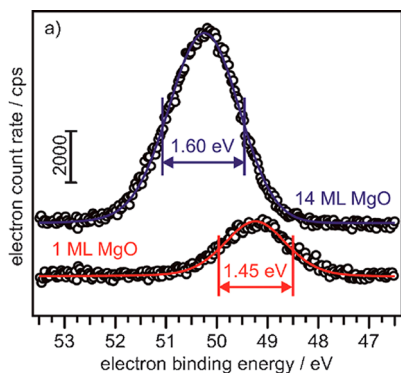


Figure 40. Mg 2p XPS spectra of 14 and 1 ML MgO/Ag(001).²⁰² Reproduced with permission from ref 202. Copyright 2011 Wiley-VCH.

the two systems: (1) The equilibrium Mg–O distance is different for bulk and monolayer MgO. (2) The curvature of these potential curves, as measured by ω_{e} , is different between bulk and monolayer. (3) The final-state relaxation, or screening, for the 2p hole state is larger for the monolayer because the polarizable metal responds to the Mg 2p hole. This analysis demonstrates the much larger structural flexibility of MgO ultrathin films compared to the bulk material, showing that the concept of flexibility influencing charge transfer and catalytic activity may be studied using photoelectron spectroscopy.

To summarize, in this section we have shown that oxide ultrathin films of few nm thickness and below may exhibit new phenomena that make these systems extremely appealing for novel and unprecedented applications. In particular, electron transport through the thin dielectric barrier is possible, which allows direct and spontaneous charging of adsorbed species or structures even in the absence of defects. This, together with other properties like the high structural flexibility or the possibility to tune the metal work function by appropriate choice of the deposited oxide layer, contributes to make these materials of potential interest in very diverse fields, from catalysis to fuel cells, from sensors to microelectronics, from storage devices to spintronics.²⁰³

8. SYNOPSIS

This review has covered the development of ideas concerning electronic properties of prototypical ionic oxide surfaces of MgO and defects associated with such surfaces, as well as the relation of those structural properties to chemical reactivity from their creation in the first part of the last century until today. The particular emphasis was placed on how electron transfer, which occurs when electrons are trapped at oxide surface defects, may be used to induce chemical reactions in species interacting with those surfaces. It is demonstrated how, in parallel to the development of more sophisticated experimental techniques and high-level first principles calculations, early ideas had to be refined to finally lead to a basic understanding of structure reactivity relations involving electron transfer. This is having considerable consequences on a variety of areas and, in particular, on the field of catalysis, where oxide surface properties determine to a large extent the stability and reactivity of the employed composite, i.e., mixed

metal–oxide systems. This is why, often in this review, reference is made to studies where nanoparticles are deposited onto oxide surfaces, as those nanoparticles may be used as information carriers to judge electron transfer on the basis of the observed nanoparticle morphology and chemical activity. In addition to the discussion of the electron transfer properties of the binary oxide, the influence of dopants within the binary oxide onto those properties is investigated, and, again, the consequences for oxide–metal nanoparticle interactions are discussed. The investigation of electron transfer properties at bulk MgO surfaces has led to the development of ideas, to use ultrathin MgO films supported on a metal substrate as model systems, where the oxide film presents a barrier to control electron transfer from the oxide metal interface to species interacting with the oxide film surface. Those ideas may be useful in the future to design materials properties in relation to the chemical activity.

The review is based almost exclusively on examples taken from MgO, probably with SiO₂ and TiO₂, one of the best characterized oxides, but the concepts and ideas illustrated are valid in general and apply to every oxide surface. In fact, every oxide surface exposes both anionic and cationic sites and can thus act as an electron donor (a base) or as an electron acceptor (an acid). On every oxide surface, low-coordinated sites exhibit an higher activity than the regular fully coordinated bulk sites due to the lower stability of undercoordinated cations and anions. Also the concept of electron trapping is very general, as electron-rich centers can be generated on virtually every oxide, although under different conditions. Finally, the unexpected and often unprecedented properties of oxide ultrathin films are not restricted to MgO but can be found in many other cases of two-dimensional dielectric materials. What is certainly different in MgO compared to other oxides, and in particular to transition metal and rare-earth oxides, is the possibility for the metal cation to change oxidation state. Although +2 is the only stable oxidation state of Mg cations, in reducible oxides like TiO₂ or CeO₂ the metal cation can easily change oxidation state and efficiently trap electrons from donor species adsorbed on the surface of the material. The main consequence is that ET from an adsorbate (e.g., hydrogen) can more easily occur on reducible transition metal oxides than on simple, nonreducible metal oxides like MgO or Al₂O₃.

The study of ET processes on MgO surfaces has involved the development of new tools, concepts, and ideas that have been useful not only to unravel a series of experimental evidence on this specific oxide but, more in general, to understand and interpret phenomena occurring on the surface of a wide class of oxide materials.

AUTHOR INFORMATION

Corresponding Author

*E-mail: gianfranco.pacchioni@unimib.it.

Notes

The authors declare no competing financial interest.

Biographies



Gianfranco Pacchioni (born 1954) received his Ph.D. at the Freie Universität Berlin in 1984. He worked at the IBM Almaden Research Center, at the Technical University of Munich, and at the University of Milano. Since 2000 he is Full Professor at the University of Milano Bicocca, where he has been Director of the Department of Materials Science (2003–2009). He is President of the Theoretical and Computational Chemistry Division of the Italian Chemical Society. He received various awards including the Humboldt Award in 2005 and is a member of several advisory boards of scientific journals. He has published about 400 papers (h-index 66). His main interest is the electronic structure of oxides surfaces, interfaces, and thin films, defects in oxides, and supported metal clusters.



Hans-Joachim Freund (born 1951) studied physics and chemistry at the University of Cologne, where he received his Ph.D. in 1978 and his habilitation in 1983. Between 1979 and 1981, he worked in the Physics Department at the University of Pennsylvania as a postdoctoral fellow. In 1983 he became Associate Professor at Erlangen University, and in 1987 he became Professor at Bochum University; in 1995 he accepted a position as scientific member and director of the Department of Chemical Physics at the Fritz-Haber-Institut der Max-Planck-Gesellschaft in Berlin. He serves as Honorary Professor of five universities. He received several national and international awards and he is a member of several academies, scientific societies, and advisory boards of scientific journals.

ACKNOWLEDGMENTS

G.P. thanks C. Di Valentin, L. Giordano, and E. Giamello for continuous valuable discussions and contributions to the topic of electron transfer at oxide surfaces. Financial support from the Italian MIUR through the FIRB Project RBAP115AYN “Oxides at the nanoscale: Multifunctionality and applications” and the PRIN Project “New generation photosensitive semiconducting

oxides modified with non metals to enhance solar light harvesting. Design, synthesis, characterisation and testing” is gratefully acknowledged. H.F. thanks M. Heyde, N. Nilius, M. Sterrer, and T. Risse for invaluable contributions and M. Misch for her help with the manuscript. Also, he thanks the Deutsche Forschungsgemeinschaft for funding through SFB 546 (Transition metal oxide aggregates) and the Cluster of Excellence UNICAT. The Fonds der Chemischen Industrie is gratefully acknowledged for financial support. Finally, G.P. and H.F. thank the support of the COST Action D41 “Inorganic oxide surfaces and interfaces” and of the COST Action CM1104 “Reducible oxide chemistry, structure and functions”.

REFERENCES

- (1) (a) Imahori, H.; Sakata, Y. *Adv. Mater.* **1997**, *9*, 537. (b) Cukier, R. L.; Nocera, D. G. *Annu. Rev. Phys. Chem.* **1998**, *49*, 337. (c) Ward, M. D. *Chem. Soc. Rev.* **1997**, *26*, 365. (d) Raymo, F. M.; Tomasulo, M. *Chem. Soc. Rev.* **2005**, *34*, 327.
- (2) Miller, R. J. D.; McLendon, G. L.; Nozik, A. J.; Schmikler, W.; Willig, F. *Surface Electron Transfer Processes*; VCH: Weinheim, Germany, 1995.
- (3) (a) Newton, M. D.; Sutin, N. *Annu. Rev. Phys. Chem.* **1984**, *35*, 437. (b) Mikkelsen, K. V.; Ratner, M. A. *Chem. Rev.* **1987**, *87*, 113. (c) Zhang, J.; Kuznetsov, A. M.; Medvedev, I. G.; Chi, Q.; Albrecht, T.; Jensen, P. S.; Ulstrup, J. *Chem. Rev.* **2008**, *108*, 2737. (d) Adams, D. M.; Brus, L.; Chidsey, C. E. D.; Creager, S.; Creutz, C.; Kagan, C. R.; Kamat, P. V.; Lieberman, M.; Lindsay, S.; Marcus, R. A.; Metzger, R. M.; Michel-Beyerle, M. E.; Miller, J. R.; Newton, M. D.; Rolison, D. R.; Sankey, O.; Schanze, K. S.; Yardley, J.; Zhu, X. *J. Phys. Chem. B* **2003**, *107*, 6668.
- (4) Chiesa, M.; Giamello, E.; Che, M. *Chem. Rev.* **2010**, *110*, 1320.
- (5) Bagus, P. S.; Illas, F.; Pacchioni, G.; Parmigiani, F. *J. Electron Spectrosc. Relat. Phenom.* **1999**, *100*, 215.
- (6) (a) Ha, S. D.; Ramanathan, S. *J. Appl. Phys.* **2011**, *110*, 071101. (b) Guillén, C.; Herrero, J. *Thin Solid Films* **2011**, *520*, 1. (c) Ohtaki, M. *J. Ceram. Soc. Jpn.* **2011**, *119*, 770. (d) Chandra, S.; Barick, K. C.; Bahadur, D. *Adv. Drug Delivery Rev.* **2011**, *63*, 1267. (e) Fergus, J. W. *J. Eur. Ceram. Soc.* **2012**, *32*, 525.
- (7) (a) Marcus, R. A.; Sutin, N. *Biochim. Biophys. Acta: Bioenerg.* **1985**, *811*, 265. (b) Marcus, R. A. *Annu. Rev. Phys. Chem.* **1964**, *15*, 155.
- (8) (a) Sauer, J. *Chem. Rev.* **1989**, *89*, 199. (b) Diebold, U. *Surf. Sci. Rep.* **2003**, *48*, 53. (c) Osgood, R. *Chem. Rev.* **2006**, *106*, 4379. (d) Zhao, J.; Li, B.; Onda, K.; Feng, M.; Petek, H. *Chem. Rev.* **2006**, *106*, 4402. (e) Brown, G. E., Jr.; Henrich, V. E.; Casey, W. H.; Clark, D. L.; Eggleston, C.; Felmy, A.; Goodman, D. W.; Grätzel, M.; Maciel, G.; McCarthy, M. I.; Nealon, K. H.; Sverjensky, D. A.; Toney, M. F.; Zachara, J. M. *Chem. Rev.* **1999**, *99*, 77. (f) Spoto, G.; Bordiga, S.; Zecchina, A.; Cocina, D.; Gribov, E. N.; Regli, L.; Groppo, E.; Lamberti, C. *Catal. Today* **2006**, *113*, 65. (g) Spoto, G.; Gribov, E. N.; Ricchiardi, G.; Damin, A.; Scarano, D.; Bordiga, S.; Lamberti, C.; Zecchina, A. *Prog. Surf. Sci.* **2004**, *76*, 71.
- (9) Kohn, H. W. *J. Chem. Phys.* **1960**, *33*, 1588.
- (10) Nelson, R. L.; Tench, A. J. *J. Chem. Phys.* **1964**, *40*, 2736.
- (11) (a) Lunsford, J. H.; Jayne, J. P. *J. Chem. Phys.* **1966**, *44*, 1487. (b) Lunsford, J. H.; Jayne, J. P. *J. Chem. Phys.* **1966**, *44*, 1492. (c) Lunsford, J. H.; Jayne, J. P. *NASA Technical Note D-3355*; 1966.
- (12) Zecchina, A.; Stone, F. S. *J. Chem. Soc., Faraday Trans. 1* **1978**, *74*, 2278.
- (13) Di Valentin, C.; Finazzi, E.; Pacchioni, G. *Surf. Sci.* **2005**, *591*, 70.
- (14) Aristov, Y. I.; Volkov, A. I.; Parmon, V. N.; Zamaraev, K. I. *React. Kinet. Catal. Lett.* **1984**, *25*, 329.
- (15) Whited, R. C.; Flaten, C. J.; Walker, W. C. *Solid State Commun.* **1973**, *13*, 1903.
- (16) Schönberger, U.; Aryasetiawan, F. *Phys. Rev. B* **1995**, *52*, 8788.
- (17) Pacchioni, G.; Sousa, C.; Illas, F.; Parmigiani, F.; Bagus, P. S. *Phys. Rev. B* **1993**, *48*, 11573.

- (18) Pandey, R.; Jaffe, J. E.; Kunz, A. B. *Phys. Rev. B* **1991**, *43*, 9228.
- (19) Tjeng, L. H.; Vos, A. R.; Sawatzky, G. A. *Surf. Sci.* **1990**, *235*, 269.
- (20) Giamello, E.; Ugliengo, P.; Garrone, E. *J. Chem. Soc., Faraday Trans. 1* **1989**, *85*, 1373.
- (21) Kantorovich, L. N.; Shluger, A. L.; Sushko, P. V.; Gunster, J.; Stracke, P.; Goodman, D. W.; Kempter, V. *Faraday Discuss.* **1999**, *114*, 173.
- (22) Wichtendahl, R.; Rodriguez-Rodrigo, M.; Härtel, U.; Kühlenbeck, H.; Freund, H.-J. *Surf. Sci.* **1999**, *423*, 90.
- (23) Spoto, G.; Gribov, E. N.; Damin, A.; Ricchiardi, G.; Zecchina, A. *Surf. Sci.* **2003**, *540*, L605.
- (24) Civalieri, B.; Maschio, L.; Ugliengo, P.; Zicovich-Wilson, C. M. *Phys. Chem. Chem. Phys.* **2010**, *12*, 6382.
- (25) Pacchioni, G. *Surf. Rev. Lett.* **2000**, *7*, 277.
- (26) Pacchioni, G.; Ricart, J. M.; Illas, F. *J. Am. Chem. Soc.* **1994**, *116*, 10152.
- (27) Lu, X.; Xu, X.; Wang, N.; Zhang, Q. *J. Phys. Chem. B* **2000**, *104*, 10024.
- (28) Ochs, D.; Brause, M.; Braun, B.; Maus-Friedrichs, W.; Kempter, V. *Surf. Sci.* **1998**, *397*, 101.
- (29) Ochs, D.; Braun, B.; Maus-Friedrichs, W.; Kempter, V. *Surf. Sci.* **1998**, *417*, 406.
- (30) (a) Carrier, X.; Doyle, C. S.; Kendelewicz, T.; Brown, G. E., Jr. *Surf. Rev. Lett.* **1999**, *6*, 1237. (b) Doyle, C. S.; Kendelewicz, T.; Carrier, X.; Brown, G. E., Jr. *Surf. Rev. Lett.* **1999**, *6*, 1247.
- (31) (a) Giamello, E.; Murphy, D.; Marchese, L.; Martra, G.; Zecchina, A. *J. Chem. Soc., Faraday Trans.* **1993**, *89*, 3715. (b) Marchese, L.; Coluccia, S.; Martra, G.; Giamello, E.; Zecchina, A. *Mater. Chem. Phys.* **1991**, *29*, 437.
- (32) (a) Zecchina, A.; Scarano, D.; Bordiga, S.; Ricchiardi, G.; Spoto, G.; Geobaldo, F. *Catal. Today* **1996**, *27*, 403. (b) Sterrer, M.; Risse, T.; Freund, H.-J. *Appl. Catal., A* **2006**, *307*, 58.
- (33) (a) Pacchioni, G.; Minerva, T.; Bagus, P. S. *Surf. Sci.* **1992**, *275*, 450. (b) Coluccia, S.; Baricco, M.; Marchese, L.; Martra, G.; Zecchina, A. *Spectrochim. Acta, Part A* **1993**, *49*, 1289. (c) Nygren, M. A.; Pettersson, L. G. M. *J. Chem. Phys.* **1996**, *105*, 9339.
- (34) Dohnálek, Z.; Kimmel, G. A.; Joyce, S. A.; Ayotte, P.; Smith, R. S.; Kay, B. D. *J. Phys. Chem. B* **2001**, *105*, 3747.
- (35) Scarano, D.; Spoto, G.; Bordiga, S.; Coluccia, S.; Zecchina, A. *J. Chem. Soc., Faraday Trans.* **1992**, *88*, 291.
- (36) Heidberg, J.; Kandel, M.; Meine, D.; Wildt, U. *Surf. Sci.* **1995**, *331–333* (Part B), 1467.
- (37) Pacchioni, G.; Cogliandro, G.; Bagus, P. S. *Int. J. Quantum Chem.* **1992**, *42*, 1115.
- (38) Garrone, E.; Zecchina, A.; Stone, F. S. *Philos. Mag. B* **1980**, *42*, 683.
- (39) (a) Stankic, S.; Müller, M.; Diwald, O.; Sterrer, M.; Knözinger, E.; Bernardi, J. *Angew. Chem., Int. Ed.* **2005**, *44*, 4917. (b) Müller, M.; Stankic, S.; Diwald, O.; Knözinger, E.; Sushko, P. V.; Trevisanutto, P. E.; Shluger, A. L. *J. Am. Chem. Soc.* **2007**, *129*, 12491. (c) Sterrer, M.; Berger, T.; Diwald, O.; Knözinger, E. *J. Am. Chem. Soc.* **2003**, *125*, 195.
- (40) Benedetti, S.; Benia, H. M.; Nilius, N.; Valeri, S.; Freund, H. J. *J. Chem. Phys. Lett.* **2006**, *430*, 330.
- (41) Sushko, P. V.; Gavartin, J. L.; Shluger, A. L. *J. Phys. Chem. B* **2002**, *106*, 2269.
- (42) Hacquart, R.; Krafft, J.-M.; Costentin, G.; Jupille, J. *Surf. Sci.* **2005**, *595*, 172.
- (43) Coluccia, S.; Deane, A. M.; Tench, A. J. *J. Chem. Soc., Faraday Trans.* **1978**, *74*, 2913.
- (44) (a) Sushko, P. V.; Shluger, A. L.; Catlow, C. R. A. *Surf. Sci.* **2000**, *450*, 153. (b) Shluger, A. L.; Sushko, P. V.; Kantorovich, L. N. *Phys. Rev. B* **1999**, *59*, 2417.
- (45) Anpo, M.; Yamada, Y.; Kubokawa, Y.; Coluccia, S.; Zecchina, A.; Che, M. *J. Chem. Soc., Faraday Trans. 1* **1988**, *84*, 751.
- (46) Rosenblatt, G. H.; Rowe, M. W.; Williams, G. P., Jr.; Williams, R. T.; Chen, Y. *Phys. Rev. B* **1989**, *39*, 10309.
- (47) Kramer, J.; Ernst, W.; Tegenkamp, C.; Pfnür, H. *Surf. Sci.* **2002**, *517*, 87.
- (48) de Boer, J. H. *Rec. Trav. Chim.* **1937**, *56*, 301.
- (49) Wertz, J. E.; Auzins, P.; Weeks, R. A.; Silsbee, R. H. *Phys. Rev.* **1957**, *107*, 1535.
- (50) Henderson, B.; Wertz, J. E. *Adv. Phys.* **1968**, *17*, 749.
- (51) Scorza, E.; Birkenheuer, U.; Pisani, C. *J. Chem. Phys.* **1997**, *107*, 9645.
- (52) Tench, A. J. *Surf. Sci.* **1971**, *25*, 625.
- (53) Sharma, R. R.; Stoneham, A. M. *J. Chem. Soc., Faraday Trans. 2* **1976**, *72*, 913.
- (54) (a) Molnar, J. P.; Hartman, C. D. *Phys. Rev.* **1950**, *79*, 1015. (b) Sibley, W. A.; Chen, Y. *Phys. Rev.* **1967**, *160*, 712. (c) Chen, Y.; Kolopus, J. L.; Sibley, W. A. *Phys. Rev.* **1969**, *186*, 865.
- (55) Kappers, L. A.; Kroes, R. L.; Hensley, E. B. *Phys. Rev. B* **1970**, *1*, 4151.
- (56) Nelson, R. L.; Hale, J. W. *Discuss. Faraday Soc.* **1971**, *52*, 77.
- (57) Henrich, V. E.; Dresselhaus, G.; Zeiger, H. J. *Phys. Rev. B* **1980**, *22*, 4764.
- (58) Underhill, P. R.; Gallon, T. E. *Solid State Commun.* **1982**, *43*, 9.
- (59) (a) Peterka, D.; Tegenkamp, C.; Schröder, K. M.; Ernst, W.; Pfnür, H. *Surf. Sci.* **1999**, *431*, 146. (b) Kramer, J.; Tegenkamp, C.; Pfnür, H. *Phys. Rev. B* **2003**, *67*, 235401.
- (60) (a) Paganini, M. C.; Chiesa, M.; Giamello, E.; Coluccia, S.; Martra, G.; Murphy, D. M.; Pacchioni, G. *Surf. Sci.* **1999**, *421*, 246. (b) Berger, T.; Sterrer, M.; Diwald, O.; Knözinger, E. *J. Phys. Chem. B* **2004**, *108*, 7280.
- (61) (a) Sousa, C.; Pacchioni, G.; Illas, F. *Surf. Sci.* **1999**, *429*, 217. (b) Illas, F.; Pacchioni, G. *J. Chem. Phys.* **1998**, *108*, 7835. (c) Markovits, A.; Minot, C.; Ménétrey, M.; Sousa, C.; Illas, F. *Solid State Ionics* **2007**, *178*, 173.
- (62) (a) Wu, M. C.; Truong, C. M.; Coulter, K.; Goodman, D. W. *J. Am. Chem. Soc.* **1992**, *114*, 7565. (b) Gibson, A.; Haydock, R.; LaFemina, J. P. *Appl. Surf. Sci.* **1993**, *72*, 285. (c) Gibson, A.; Haydock, R.; LaFemina, J. P. *Phys. Rev. B* **1994**, *50*, 2582. (d) Giamello, E.; Murphy, D.; Ravera, L.; Coluccia, S.; Zecchina, A. *J. Chem. Soc., Faraday Trans.* **1994**, *90*, 3167. (e) Murphy, D.; Giamello, E. *J. Phys. Chem.* **1995**, *99*, 15172. (f) Orlando, R.; Millini, R.; Perego, G.; Dovesi, R. *J. Mol. Catal. A: Chem.* **1997**, *119*, 253. (g) Murphy, D. M.; Farley, R. D.; Purnell, I. J.; Rowlands, C. C.; Jacob, A. R.; Paganini, M. C.; Giamello, E. *J. Phys. Chem. B* **1999**, *103*, 1944. (h) Sterrer, M.; Diwald, O.; Knözinger, E. *J. Phys. Chem. B* **2000**, *104*, 3601. (i) Kuzovkov, V. N.; Popov, A. I.; Kotomin, E. A.; Monge, M. A.; González, R.; Chen, Y. *Phys. Rev. B* **2001**, *64*, 064102. (j) Xu, Y.; Li, J.; Zhang, Y.; Chen, W. *Surf. Sci.* **2003**, *525*, 13.
- (63) (a) Wu, M. C.; Truong, C. M.; Coulter, K.; Goodman, D. W. *J. Vac. Sci. Technol. A* **1993**, *11*, 2174. (b) Coulter, K.; Szanyi, J.; Goodman, D. W. *Catal. Lett.* **1995**, *35*, 23.
- (64) (a) Kolmakov, A.; Stultz, J.; Goodman, D. W. *J. Chem. Phys.* **2000**, *113*, 7564. (b) Kim, Y. D.; Stultz, J.; Goodman, D. W. *Langmuir* **2002**, *18*, 3999. (c) Wendt, S.; Kim, Y. D.; Goodman, D. W. *Prog. Surf. Sci.* **2003**, *74*, 141.
- (65) Ferrari, A. M.; Pacchioni, G. *J. Phys. Chem.* **1995**, *99*, 17010.
- (66) Pacchioni, G.; Pescarmona, P. *Surf. Sci.* **1998**, *412–413*, 657.
- (67) Carrasco, J.; Lopez, N.; Illas, F.; Freund, H.-J. *J. Chem. Phys.* **2006**, *125*, 074711.
- (68) Mori-Sánchez, P.; Recio, J. M.; Silvi, B.; Sousa, C.; Pendás, M. A.; Luaña, V.; Illas, F. *Phys. Rev. B* **2002**, *66*, 075103.
- (69) (a) Pacchioni, G.; Ferrari, A. M.; Giamello, E. *Chem. Phys. Lett.* **1996**, *255*, 58. (b) Ferrari, A. M.; Pacchioni, G. *J. Chem. Phys.* **1997**, *107*, 2066.
- (70) (a) Ferrari, A. M.; Pacchioni, G. *J. Phys. Chem.* **1996**, *100*, 9032. (b) Giordano, L.; Di Valentin, C.; Goniakowski, J.; Pacchioni, G. *Phys. Rev. Lett.* **2004**, *92*, 096105. (c) Neyman, K. M.; Inntam, C.; Matveev, A. V.; Nasluzov, V. A.; Röscher, N. *J. Am. Chem. Soc.* **2005**, *127*, 11652. (d) Xu, L.; Campbell, C. T.; Jónsson, H.; Henkelman, G. *Surf. Sci.* **2007**, *601*, 3133. (e) Del Vitto, A.; Pacchioni, G.; Delbecq, F.; Sautet, P. *J. Phys. Chem. B* **2005**, *109*, 8040. (f) Zhukovskii, Y. F.; Kotomin, E. A.; Jacobs, P. W. M.; Stoneham, A. M.; Harding, J. H. *J. Phys.: Condens. Matter* **2000**, *12*, 55.

- (71) (a) Sanchez, A.; Abbet, S.; Heiz, U.; Schneider, W. D.; Häkkinen, H.; Barnett, R. N.; Landman, U. *J. Phys. Chem. A* **1999**, *103*, 9573. (b) Abbet, S.; Sanchez, A.; Heiz, U.; Schneider, W. D.; Ferrari, A. M.; Pacchioni, G.; Rosch, N. *J. Am. Chem. Soc.* **2000**, *122*, 3453. (c) Yoon, B.; Häkkinen, H.; Landman, U.; Wörz, A.; Antonietti, J.-M.; Abbet, S.; Judai, K.; Heiz, U. *Science* **2005**, *307*, 403. (d) Heiz, U.; Bullock, E. L. *J. Mater. Chem.* **2004**, *14*, 564.
- (72) Yan, Z.; Chinta, S.; Mohamed, A. A.; Fackler, J. P.; Goodman, D. W. *J. Am. Chem. Soc.* **2005**, *127*, 1604.
- (73) (a) Molina, L. M.; Hammer, B. *J. Catal.* **2005**, *233*, 399. (b) Barcaro, G.; Fortunelli, A. *J. Chem. Theory Comput.* **2005**, *1*, 972. (c) Barcaro, G.; Aprà, E.; Fortunelli, A. *Chem.—Eur. J.* **2007**, *13*, 6408. (d) Caballero, R.; Quintanar, C.; Köster, A. M.; Khanna, S. N.; Reveles, J. U. *J. Phys. Chem. C* **2008**, *112*, 14919. (e) Yang, Z.; Wu, R.; Zhang, Q.; Goodman, D. W. *Phys. Rev. B* **2002**, *65*, 155407.
- (74) Sterrer, M.; Yulikov, M.; Fischbach, E.; Heyde, M.; Rust, H.-P.; Pacchioni, G.; Risse, T.; Freund, H.-J. *Angew. Chem., Int. Ed.* **2006**, *45*, 2630.
- (75) Meyer, R.; Lemire, C.; Shaikhutdinov, S. K.; Freund, H. *Gold Bull.* **2004**, *37*, 72.
- (76) Benia, H. M.; Lin, X.; Gao, H. J.; Nilus, N.; Freund, H.-J. *J. Phys. Chem. C* **2007**, *111*, 10528.
- (77) Sterrer, M.; Fischbach, E.; Risse, T.; Freund, H.-J. *Phys. Rev. Lett.* **2005**, *94*, 186101.
- (78) Di Valentin, C.; Neyman, K. M.; Risse, T.; Sterrer, M.; Fischbach, E.; Freund, H.-J.; Nasluzov, V. A.; Pacchioni, G.; Rösch, N. *J. Chem. Phys.* **2006**, *124*, 044708.
- (79) Yulikov, M.; Sterrer, M.; Heyde, M.; Rust, H. P.; Risse, T.; Freund, H.-J.; Pacchioni, G.; Scagnelli, A. *Phys. Rev. Lett.* **2006**, *96*, 146804.
- (80) Giamello, E.; Garrone, E.; Ugliengo, P.; Che, M.; Tench, A. J. *J. Chem. Soc., Faraday Trans. 1* **1989**, *85*, 3987.
- (81) Giamello, E.; Paganini, M. C.; Murphy, D. M.; Ferrari, A. M.; Pacchioni, G. *J. Phys. Chem. B* **1997**, *101*, 971.
- (82) Giamello, E.; Paganini, M. C.; Chiesa, M.; Murphy, D. M.; Pacchioni, G.; Soave, R.; Rockenbauer, A. *J. Phys. Chem. B* **2000**, *104*, 1887.
- (83) Diwald, O.; Knözinger, E.; Martra, G. *J. Chem. Phys.* **1999**, *111*, 6668.
- (84) (a) Kantorovich, L. N.; Holender, J. M.; Gillan, M. J. *Surf. Sci.* **1995**, *343*, 221. (b) Ménétrey, M.; Markovits, A.; Minot, C.; Del Vitto, A.; Pacchioni, G. *Surf. Sci.* **2004**, *549*, 294. (c) Pacchioni, G. *J. Chem. Phys.* **2008**, *128*, 182505.
- (85) (a) Ojamäe, L.; Pisani, C. *J. Chem. Phys.* **1998**, *109*, 10984. (b) Bogicevic, A.; Jennison, D. R. *Surf. Sci.* **1999**, *437*, L741. (c) D'Ercole, A.; Pisani, C. *J. Chem. Phys.* **1999**, *111*, 9743. (d) Ealet, B.; Goniakowski, J.; Finocchi, F. *Phys. Rev. B* **2004**, *69*, 195413. (e) Carrasco, J.; Lopez, N.; Illas, F. *J. Chem. Phys.* **2005**, *122*, 224705. (f) Venables, J. A.; Giordano, L.; Harding, J. H. *J. Phys.: Condens. Matter* **2006**, *18*, S411. (g) Costa, D.; Chizallet, C.; Ealet, B.; Goniakowski, J.; Finocchi, F. *J. Chem. Phys.* **2006**, *125*, 054702. (h) Shalabi, A. S.; Abdel Halim, W. S.; Ghonaim, M. S. *Physica B* **2011**, *406*, 397.
- (86) Ricci, D.; Pacchioni, G.; Sushko, P. V.; Shluger, A. L. *J. Chem. Phys.* **2002**, *117*, 2844.
- (87) (a) Ricci, D.; Di Valentin, C.; Pacchioni, G.; Sushko, P. V.; Shluger, A. L.; Giamello, E. *J. Am. Chem. Soc.* **2003**, *125*, 738. (b) Chiesa, M.; Paganini, M. C.; Giamello, E.; Murphy, D. M.; Di Valentin, C.; Pacchioni, G. *Acc. Chem. Res.* **2006**, *39*, 861.
- (88) Sterrer, M.; Berger, T.; Diwald, O.; Knözinger, E.; Sushko, P. V.; Shluger, A. L. *J. Chem. Phys.* **2005**, *123*, 064714.
- (89) (a) Gribov, E. N.; Bertarione, S.; Scarano, D.; Lamberti, C.; Spoto, G.; Zecchina, A. *J. Phys. Chem. B* **2004**, *108*, 16174. (b) Diwald, O.; Knözinger, E. *J. Phys. Chem. B* **2002**, *106*, 3495.
- (90) (a) Chiesa, M.; Paganini, M. C.; Spoto, G.; Del Vitto, A.; Di Valentin, C.; Pacchioni, G.; Giamello, E. *J. Phys. Chem. B* **2005**, *109*, 7314. (b) Sterrer, M.; Berger, T.; Stankic, S.; Diwald, O.; Knözinger, E. *ChemPhysChem* **2004**, *5*, 1695.
- (91) (a) Coluccia, S.; Boccuzzi, F.; Ghiotti, G.; Morterra, C. *J. Chem. Soc., Faraday Trans. 1* **1982**, *78*, 2111. (b) Diwald, O.; Hofmann, P.; Knözinger, E. *Phys. Chem. Chem. Phys.* **1999**, *1*, 713.
- (92) Chiesa, M.; Paganini, M. C.; Giamello, E.; Di Valentin, C.; Pacchioni, G. *Angew. Chem., Int. Ed.* **2003**, *42*, 1759.
- (93) Chiesa, M.; Martino, P.; Giamello, E.; Di Valentin, C.; Del Vitto, A.; Pacchioni, G. *J. Phys. Chem. B* **2004**, *108*, 11529.
- (94) (a) Zhang, Z.; Du, Y.; Petrik, N. G.; Kimmel, G. A.; Lyubinetsky, I.; Dohnálek, Z. *J. Phys. Chem. C* **2009**, *113*, 1908. (b) Wöll, C. *Prog. Surf. Sci.* **2007**, *82*, 55.
- (95) (a) Jensen, M. C. R.; Venkataramani, K.; Helveg, S.; Clausen, B. S.; Reichling, M.; Besenbacher, F.; Lauritsen, J. V. *J. Phys. Chem. C* **2008**, *112*, 16953. (b) Brown, M. A.; Carrasco, E.; Sterrer, M.; Freund, H.-J. *J. Am. Chem. Soc.* **2010**, *132*, 4064.
- (96) (a) Brown, M. A.; Fujimori, Y.; Ringleb, F.; Shao, X.; Stavale, F.; Nilus, N.; Sterrer, M.; Freund, H.-J. *J. Am. Chem. Soc.* **2011**, *133*, 10668. (b) Brown, M. A.; Ringleb, F.; Fujimori, Y.; Sterrer, M.; Freund, H.-J.; Preda, G.; Pacchioni, G. *J. Phys. Chem. C* **2011**, *115*, 10114.
- (97) Vayssilov, G. N.; Gates, B. C.; Rösch, N. *Angew. Chem., Int. Ed.* **2003**, *42*, 1391.
- (98) Napoli, F.; Chiesa, M.; Giamello, E.; Finazzi, E.; Di Valentin, C.; Pacchioni, G. *J. Am. Chem. Soc.* **2007**, *129*, 10575.
- (99) (a) Chiesa, M.; Giamello, E.; Di Valentin, C.; Pacchioni, G.; Sojka, Z.; Van Doorslaer, S. *J. Am. Chem. Soc.* **2005**, *127*, 16935. (b) Lian, J. C.; Finazzi, E.; Di Valentin, C.; Risse, T.; Gao, H. J.; Pacchioni, G.; Freund, H. J. *J. Chem. Phys. Lett.* **2008**, *450*, 308.
- (100) (a) Edwards, P. P. *Adv. Inorg. Chem. Radiochem.* **1982**, *25*, 135. (b) Chiesa, M.; Giamello, E.; Van Doorslaer, S. *J. Am. Chem. Soc.* **2009**, *131*, 12664.
- (101) Preda, G.; Pacchioni, G.; Chiesa, M.; Giamello, E. *J. Phys. Chem. C* **2008**, *112*, 19568.
- (102) Livraghi, S.; Paganini, M. C.; Giamello, E. *J. Mol. Catal. A: Chem.* **2010**, *322*, 39.
- (103) (a) Ricci, D.; Pacchioni, G.; Sushko, P. V.; Shluger, A. L. *Surf. Sci.* **2003**, *542*, 293. (b) Chiesa, M.; Giamello, E.; Paganini, M. C.; Sojka, Z.; Murphy, D. M. *J. Chem. Phys.* **2002**, *116*, 4266.
- (104) Chiesa, M.; Giamello, E.; Murphy, D. M.; Pacchioni, G.; Paganini, M. C.; Soave, R.; Sojka, Z. *J. Phys. Chem. B* **2001**, *105*, 497.
- (105) Socaciu, L. D.; Hagen, J.; Bernhardt, T. M.; Wöste, L.; Heiz, U.; Häkkinen, H.; Landman, U. *J. Am. Chem. Soc.* **2003**, *125*, 10437.
- (106) Pacchioni, G.; Siculo, S.; Valentin, C. D.; Chiesa, M.; Giamello, E. *J. Am. Chem. Soc.* **2008**, *130*, 8690.
- (107) Molina, L. M.; Alonso, J. A. *J. Phys. Chem. C* **2007**, *111*, 6668.
- (108) (a) Hagen, J.; Socaciu, L. D.; Eljazyfer, M.; Heiz, U.; Bernhardt, T. M.; Wöste, L. *Phys. Chem. Chem. Phys.* **2002**, *4*, 1707. (b) Wallace, W. T.; Whetten, R. L. *J. Am. Chem. Soc.* **2002**, *124*, 7499.
- (109) Wang, F.; Zhang, D.; Sun, H.; Ding, Y. *J. Phys. Chem. C* **2007**, *111*, 11590.
- (110) (a) Yoon, B.; Häkkinen, H.; Landman, U. *J. Phys. Chem. A* **2003**, *107*, 4066. (b) Salisbury, B. E.; Wallace, W. T.; Whetten, R. L. *J. Chem. Phys.* **2000**, *262*, 131. (c) Stolcic, D.; Fischer, M.; Ganteför, G.; Kim, Y. D.; Sun, Q.; Jena, P. *J. Am. Chem. Soc.* **2003**, *125*, 2848. (d) Mills, G.; Gordon, M. S.; Metiu, H. *Chem. Phys. Lett.* **2002**, *359*, 493.
- (111) (a) Meerson, O.; Sitja, G.; Henry, C. R. *Eur. Phys. J. D* **2005**, *34*, 119. (b) Arenz, M.; Landman, U.; Heiz, U. *ChemPhysChem* **2006**, *7*, 1871.
- (112) Wang, J.; Hammer, B. *Top. Catal.* **2007**, *44*, 49.
- (113) In *Nanoscience and Technology*; Morita, S., Giessibl, F. J., Wiesendanger, R., Eds.; Springer: Berlin, Heidelberg, 2009; Vol. 2.
- (114) Erni, R. *Aberration-Corrected Imaging in Transmission Electron Microscopy: An Introduction*; Imperial College Press: London, 2010.
- (115) Barth, C.; Henry, C. R. *Phys. Rev. Lett.* **2003**, *91*, 196102.
- (116) Livshits, A. L.; Shluger, A. L.; Rohl, A. L.; Foster, A. S. *Phys. Rev. B: Condens. Matter Mater. Phys.* **1999**, *59*, 2436.
- (117) (a) Barth, C.; Foster, A. S.; Henry, C. R.; Shluger, A. L. *Adv. Mater.* **2011**, *23*, 477. (b) Sushko, M. L.; Gal, A. Y.; Watkins, M.; Shluger, A. L. *Nanotechnology* **2006**, *17*, 2062.

- (118) Schintke, S.; Messerli, S.; Pivetta, M.; Patthey, F.; Libiouille, L.; Stengel, M.; De Vita, A.; Schneider, W.-D. *Phys. Rev. Lett.* **2001**, *87*, 2768011.
- (119) (a) König, T.; Simon, G. H.; Heinke, L.; Lichtenstein, L.; Heyde, M. *Beilstein J. Nanotechnol.* **2011**, *2*, 1. (b) König, T.; Simon, G. H.; Martinez, U.; Giordano, L.; Pacchioni, G.; Heyde, M.; Freund, H.-J. *ACS Nano* **2010**, *4*, 2510. (c) Heyde, M.; Simon, G. H.; Rust, H. P.; Freund, H. J. *Appl. Phys. Lett.* **2006**, *89*, 263107.
- (120) Sterrer, M.; Heyde, M.; Novicki, M.; Nilius, N.; Risse, T.; Rust, H. P.; Pacchioni, G.; Freund, H.-J. *J. Phys. Chem. B* **2006**, *110*, 46.
- (121) König, T.; Simon, G. H.; Rust, H. P.; Pacchioni, G.; Heyde, M.; Freund, H. J. *J. Am. Chem. Soc.* **2009**, *131*, 17544.
- (122) Sader, J. E.; Jarvis, S. P. *Appl. Phys. Lett.* **2004**, *84*, 1801.
- (123) Treveltham, T.; Shluger, A. *Nanotechnology* **2009**, *20*, 264019.
- (124) (a) Pacchioni, G. In *The Chemical Physics of Solid Surfaces—Oxide Surfaces*; Woodruff, D. P., Ed.; Elsevier: Amsterdam, 2001; Vol. 9, p 94. (b) König, T.; Simon, G. H.; Rust, H. P.; Heyde, M. *J. Phys. Chem. C* **2009**, *113*, 11301. (c) Siculo, S.; Giordano, L.; Pacchioni, G. *J. Phys. Chem. C* **2009**, *113*, 10256.
- (125) Giordano, L.; Martinez, U.; Pacchioni, G.; Watkins, M.; Shluger, A. L. *J. Phys. Chem. C* **2008**, *112*, 3857.
- (126) Giordano, L.; Goniakowski, J.; Pacchioni, G. *Phys. Rev. B* **2001**, *64*, 075417.
- (127) Somorjai, G. A. *Introduction to Surface Chemistry and Catalysis*; John Wiley & Sons, Inc.: New York, 1994.
- (128) Gonchar, A. Ph.D. Thesis, Freie Universität Berlin, Berlin, Germany, 2011.
- (129) Finocchi, F.; Goniakowski, J.; Noguera, C. *Phys. Rev. B: Condens. Matter Mater. Phys.* **1999**, *59*, 5178.
- (130) (a) Popov, A. I.; Monge, M. A.; González, R.; Chen, Y.; Kotomin, E. *Solid State Commun.* **2001**, *118*, 163. (b) De Vita, A.; Gillan, M. J.; Lin, J. S.; Payne, M. C.; Stich, L.; Clarke, L. *J. Phys. Rev. B* **1992**, *46*, 12964.
- (131) (a) Freund, H.-J. *Faraday Disc.* **1999**, *114*, 1. (b) Pacchioni, G. *Solid State Sci.* **2000**, *2*, 161.
- (132) McKenna, K. P.; Shluger, A. *Nat. Mater.* **2008**, *7*, 859.
- (133) Wang, Z.; Saito, M.; McKenna, K. P.; Gu, L.; Tsukimoto, S.; Shluger, A. L.; Ikuhara, Y. *Nature* **2011**, *479*, 380.
- (134) (a) Klaua, M.; Ullmann, D.; Barthel, J.; Wulfhekel, W.; Kirschner, J.; Urban, R.; Monchesky, T. L.; Enders, A.; Cochran, J. F.; Heinrich, B. *Phys. Rev. B* **2001**, *64*, 134411. (b) Vassent, L.; Dynna, M.; Marty, A.; Gilles, B.; Patrat, G. *J. Appl. Phys.* **1996**, *80*, 5727. (c) Schoiswohl, J.; Zheng, W.; Surnev, S.; Ramsey, M. G.; Granozzi, G.; Agnoli, S.; Netzer, F. P. *Surf. Sci.* **2006**, *600*, 1099. (d) Benedetti, S.; Torelli, P.; Valeri, S.; Benia, H. M.; Nilius, N.; Renaud, G. *Phys. Rev. B* **2008**, *78*, 195411.
- (135) Lin, X.; Yang, B.; Benia, H. M.; Myrach, P.; Yulikov, M.; Aumer, A.; Brown, M.; Sterrer, M.; Bondarchuk, O.; Kieseritzky, E.; Rocker, J.; Risse, T.; Gao, H.; Nilius, N.; Freund, H. J. *J. Am. Chem. Soc.* **2010**, *132*, 7745.
- (136) Wollschläger, J.; Erdős, D.; Goldbach, H.; Höpken, R.; Schröder, K. M. *Thin Solid Films* **2001**, *400*, 1.
- (137) Dynna, M.; Vassent, J. L.; Marty, A. *J. Appl. Phys.* **1996**, *80*, 2650.
- (138) Ferrari, A. M.; Casassa, S.; Pisani, C.; Altieri, S.; Rota, A.; Valeri, S. *Surf. Sci.* **2005**, *588*, 160.
- (139) Rienks, E. D. L.; Nilius, N.; Rust, H. P.; Freund, H. J. *Phys. Rev. B* **2005**, *71*, 2414041.
- (140) Brune, H.; Giovannini, M.; Bromann, K.; Kern, K. *Nature* **1998**, *394*, 451.
- (141) Benia, H. M.; Myrach, P.; Gonchar, A.; Risse, T.; Nilius, M.; Freund, H. J. *Phys. Rev. B* **2010**, *81*, 241415.
- (142) Binnig, G.; Frank, K. H.; Fuchs, H.; Garcia, N.; Reihl, B.; Rohrer, H.; Salvan, F.; Williams, A. R. *Phys. Rev. Lett.* **1985**, *55*, 991.
- (143) Kolesnychenko, O. Y.; Kolesnichenko, Y. A.; Shklyarevskii, O.; van Kempen, H. *Physica B* **2000**, *291*, 246.
- (144) Nilius, N. *Surf. Sci. Rep.* **2009**, *64*, 595.
- (145) (a) Benia, H. M.; Myrach, P.; Nilius, M. *New J. Phys.* **2008**, *10*, 013010. (b) Benia, H. M.; Nilius, N.; Freund, H. J. *Surf. Sci.* **2007**, *601*, L55.
- (146) (a) Goniakowski, J.; Noguera, C. *Interface Sci.* **2004**, *12*, 93. (b) Giordano, L.; Cinquini, F.; Pacchioni, G. *Phys. Rev. B* **2006**, *73*, 045414.
- (147) McKenna, K. P.; Shluger, A. L. *Phys. Rev. B* **2009**, *79*, 224116.
- (148) Benia, H. M.; Myrach, P.; Nilius, N.; Freund, H. J. *Surf. Sci.* **2010**, *604*, 435.
- (149) Sterrer, M.; Fischbach, E.; Heyde, M.; Nilius, N.; Rust, H. P.; Risse, T.; Freund, H. J. *J. Phys. Chem. B* **2006**, *110*, 8665.
- (150) Ertl, G. *Angew. Chem.* **2008**, *120*, 3578. *Angew. Chem., Int. Ed.* **2008**, *47*, 3524.
- (151) (a) Morales, E.; Lundsford, J. H. *J. Catal.* **1989**, *118*, 255. (b) Ito, T.; Lundsford, J. H. *Nature* **1985**, *314*, 721.
- (152) Lundsford, J. H. *Angew. Chem., Int. Ed.* **1995**, *34*, 970.
- (153) (a) Driscoll, D. J.; Martir, W.; Wang, J. X.; Lundsford, J. H. *J. Am. Chem. Soc.* **1985**, *107*, 58. (b) Xiao, W.; Guo, Q.; Wang, E. G. *Chem. Phys. Lett.* **2003**, *368*, 527. (c) Ito, T.; Wang, J.; Lin, C. H.; Lundsford, J. H. *J. Am. Chem. Soc.* **1985**, *107*, 5062.
- (154) Cluster of Excellence “Unifying Concepts in Catalysis”; <http://www.unicat.tu-berlin.de/>, 2007.
- (155) Myrach, P.; Nilius, N.; Levchenko, S. V.; Gonchar, A.; Risse, T.; Dinse, K.-P.; Boatner, L. A.; Frandsen, W.; Horn, R.; Freund, H.-J.; Schlögl, R.; Scheffler, M. *ChemCatChem* **2010**, *2*, 854.
- (156) (a) Haruta, M.; Kobayashi, T.; Sano, H.; Yamada, N. *Chem. Lett.* **1987**, *16*, 405. (b) Valden, M.; Lai, X.; Goodman, D. W. *Science* **1998**, *281*, 1647. (c) Hashmi, A. S. K.; Hutchings, G. J. *Angew. Chem., Int. Ed.* **2006**, *45*, 7896. (d) Herzing, A. A.; Kiely, C. J.; Carley, A. F.; Landon, P.; Hutchings, G. J. *Science* **2008**, *321*, 1331. (e) Risse, T.; Shaikhutdinov, S.; Nilius, N.; Sterrer, M.; Freund, H.-J. *Acc. Chem. Res.* **2008**, *41*, 949.
- (157) Landman, U.; Yoon, B.; Zhang, C.; Heiz, U.; Arenz, M. *Top. Catal.* **2007**, *44*, 145.
- (158) (a) Pacchioni, G.; Giordano, L.; Baistrocchi, M. *Phys. Rev. Lett.* **2005**, *94*, 226104. (b) Nilius, N.; Ganduglia-Pirovano, M. V.; Brázdová, V.; Kulawik, M.; Sauer, J.; Freund, H. J. *Phys. Rev. Lett.* **2008**, *100*, 096802.
- (159) (a) Shapovalov, V.; Metiu, H. *J. Catal.* **2007**, *245*, 205. (b) Mammen, N.; Narasimhan, S.; de Gironcoli, S. *J. Am. Chem. Soc.* **2011**, *133*, 2801.
- (160) (a) Ricci, D.; Bongiorno, A.; Pacchioni, G.; Landman, U. *Phys. Rev. Lett.* **2006**, *97*, 036106. (b) Sterrer, M.; Risse, T.; Heyde, M.; Rust, H.-P.; Freund, H.-J. *Phys. Rev. Lett.* **2007**, *98*, 206103.
- (161) (a) Kim, H. Y.; Lee, H. M.; Pala, R. G. S.; Shapovalov, V.; Metiu, H. *J. Phys. Chem. C* **2008**, *112*, 12398. (b) Ganesh, R.; Pala, S.; Metiu, H. *J. Phys. Chem. C* **2007**, *111*, 12715.
- (162) (a) Bolorizadeh, M. A.; Sashin, V. A.; Kheifets, A. S.; Ford, M. *J. J. Electron Spectrosc. Relat. Phenom.* **2004**, *141*, 27. (b) Albuquerque, E. L.; Vasconcelos, M. S. *J. Phys.: Conf. Ser.* **2008**, *100*, 042006. (c) Stankic, S.; Bernadi, J.; Diwald, O.; Knözinger, E. *J. Phys. Chem. B* **2006**, *110*, 13866. (d) Trevisanutto, P. E.; Sushko, P. V.; Beck, K. M.; Joly, A. G.; Hess, W. P.; Shluger, A. L. *J. Phys. Chem. C* **2009**, *113*, 1274.
- (163) Paganini, M. C.; Chiesa, M.; Dolci, F.; Martino, P.; Giamello, E. *J. Phys. Chem. B* **2006**, *110*, 11918.
- (164) (a) Shao, X.; Myrach, P.; Nilius, N.; Freund, H.-J. *J. Phys. Chem. C* **2011**, *115*, 8784. (b) Shao, X.; Nilius, N.; Myrach, P.; Freund, H.-J.; Martinez, U.; Prada, S.; Giordano, L.; Pacchioni, G. *Phys. Rev. B* **2011**, *83*, 245407.
- (165) Henderson, B.; Imbusch, G. F. In *Optical Spectroscopy of Inorganic Solids*; Clarendon Press: Oxford, U.K., 1989.
- (166) Stavale, F.; Nilius, N.; Freund, H.-J. *New J. Phys.* **2012**, *14*, 033006.
- (167) Shao, X.; Prada, S.; Giordano, L.; Pacchioni, G.; Nilius, N.; Freund, H.-J. *Angew. Chem., Int. Ed.* **2011**, *50*, 11525.
- (168) (a) Bäumer, M.; Freund, H.-J. *Prog. Surf. Sci.* **1999**, *61*, 127. (b) Lai, X.; Clair, T. P. S.; Valden, M.; Goodman, D. W. *Prog. Surf. Sci.* **1998**, *59*, 25.

- (169) Martinez, U.; Giordano, L.; Pacchioni, G. *ChemPhysChem* **2010**, *11*, 412.
- (170) Stavale, F.; Shao, X.; Nilius, N.; Freund, H.-J.; Prada, S.; Giordano, L.; Pacchioni, G. *J. Am. Chem. Soc.* **2012**, *134*, 11380.
- (171) Shao, X.; Nilius, N.; Freund, H.-J. *J. Am. Chem. Soc.* **2012**, *134*, 2532.
- (172) Cabrera, N.; Mott, N. F. *Rep. Prog. Phys.* **1948**, *12*, 163.
- (173) (a) Olsson, C. O. A.; Landolt, D. *Electrochim. Acta* **2003**, *48*, 1093. (b) Kunze, J.; Maurice, V.; Klein, L. H.; Strehblow, H.-H.; Marcus, P. *J. Phys. Chem. B* **2001**, *105*, 4263.
- (174) (a) Freund, H.-J.; Pacchioni, G. *Chem. Soc. Rev.* **2008**, *37*, 2224. (b) Giordano, L.; Pacchioni, G. *Acc. Chem. Res.* **2011**, *44*, 1244.
- (175) Frondelius, P.; Hellman, A.; Honkala, K.; Hakkinen, H.; Gronbeck, H. *Phys. Rev. B* **2008**, *78*, 085426.
- (176) Giordano, L.; Martinez, U.; Siculo, S.; Pacchioni, G. *J. Chem. Phys.* **2007**, *127*, 144713.
- (177) Sterrer, M.; Risse, T.; Martinez Pozzoni, U.; Giordano, L.; Heyde, M.; Rust, H.-P.; Pacchioni, G.; Freund, H.-J. *Phys. Rev. Lett.* **2007**, *98*, 096107.
- (178) Repp, J.; Meyer, G.; Olsson, F. E.; Persson, M. *Science* **2004**, *305*, 493.
- (179) Hellman, A.; Klacar, S.; Grönbeck, H. *J. Am. Chem. Soc.* **2009**, *131*, 16636.
- (180) Napoli, F.; Chiesa, M.; Giamello, E.; Preda, G.; Di Valentin, C.; Pacchioni, G. *Chem.—Eur. J.* **2010**, *16*, 6776.
- (181) Gonchar, A.; Risse, T.; Freund, H.-J.; Giordano, L.; Di Valentin, C.; Pacchioni, G. *Angew. Chem., Int. Ed.* **2011**, *50*, 2635.
- (182) Grönbeck, H. *J. Phys. Chem. B* **2006**, *110*, 11977.
- (183) Harding, C.; Habibpour, V.; Kunz, S.; Farnbacher, A. N.-S.; Heiz, U.; Yoon, B.; Landman, U. *J. Am. Chem. Soc.* **2008**, *131*, 538.
- (184) Simic-Milosevic, V.; Heyde, M.; Nilius, N.; Koenig, T.; Rust, H. P.; Sterrer, M.; Risse, T.; Freund, H. J.; Giordano, L.; Pacchioni, G. *J. Am. Chem. Soc.* **2008**, *130*, 7814.
- (185) Simic-Milosevic, V.; Heyde, M.; Lin, X.; König, T.; Rust, H.-P.; Sterrer, M.; Risse, T.; Nilius, N.; Freund, H.-J.; Giordano, L.; Pacchioni, G. *Phys. Rev. B* **2008**, *78*, 235429.
- (186) Lin, X.; Nilius, N.; Freund, H. J.; Walter, M.; Frondelius, P.; Honkala, K.; Häkkinen, H. *Phys. Rev. Lett.* **2009**, *102*, 206801.
- (187) Frondelius, P.; Häkkinen, H.; Honkala, K. *Phys. Chem. Chem. Phys.* **2010**, *12*, 1483.
- (188) Zhang, C.; Yoon, B.; Landman, U. *J. Am. Chem. Soc.* **2007**, *129*, 2228.
- (189) Yoon, B.; Landman, U. *Phys. Rev. Lett.* **2008**, *100*, 056102.
- (190) Kulawik, M.; Nilius, N.; Freund, H. J. *Phys. Rev. Lett.* **2006**, *96*, 036103.
- (191) Giordano, L.; Pacchioni, G.; Goniakowski, J.; Nilius, N.; Rienks, E. D. L.; Freund, H.-J. *Phys. Rev. Lett.* **2008**, *101*, 026102.
- (192) Giordano, L.; Pacchioni, G. *Phys. Chem. Chem. Phys.* **2006**, *8*, 3335.
- (193) Vaida, M. E.; Gleitsmann, T.; Tchitnga, R.; Bernhardt, T. M. *J. Phys. Chem. C* **2009**, *113*, 10264.
- (194) Kingdom, K. H.; Langmuir, I. *Phys. Rev.* **1923**, *21*, 380.
- (195) Gurney, R. W. *Phys. Rev.* **1935**, *47*, 479.
- (196) Ploigt, H.-C.; Brun, C.; Pivetta, M.; Patthey, F.; Schneider, W. *D. Phys. Rev. B* **2007**, *76*, 195404.
- (197) Prada, S.; Martinez, U.; Pacchioni, G. *Phys. Rev. B* **2008**, *78*, 235423.
- (198) (a) Pettersson, L. G. M.; Bagus, P. S. *Phys. Rev. Lett.* **1986**, *56*, 500. (b) Michaelides, A.; Hu, P.; Lee, M. H.; Alavi, A.; King, D. A. *Phys. Rev. Lett.* **2003**, *90*, 246103. (c) De Renzi, V.; Rousseau, R.; Marchetto, D.; Biagi, R.; Scandolo, S.; del Pennino, U. *Phys. Rev. Lett.* **2005**, *95*, 046804.
- (199) Bagus, P. S.; Staemmler, V.; Wöll, C. *Phys. Rev. Lett.* **2002**, *89*, 096104.
- (200) Goniakowski, J.; Noguera, C. *Phys. Rev. B* **2009**, *79*, 155433.
- (201) Goniakowski, J.; Noguera, C.; Giordano, L.; Pacchioni, G. *Phys. Rev. B* **2009**, *80*, 125403.
- (202) Nelin, C. J.; Bagus, P. S.; Brown, M. A.; Sterrer, M.; Freund, H.-J. *Angew. Chem., Int. Ed.* **2011**, *50*, 10174.
- (203) *Oxide Ultrathin Films: Science and Technology*; Pacchioni, G., Valeri, S., Eds.; Wiley-VCH: Weinheim, Germany, 2012.